Coordination Chemistry Reviews 526 (2025) 216355

Contents lists available at ScienceDirect

Coordination Chemistry Reviews

journal homepage: www.elsevier.com/locate/ccr

Zirconium–based MXenes: Synthesis, properties, applications, and prospects

George Elsa [a,1], Abdul Hanan [a,1], Rashmi Walvekar [b,c], Arshid Numan [a,d], Mohammad Khalid [e,f,g,*]

[a] *Sunway Centre for Electrochemical Energy and Sustainable Technology (SCEEST), School of Engineering and Technology, Sunway University, No. 5 Jalan Universiti, Bandar Sunway 47500, Selangor Darul Ehsan, Malaysia*
[b] *Faculty of Innovation and Technology, School of Engineering, Chemical Engineering Programme, No.1 Jalan Taylor's, Taylor's University Malaysia, 47500 Subang Jaya, Selangor, Malaysia*
[c] *Chitkara Centre for Research and Development, Chitkara University, Himachal Pradesh 174103, India*
[d] *Department of Applied Physics, Saveetha School of Engineering, Saveetha University (SIMATS), Chennai, India*
[e] *Materials and Manufacturing Research Group, James Watt School of Engineering, University of Glasgow, Glasgow G12 8QQ, UK*
[f] *Faculty of Engineering, Manipal University Jaipur, Rajasthan 303007, India*
[g] *Centre for Research Impact & Outcome, Chitkara University Institute of Engineering and Technology, Chitkara University, Rajpura 140401, Punjab, India*

ARTICLE INFO

Keywords
2D materials
Zirconium
MXenes
Synthesis
Properties
Applications

ABSTRACT

Zirconium (Zr) based MXenes are a new type of two–dimensional (2D) transition metal carbides and carbonitrides that have attracted significant research interest in recent years. These materials exhibit a unique combination of physicochemical properties, making them attractive for a wide range of applications. Despite this growing attention, a systematic review of their synthesis methods, material properties, and applications is still lacking. This review provides a comprehensive overview of the state of research on Zr–MXenes, covering various aspects from synthesis to applications. The discussion includes an in–depth analysis of the different wet–chemical etching protocols used to obtain Zr–MXenes from Zr–containing MAX phases and the impact of these methods on the morphology of materials. Detailed characterization techniques have revealed important properties of Zr–MXenes, such as hydrophilicity, electrical conductivity, and ion storage capability. Further, this review examines the potential applications of Zr–MXenes in various fields, including energy storage, electromagnetic interference shielding, corrosion prevention, and biomedical applications. While, Zr–MXenes offer promising prospects, challenges related to large–scale production and property optimization must be addressed to facilitate their widespread adoption. By providing a comprehensive overview of Zr–MXene synthesis, properties, and applications, this review aims to inspire and guide future research and development efforts toward the rational design and utilization of these promising 2D nanomaterials.

1. Introduction

In recent years, there has been a considerable increase in research attention on two–dimensional (2D) materials, which are widely regarded as fundamental components in contemporary materials science [1,2]. Advanced 2D materials and nanomaterials have shown significant promise across various applications, including energy and environmental sectors [3,4]. This is attributed to their intriguing properties, such as elevated surface area, expanded porosity, better mechanical strength, and enhanced chemical stability. Such materials possessing layered architectures and exhibiting significant anisotropic bonding have been identified as viable candidates for electrochemical applications due to their capacity to perform diverse intercalation processes [5,6]. Extensive research has been conducted on graphene, members of the dichalcogenides family, and other related 2D materials, exploring their vast array of potential applications [7,8].

MXenes, the latest addition to the 2D materials family, have made a significant impact on materials science [4,9]. These materials are synthesized by selectively etching out the A layer from ternary carbides, nitrides, or carbonitrides, known as MAX phases, and follow the general formula $M_{n+1}AX_n$. In this formula, M represents an early transition

---

[*] Corresponding author at: Materials and Manufacturing Research Group, James Watt School of Engineering, University of Glasgow, Glasgow G12 8QQ, UK.
E-mail address: mohammad.khalid@glasgow.ac.uk (M. Khalid).

[1] Equal contributing authors.

https://doi.org/10.1016/j.ccr.2024.216355
Received 6 September 2024; Received in revised form 15 November 2024; Accepted 18 November 2024

Nomenclature

V	Vanadium
Ti	Titanium
Mo	Molybdenum
Nb	Niobium
Ta	Tantalum
Zr	Zirconium
C	Carbon
N	Nitrogen
B	Bulk modulus
G	Shear modulus
PU	Positive and unlabeled machine learning
PCA	Principal component analysis
TPR	True positive rates
PECS	Pulsed electric current sintering
TEM	Transmission electron microscopy
HRTEM	High–resolution transmission electron microscopy
SAED	Selected area electron diffraction
PVP	Polyvinyl pyrrolidone
TG–DSC	Thermogravimetry–Differential Scanning Calorimetry
TGA	Thermal gravimetry analysis
ELF	Electron localization functions
E_{ad}	Adsorption energy
ω_p	Plasma frequency
FWHM	Full width at half maximum
TBP	Temporal bandwidth product
SA	Saturable absorber
E	Deformation resistance
DOS	Density of states
CTE	Thermal expansion coefficient
Tc	Critical temperature
FM	Ferromagnetic
MAE	Magnetic anisotropy energy
AFM	Antiferromagnetic
SAOM	Saturable absorber optical modulators
Rq	Root mean square roughness
XPS	X–ray photoelectron spectroscopy
DES	Digital Emission Scanning
CTS	Compressive tensile strain
MSD	Magnetron sputtering deposition
LD	Diode laser
DFT	Density functional theory
F	Fluorine
O	Oxygen
S	Sulfur
Se	Selenium
Te	Tellurium
Na	Sodium
NVPF	Sodium vanadium fluorophosphate ($Na_3V_2(PO_4)_2F_3$)
GCD	Galvanostatic charge-discharge
CV	Cyclic voltammetry
EIS	Electrochemical impedance spectroscopy
K	Potassium
KIB	Potassium ion battery
GGA	Generalized gradient approximation
TPU	Thermoplastic polyurethane
Zr AMP	Zirconium amino tris (methylenephosphonate)
TENGs	Triboelectric nanogenerators
MOF	Metal–organic framework
M–TENG	Multilayered triboelectric nanogenerator
Co–NPC	Cobalt–nano porous carbon
VR	Virtual reality
MCU	Microcontroller unit
SPU	Signal processing unit
α–ZrP	α–Zr phosphate
MZP	MXene–ZrP@PDA
WEP	Waterborne epoxy
COF	Coefficient of friction
GO–ZrO_2	Graphene oxide–zirconia dioxide
NSs	Nanosheets
NIR–II	Near–infrared II
PDT	Photodynamic therapy
EPR	Enhanced permeability and retention
TME	Tumour microenvironment
FFT	Fast Fourier transform
Fcc	Face–centered cubic
P	Phosphorus
USEPA	United States Environmental Protection Agency
ppb	Parts per billion
SA	Sodium alginate
MX–ZrSA	Zr–crosslinked SA
AAO	Anaerobic-anoxic–oxic

metal such as vanadium (V), titanium (Ti), molybdenum (Mo), niobium (Nb), or zirconium (Zr), while A is typically from group 13 or 14 elements (e.g., Al, Sc, Ga), and X denotes carbon (C), nitrogen (N), or both [10]. Since their discovery in 2011, MXenes have attracted widespread research interest due to the potential to tune their properties and crystal structures through compositional variations.

Among the MXenes, $Ti_3C_2T_x$ (Ti–MXene) was the first to be synthesized and has been extensively studied for applications in electromagnetic interference (EMI) shielding, supercapacitors, batteries, catalysis, sensors, water splitting, and even therapeutics [11–14]. However, limitations such as oxidation susceptibility, challenges in controlling terminal groups, and reliance on acid-based synthesis have spurred interest in exploring alternative compositions like Mo– and Zr–based MXenes. Zr–based MXenes first reported in 2013, exhibit unique properties that make them promising for energy storage, environmental remediation, corrosion resistance, optoelectronics, photonics, and biomedicine. Their unique chemistry, supported by a Zr backbone, offers tunable properties with the potential for new functionalities.

This review examines recent advancements in Zr–based MXenes, highlighting their diverse applications in energy storage, environmental remediation, and biomedicine. It covers updated synthesis methods, key factors influencing structure, and techniques for characterizing physicochemical properties. Additionally, the review examines emerging uses of Zr–MXenes, especially in energy technologies, and discusses future opportunities and challenges in optimizing their compositions. Fig. 1 summarizes the increasing applications of Zr–based MXenes, which are essential for future sustainable developments, while Fig. 2 shows the growing scientific interest, as evidenced by the increasing number of publications on “Zirconium MXene” in the Web of Science. Over the past decade, Zr–MXenes have emerged as a key research area, driving advancements in both fundamental understanding and practical applications.

2. Zr–based MXenes

2.1. *Theoretical studies*

The rapid advancements in computational material screening have significantly accelerated the identification of promising candidates for applications like energy storage [15], photovoltaic absorbers [16],

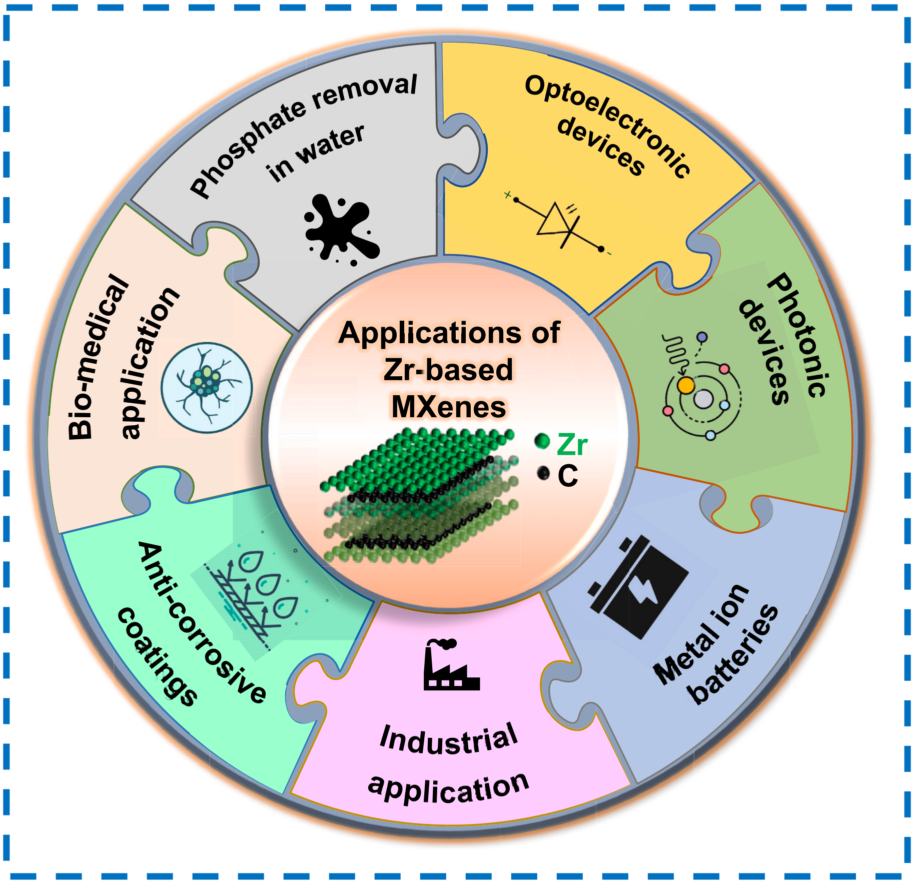

Fig. 1. Different applications of Zr–based MXenes.

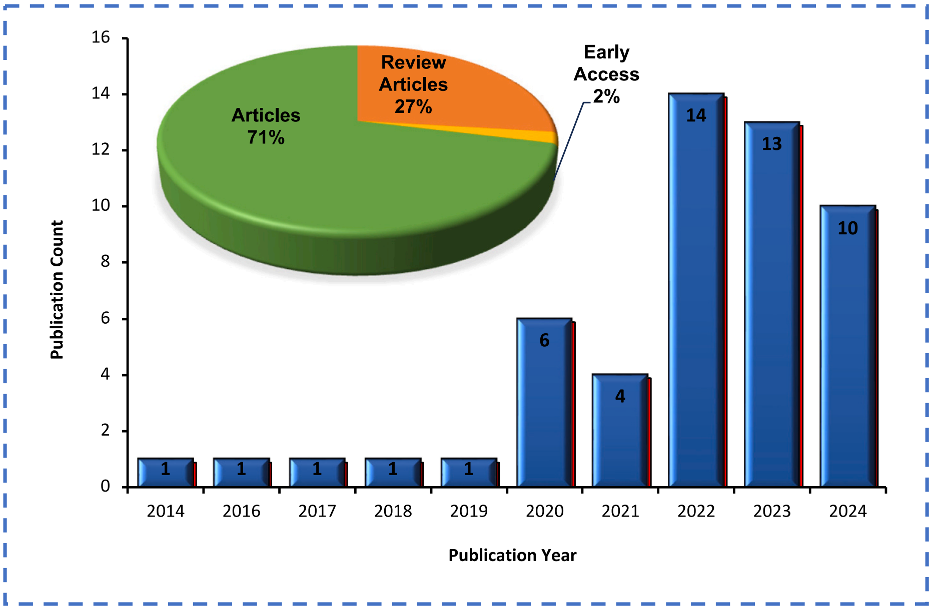

Fig. 2. Current growth of Zr–MXenes based on last ten–year research publications. Source: Web of Science (retrieved on October 2024).

electrocatalysis [17], and various other technological fields [18]. As a result, material databases are rapidly growing, with both experimental and theoretical data on 3D crystals, while recent initiatives have notably expanded the catalogue of proposed 2D materials and their potential properties [19,20]. For instance, Frey et al. [21] used positive and unlabeled (PU) machine learning to assess the synthesizability of theoretically predicted MAX and MXene compounds, including Zr–based MXenes. The study analyzed 66 distinct M atom MXenes, each linked to 12 possible MAX precursors, resulting in approximately 800 unique synthesis pathways. They predicted 111 unsynthesized MAX phases and 18 MXenes to have a high probability of successful synthesis, identifying 20 MAX/MXene pairs with high combined synthesizability,

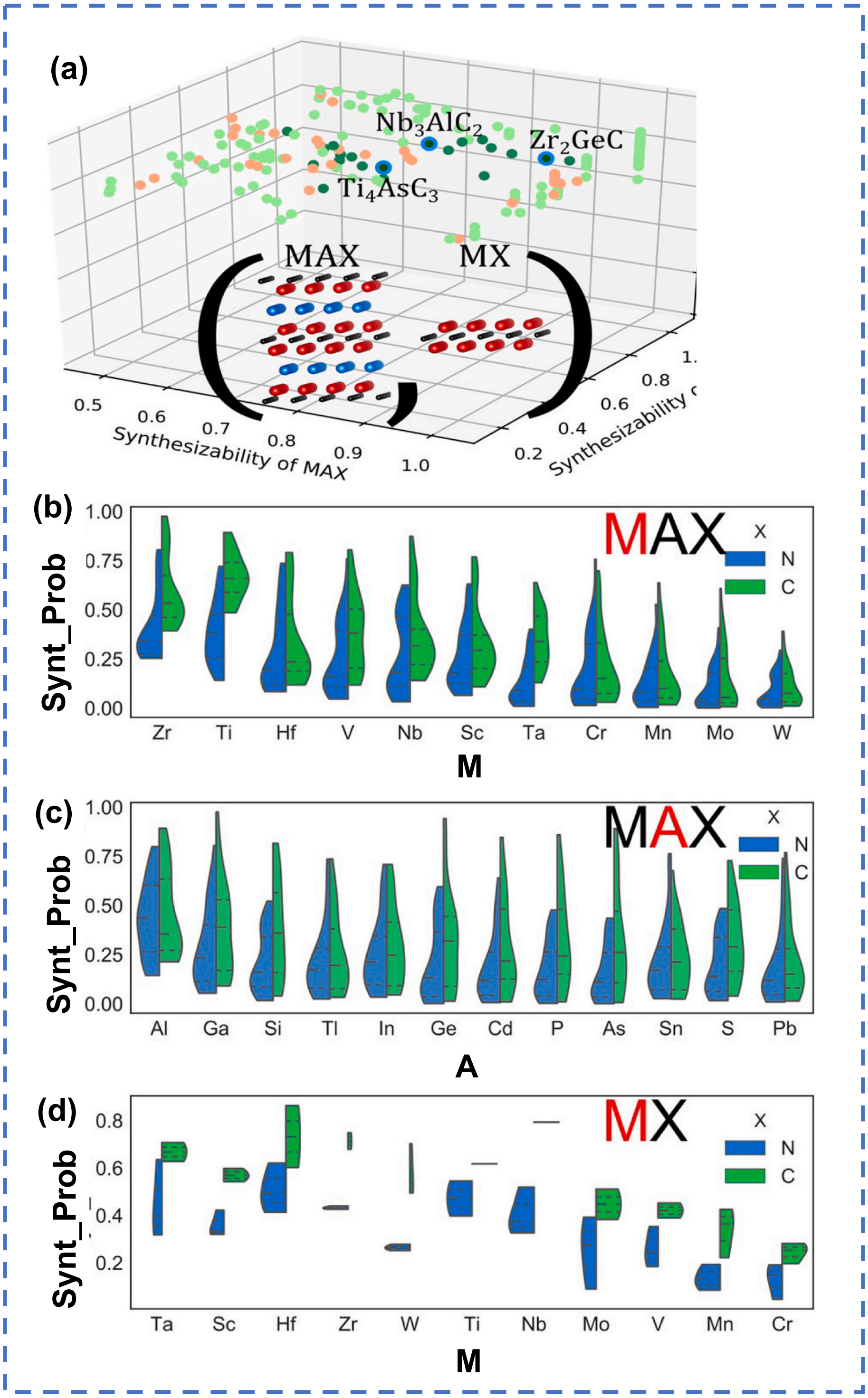

Fig. 3. (a) *k*-means clustering of (MAX, MXene) pair synthesizability as a function of the required chemical etching energy, and individual MAX and MXene synthesizability. Predicted positive samples are represented in light green, the top 20 predicted positive samples are portrayed in dark green, and predicted negative samples are illustrated in orange. The data points for Zr$_2$GeC, Ti$_4$AsC$_3$, and Nb$_3$AlC$_2$ (highlighted in blue) are presented as examples of the highest projected positive samples, (b) Violin plots depicting synthesis probabilities as a function of constituent atomic species (X = N represented in blue, X = C represented in green). MAX synthesis probability as a function of the number of M atoms, (c) MAX synthesis probability as a function of A atom, (d) Probabilities of MXene synthesis as a function of M atom. Reproduced with permission from [21]. (For interpretation of the references to colour in this figure legend, the reader is referred to the web version of this article.)

including Zr–MXene.

Their model utilized elemental data along with structural, thermodynamic, and electronic information derived from density functional theory (DFT) calculations as inputs. After identifying key features for predicting synthesis success, statistical learning techniques, including principal component analysis (PCA), were used to refine the most critical inputs, such as lattice parameters, formation energy, and atomic Bader charges [21]. These features were then applied to clustering and

Table 1
Optimal MAX phase precursors along with the synthesizability of their corresponding MXenes, and the etching energy (e$V/\text{Å}^2$) of the (MAX, MXene) pair. Reproduced with permission from [21].

MAX	Synthesizability of MAX	Synthesizability of MX	Etching energy
Zr_2GaC	0.975	0.748	−0.143
Zr_2GeC	0.942	0.748	−0.152
Zr_2AsC	0.890	0.748	−0.150
Zr_2PC	0.860	0.748	−0.138
Zr_2CdC	0.846	0.748	−0.108
Zr_2SiC	0.816	0.748	−0.131

classification of PU learning models, validated using *k*-fold cross-validation with true positive rates (TPR) measured against 63 experimentally synthesized MAX compounds. Given the limited positive sample size, external validation methods, including phase stability tests and experimental comparisons, were employed. This computational framework offers insights not only for mechanically exfoliating 2D materials but also for liquid exfoliation of any layered materials [21].

Fig. 3(a) illustrates *k*-means clustering results, with highly synthesizable MAX/MXene pairs highlighted in dark green and lower-probability pairs in orange. Etching energy is displayed along the z-axis to enhance visual clarity. The top 20 pairs with the highest combined synthesizability scores are marked, providing a focused direction for future experimental efforts. Table 1 lists these pairs alongside their respective MAX and MXene scores, narrowing the field from 111 favourable MAX phases to specific Zr-based compounds that can be chemically etched into MXenes with a high probability of success.

Fig. 3(b–d) shows violin plots of the predicted synthesis probabilities for various atomic species in MAX and MXene systems. Several patterns emerge, particularly the higher likelihood of carbides (green) being synthesized compared to nitrides (blue). This trend aligns with experimental data, where only 9 (fewer than 15 %) of the known MAX phases are nitrides. For MXenes, this is even more pronounced, as only one nitride, Ti_4N_3, has been synthesized from theMAX phase, skewing the model's predictions toward carbides. This emphasises the need to identify nitride compounds with high synthesis potential. The larger dashed line in the plots represents the median, and the thinner dashed lines indicate the interquartile range. For many species, the interquartile range shows a low probability of synthesis, with some species having a narrower range extending to higher probabilities.

Fig. 3(b) highlights trends in MAX phases based on the M atom. Notably, synthesizability decreases with increasing group number: group 4 elements like Ti, Zr, and Hf exhibit higher synthesis probabilities, while group 6 elements like Mo and W show much lower probabilities. For W, the interquartile range falls entirely below 0.2, consistent with experimental results, where group 4 M atoms dominate known MAX phases, and no W-based systems have been synthesized. The influence of the A atom (Fig. 3(c)) is less pronounced, with the distributions of carbides spread across the entire probability spectrum. Despite Al-based MAX phases being the only ones successfully etched into MXenes, several other A-group elements show potential as MXene precursors. Interestingly, the trend observed in MAX phases does not carry over to MXenes [22]. Further, the hitherto evident trend toward MAX phases is completely absent in the MXenes. Fig. 3(d) shows a surprising number of positive predictions for early transition metal MXenes, except for V, Mn, and Cr. The stark contrast between 3d block elements and others may be due to an artefact, as only nonmagnetic ground states were considered, while some 3d transition metals are expected to exhibit magnetic properties [23,24]. The Ti and Nb carbide violin plots show nearly linear trends at high synthesis probabilities, as only one stacked MXene system from each remains unsynthesized [21].

2.2. Zr MAX phases

Among the over 70 known MAX phases, the Zr family comprises approximately 12 distinct phases, including Zr_2AlC, Zr_2SiC, Zr_2PC, Zr_2SnC, Zr_2GaC, Zr_2SC, Zr_2GeC, Zr_2AsC, Zr_2CdC, Zr_2InC, Zr_2TiC, and Zr_2PbC (collectively referred to as Zr_2AC) [25]. Most of these Zr-based phases have been studied theoretically, with only a few synthesized to date, among which Zr_2C is notable for being a commonly synthesized Zr-based MXene. Nasir et al. [25] investigated the properties of Zr_2AlC, Zr_2SC, Zr_2SiC, and Zr_2PC, noting that all “A” elements (Al, Si, P, S) occupy the same period, imparting unique symmetry-related properties. In these structures, Zr atoms occupy (1/3, 2/3, z), A atoms (2/3, 1/3, 1/4), and C atoms [0,0,0]. The literature indicates that these Zr_2AC MXenes (211 phase) offer high mechanical strength and stability. Their bulk (B) and shear moduli (G) were calculated using Voigt [26], Reuss [27], and Hill approximations. Results show that the bulk modulus increases as A-group elements progress across the periodic table, with a slight drop in Mulliken Bond theory also suggests that Zr–C bonds are stronger and less metallic than Zr–A bonds, with Zr_2AC structures demonstrating higher Zr–C bond strength. Vickers hardness tests reveal values of 5.9 GPa for Zr_2AlC, 7.1 GPa for Zr_2SiC, 7.8 GPa for Zr_2PC, and 6.8 GPa for Zr_2SC, suggesting that Zr_2AlC is relatively softer and more machinable.

Further, $(MC)_n[Al(A)]_mC_{m-1}$ compounds are promising precursors for MXenes and other 2D carbides. Zha et al. [28] identified over 30 related compounds, including $Zr_2Al_3C_4$, $Zr_3Al_3C_5$, $ZrAl_4C_4$, and $Zr_2[Al(Ge)]_4C_5$, etc., which hold potential for MXene synthesis. Zr-based materials offer diverse applications, detailed in Section 4. For example, Chen et al. [29] successfully synthesized a ternary MAX phase, Zr_2SeC, containing chalcogen. A comprehensive analysis of the crystal structure confirmed the presence of selenium (Se) at the A site of the MAX phase. First-principles calculations were employed to predict the optimal crystal structure of Zr_2SeC and to analyze the chemical bonding in comparison to Zr_2SC. It was found that the thermal conductivity of Zr_2SeC is significantly influenced by electronic contributions, particularly at elevated temperatures, which leads to a decrease in thermal conductivity. These findings further highlight the importance of A-site components in modifying the physical characteristics of MAX phases.

2.3. Significance of Zr–based MXenes

Although Ti-based MXenes have been extensively studied for various applications [30], other MXenes, particularly those derived from niobium (Nb) [31], vanadium (V) [32], molybdenum (Mo) [33], and Zr, are increasingly gaining attention. The abundant availability of Zr on Earth and its critical role in alloy preparation for electronics make Zr increasingly appealing for future applications. Despite their potential, Zr-MXenes remain underexplored in the literature, highlighting the need for further investigation. Zr-MXenes can be functionalized with groups such as –O, –F, –OH, and –Cl through various synthesis techniques. However, synthesizing bare MXenes poses challenges due to their high reactivity [34].

First-principles calculations reveal that a novel Zr_2Si MXene exhibits both exceptional stability and an antiferromagnetic ground state [35]. The spins in Zr_2Si MXene are ferromagnetically aligned within each Zr plane but antiferromagnetically coupled between the two Zr planes, forming an anti-parallel configuration. Due to the lack of Coulomb interactions among Zr–4d electrons and the absence of spin–orbit coupling, no linear energy-momentum relationship (Dirac cones) near the Fermi level is observed. Instead, the Dirac cones originate from the $d_{x^2-y^2}$ and d_{z^2} orbitals of Zr display anisotropy in momentum space and Fermi velocities similar to those found in graphene [36]. The introduction of Coulomb repulsion and spin-orbit coupling could render these Dirac cones non-conductive, opening possibilities for electronic applications. Moreover, Zr_2Si MXene transitions between antiferromagnetic and ferromagnetic states, leading to a switch between semiconducting and metallic behaviour, indicating its potential in electronic devices [35]. Zr–based MXenes, particularly ZrC and ZrN, show great

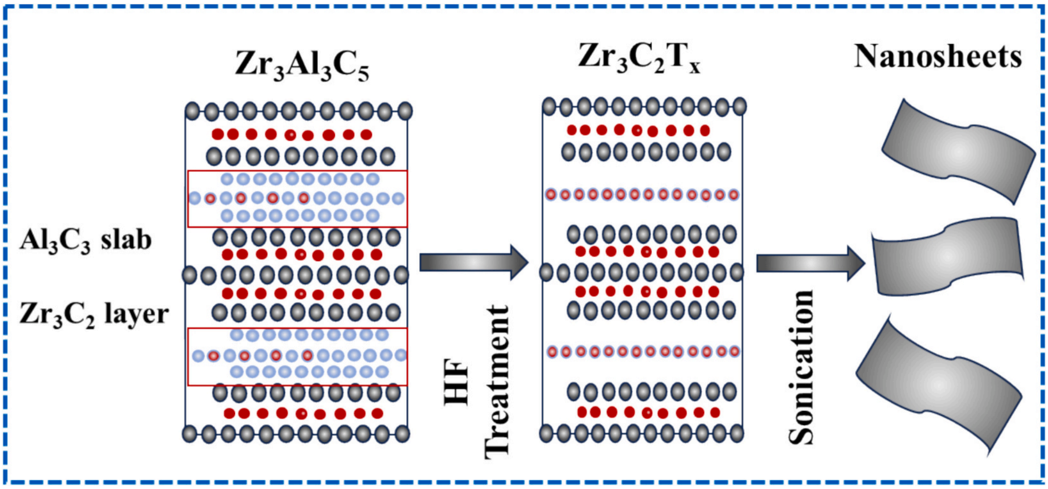

Fig. 4. 2D $Zr_3C_2T_x$ MXene synthesized through selective etching of Al_3C_3 from stacked ternary $Zr_3Al_3C_5$. Reproduced with permission from [47].

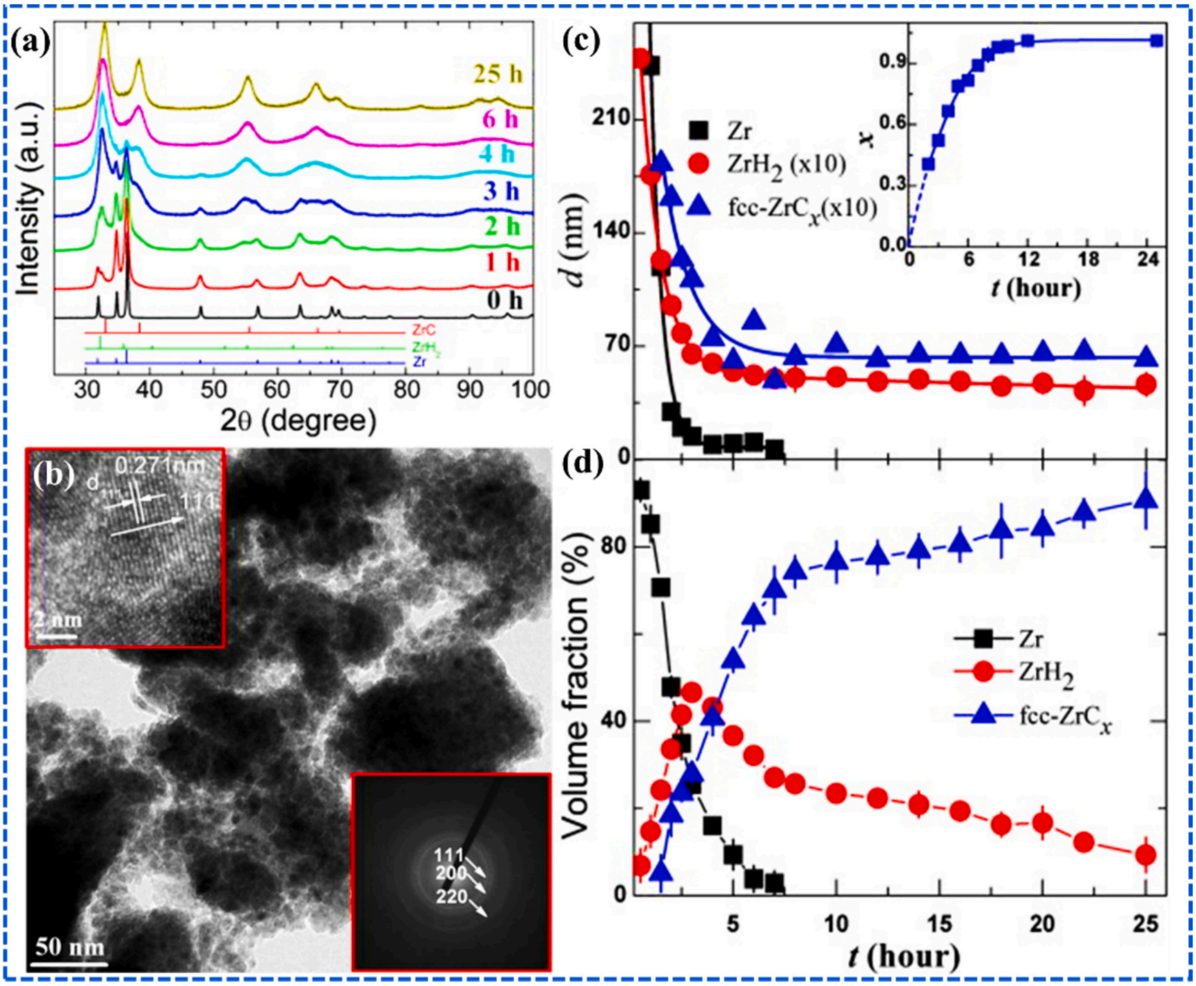

Fig. 5. (a) XRD spectra of as-supplied Zr powder, along with the as-milled powders produced at different durations of milling. The bars in the graph are arranged in descending order and represent ZrC (red, PDF#74–1221), ZrH_2 (green, PDF#73–2067), and Zr (blue, PDF#05–0665), respectively, (b) TEM images of the powders that underwent milling for 25 h. The upper and bottom insets in (b) correspond to the HRTEM image and the SAED rings. The progression of the mean grain size d, (c) and volume fraction, (d) for Zr, ZrH_2, and ZrC_x as a function of milling time (t). For clarity, the grain sizes of ZrH_2 and ZrC_x were scaled by a factor of 10. The inset (c) represents the mean *C* powder content after different milling durations. Reproduced with permission from [49]. (For interpretation of the references to colour in this figure legend, the reader is referred to the web version of this article.)

promise due to their exceptional properties. ZrC, for instance, exhibits high chemical stability [37], high melting point [38], ablation resistance [39], notable wear resistance [40], hardness [40,41], excellent temperature resistance [42], and excellent electrical conductivity [43]. These characteristics make ZrC suitable for applications such as field emitter coatings, wear-resistant epoxy coatings [44], electrode coatings [45], and lubricating barriers for prosthetics [46]. The unique bonding nature of ZrC, combining metallic, ionic, and covalent bonds, facilitates strong photon-electron interactions, creating the potential for a wide range of technological applications [25].

2.4. Synthesis and characterization of Zr derived materials

2.4.1. ZrC MXene by HF etching

Experimental synthesis and characterization of Zr–derived materials, including Zr–MXenes, are crucial for realizing their practical applications and complementing computational studies. In 2016, Zhou et al. [47] first reported the successful synthesis of Zr–MXene by etching $Zr_3Al_3C_5$ with hydrofluoric acid (HF) (Fig. 4). They noted that the efficiency of this HF etching process depends on optimizing parameters such as acid concentration, etchant-to-solute ratio, and temperature. The synthesis process begins with the preparation of $Zr_3Al_3C_5$ MAX phases, commonly achieved via pulsed electric current sintering (PECS). In this process, Zr, Al, and graphite powders are mixed in a molar ratio of 3.3:2.4:8, milled in absolute ethanol for 12 h, and then dried. The powder is cold-pressed and sintered at 1800 °C for 20 min in an argon (Ar) atmosphere. After cooling, the material is ground, sieved, and immersed in 50 wt.% HF at room temperature for 72 h. The etched material is then washed continuously with deionized water, filtered, and dried at room temperature for 48 h, resulting in 2D $Zr_3C_2T_x$ sheets with flexibility similar to graphene [47]. The reactions that occur during the synthesis process are shown in Eqs. (1–3).

$$Zr_3Al_3C_5 + HF \rightarrow AlF_3 + CH_4 + Zr_3C_2 \tag{1}$$

$$Zr_3C_2 + 2\,H_2O \rightarrow Zr_3C_2(OH)_2 + H_2 \tag{2}$$

$$Zr_3C_2 + HF \rightarrow Zr_3C_2F_2 + H_2 \tag{3}$$

The final structure of Zr-based MXene is a hexagonal Zr–C layer, which is shared with one C layer and an Al–C layer [47].

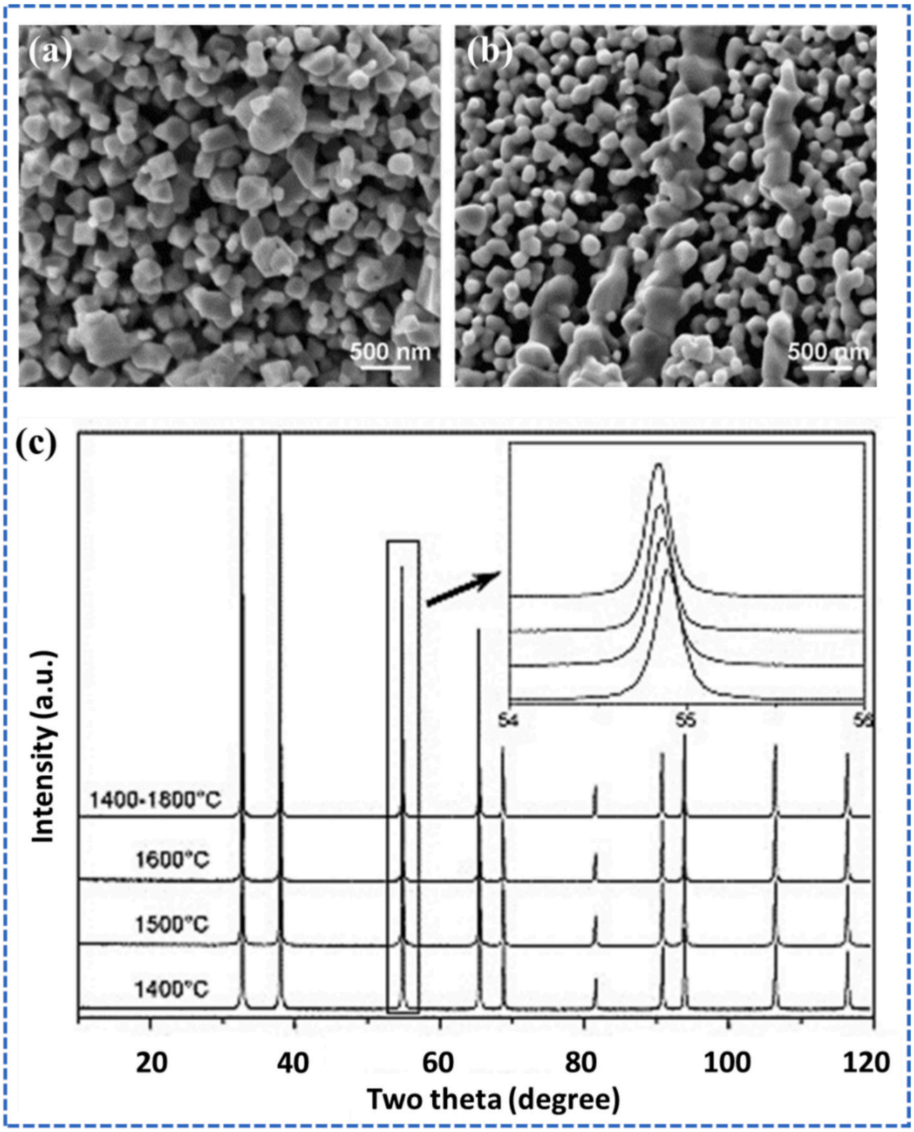

Fig. 6. Morphology of nanosized ZrC (a) SEM image of an agglomerate microstructure for a sample heat treated at 1600 °C for 3 h, (b) SEM image of an agglomerate microstructure for a sample heat treated at 1400 °C then at 1800 °C for 6 min, (c) XRD patterns of the different samples as a function of their respective heat treatment under Ar flow. Reproduced with permission from [50].

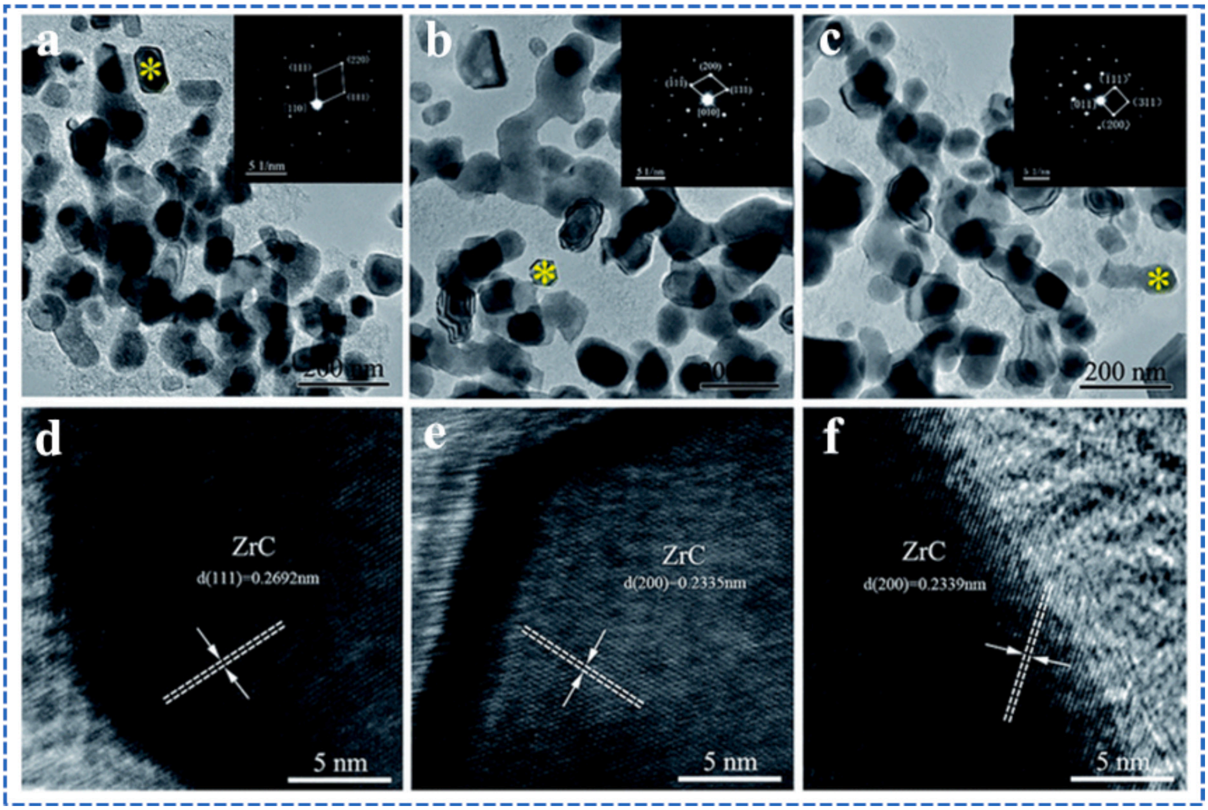

Fig. 7. TEM and HRTEM images of ZrC powders synthesized from precursors with varying ratios of $ZrO(CH_3COO)_2$: $C_{12}H_{22}O_{11}$: (a and d) 4:1.5, (b and e) 4:1.2, (c and f) 4:1. SAED patterns for ZrC particles are displayed in (a), (b), and (c) at the * position. Reproduced with permission from [51].

2.4.2. *Zr carbide by planetary milling*

Zr carbide (ZrC) is a non-stoichiometric compound with a face-centred cubic (FCC) structure characterized by a combination of ionic, covalent, and metallic bonds [48]. This unique bonding contributes to the exceptional physical and chemical properties of ZrC. Xiang et al. [49] developed a method for synthesizing ZrC nanopowder by milling Zr powder with toluene, noting that the milling time significantly affects the Zr_3C_x peak. The milling process was conducted in a planetary mill using tungsten carbide vials, with a ball–to–Zr ratio of 13:1 and a toluene–to–Zr powder ratio of 3:1, all within a pure Ar atmosphere, where toluene serves as the carbon source for Zr_3C_x. The milling was performed at 400 rpm in tightly sealed vials, resulting in a paste-like consistency, which was subsequently placed in a vacuum chamber for 20 h at 80 °C to remove residual toluene. The bulk Zr_3C_x was then sintered for 5 min using spark plasma sintering at 1200 °C under a pressure of 50 MPa. The synthesized Zr_3C_x exhibited an average particle size of approximately 5 μm. The carbon content of the samples was determined through an oxidation process, and density was calculated using the Archimedes technique. Vickers indentation was performed by applying a 300 g weight for 10 s using a diamond indenter.

Fig. 5(a) exhibits the X-ray diffraction (XRD) spectra of the original Zr powder and powders milled for various durations (1, 2, 3, 4, 6, and 25 h). With increasing milling time, the diffraction peaks of hexagonal close-packed (HCP) Zr diminished, broadened, and disappeared entirely after 6 h. Additionally, two phases, FCC ZrH_2 and FCC ZrC_x, emerged in the XRD spectra. In the early milling stage (<3 h), ZrH_2 was the predominant phase, while reflection peaks for ZrC_x began appearing after 1 h, increasing in intensity and dominating after 3 h. Fig. 5(b) presents TEM and HRTEM images of nanoparticles obtained after 25 h of milling, revealing significant agglomeration with an average particle size under 10 nm, closely matching an average grain size of about 7 nm. HRTEM images confirm the nanoparticles' single crystalline structure, and the SAED rings (lower right inset of Fig. 5(b)) and HRTEM images, along with XRD patterns, indicate an FCC structure. Previous studies suggest that milling Zr in toluene may induce an allotropic transformation from HCP to FCC crystal structures, attributed to the reduction in Zr particle size during milling.

Fig. 5(c) and (d) illustrate the evolution of the Zr, ZrH_2, and ZrC_x phases in terms of volume fraction and grain size with milling duration. In the initial hour, the Zr phase decreases significantly in both volume fraction and particle size, with grains rapidly reaching below 10 nm. After 6 h, the Zr phase becomes undetectable in XRD. ZrH_2 production peaked within the first 3 h but began to decline as milling continued, while the formation of the ZrC_x phase accelerated after 1 h, correlating with milling time. Throughout the early milling stage, both ZrH_2 and ZrC_x grains remained at nanoscale, ultimately reaching approximately 7 nm. After 25 h, the volume fraction of ZrC_x reached at 90 %, indicating that the nanoparticles were primarily composed of the ZrC_x phase. The inset of Fig. 5(c) shows that the average carbon content increased with milling time, reaching a value of 1 when the duration exceeded 10 h [49].

2.4.3. *Zr carbide by sol-gel method*

The synthesis of ZrC via the sol-gel method involves Zirconium (IV) n-propoxide ($Zr(OPr)_4$) in 70 % propanol, acetic acid (AcOH) and saccharose as the precursors. The process begins by dissolving saccharose in AcOH at 80 °C. After cooling to room temperature, $Zr(OPr)_4$ is added under continuous stirring, causing the solution to turn brown and form a viscous gel structure. The remaining AcOH is then evaporated at 80 °C, leaving behind acetates. The resulting gel is dried at 120 °C to produce a powder, which is ground and subjected to carbothermal reduction at 1400 °C and 1800 °C for 3 h under Ar atmosphere.

Key steps in synthesizing the precursor involve forming metal chelates, transesterification, and hydrolysis-condensation reactions. The introduction of $Zr(OPr)_4$ into acetic acid initiates a transformation that produces zirconium propoxide diacetate ($Zr(OAc)_2(OPr)_2$). This

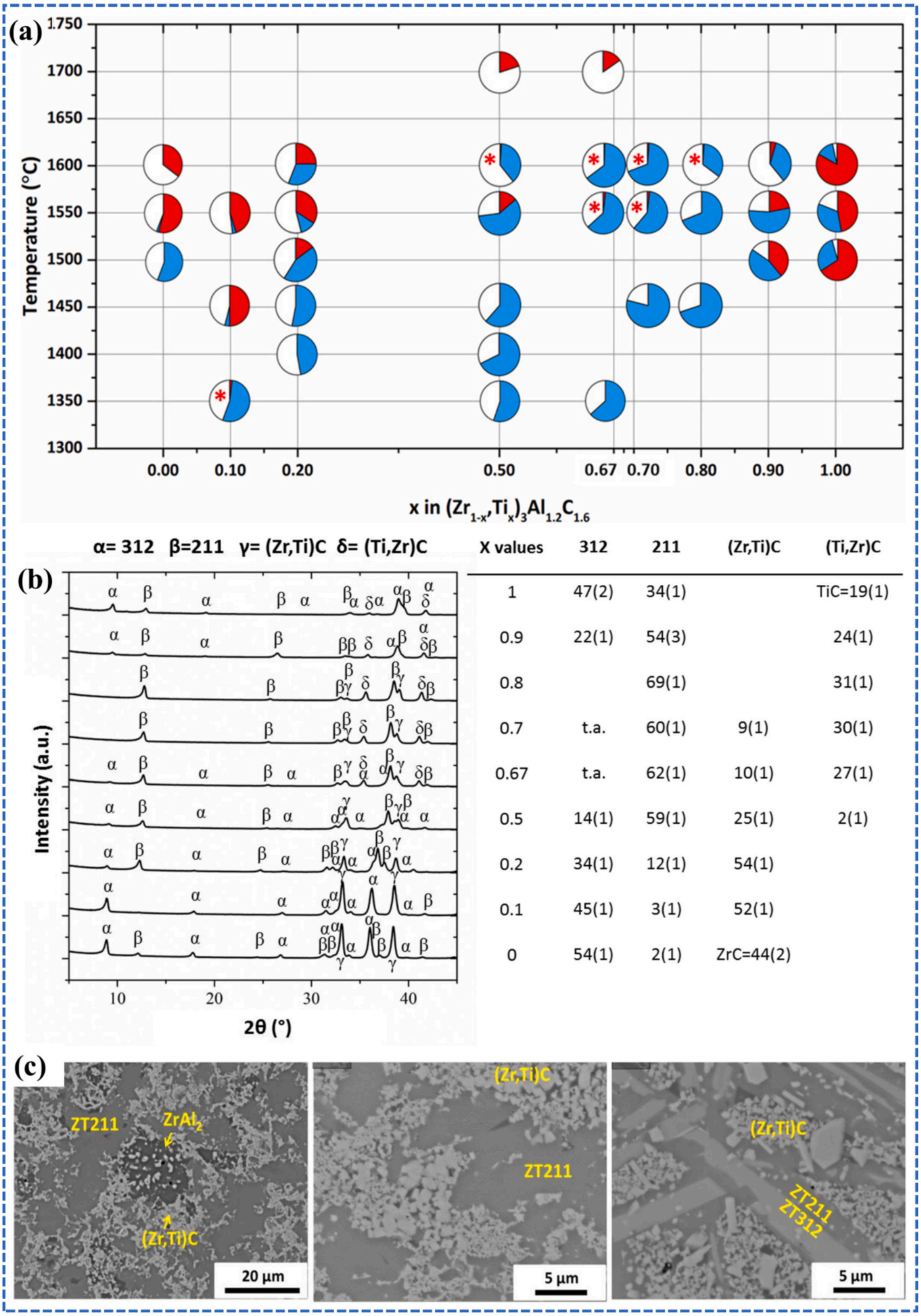

X values	312	211	(Zr,Ti)C	(Ti,Zr)C
1	47(2)	34(1)		TiC=19(1)
0.9	22(1)	54(3)		24(1)
0.8		69(1)		31(1)
0.7	t.a.	60(1)	9(1)	30(1)
0.67	t.a.	62(1)	10(1)	27(1)
0.5	14(1)	59(1)	25(1)	2(1)
0.2	34(1)	12(1)	54(1)	
0.1	45(1)	3(1)	52(1)	
0	54(1)	2(1)	ZrC=44(2)	

Fig. 8. (a) Map illustrating the phase assembly of MAX phase ceramics synthesized in the Zr–Ti–Al–C network, as a function of the hot-pressing temperature and the Ti content, x, in the $(Zr_{1-x},Ti_x)_3Al_{1.2}C_{1.6}$ starting powder. The phase assembly of the MAX phase ceramics is illustrated using pie charts depicting the mass % of each phase: ZT312 in red, ZT211 in blue, and the secondary phase in white. Red asterisks indicate a minimal presence of the ZT312 phase, (b) XRD patterns and phase assembly in ceramics hot-pressed at 1550 °C as a function of the $(Zr_{1-x},Ti_x)Al_{1.2}C_{1.6}$ starting powder composition. Values in parentheses indicate the uncertainty in the last digit of mass% values, (c) BSE images of $(Zr_{0.8},Ti_{0.2})_3Al_{1.2}C_{1.6}$ ceramics hot-pressed at: 1400 °C, 1450 °C, and 1500 °C. Reproduced with permission from [52]. (For interpretation of the references to colour in this figure legend, the reader is referred to the web version of this article.)

carboxylatoalkoxide can participate in several competitive reactions. The first one involves the transesterification of alkoxy groups in $Zr(OAc)_2(OPr)_2$ with the hydroxyl groups of saccharose, as shown in Eq. (4).

$$PrO - Zr(OAc)_2(OPr) + HO - X - (OH)_7 \rightarrow PrO - Zr(OAc)_2 - O - X - (OH)_7 + PrOH \tag{4}$$

where X is a simplified notation for $C_{12}H_{14}O_3$.

Subsequently, unreacted acetic acid reacts with propanol (the solvent and product of the previous reaction) to form water and propyl acetate, as indicated in Eq. (5).

$$AcOH + PrOH \rightleftharpoons PrOAc + H_2O \tag{5}$$

This generated water then participates in a substitution reaction with $Zr(OAc)_2(OPr)_2$, where hydroxyl groups replace propoxy groups (Eq. (6)).

$$Zr(OAc)_2(OPr_2) + H_2O \rightarrow Zr(OAc)_2(OPr)OH + PrOH \rightarrow Zr(OAc)_2(OH)_2 + PrOH \tag{6}$$

Since water is continuously consumed for hydrolysis, Eq. (5) shifts toward the right, which is maintained by a high acetic acid/Zr molar ratio, ensuring a complete reaction [50].

Fig. 6(a) and (b) show heat-treated samples at 1400 °C and 1800 °C, respectively, where particles exhibit a uniform size distribution and increased sphericity due to partial surface melting. XRD patterns (Fig. 6 (c)) confirm the formation of a single-phase structure, with peak shifts toward lower angles as temperature rises, indicating an increase in lattice parameter, as supported by Rietveld refinement.

2.4.4. Nano crystallized Zr carbide based on an aqueous solution-derived precursor

Nano-crystallized ZrC powder was synthesized through an aqueous solution-based method, using Zr acetate and sucrose ($C_{12}H_{22}O_{11}$) as primary reagents. These were combined with polyvinyl pyrrolidone (PVP) to create a suitable precursor for ZrC synthesis. This aqueous approach allows for fine-scale mixing in an environmentally friendly way. The precursor was subjected to carbothermal reduction at 1600–1650 °C, yielding ZrC powder with an ultra-fine particle size of 50–100 nm and an oxygen content below 1.0 wt.% due to minimal residual free carbon. The conversion process from pre-ceramic precursor to ZrC powder was comprehensively studied using FTIR, TG-DSC, XRD, Raman spectroscopy, SEM, and TEM analyses.

The initial Zr acetate (99 % purity) and $C_{12}H_{22}O_{11}$ were mixed in a molar ratio of 4:1, with the PVP concentration in the precursor solution maintained at approximately 2 wt.%. The ingredients were dissolved in DI water and stirred continuously for 24 h to form a homogenous precursor solution. The precursor then underwent cross-linking and curing at 85 °C for 12 h in a drying oven, followed by pyrolysis at 600 °C for 2 h under an Ar flow, with a heating rate of 1 °C min^{-1}. The pyrolyzed precursor was subsequently heat-treated at 1400–1650 °C for 2 h under vacuum, with a heating rate of 5 °C min^{-1}, to complete the carbothermal reduction. The resulting ZrC compounds were ground into fine powders for further characterization.

Fig. 7 presents TEM and HRTEM images of ZrC particles synthesized with varying ratios of $ZrO(CH_3COO)_2$ as a precursor. SEM insets in Fig. 7(a–c) show equiaxial particles with cubic crystalline structures consistent with ZrC, with particle sizes of 56, 60, and 61 nm. Reducing the initial concentration of $C_{12}H_{22}O_{11}$ significantly decreases amorphous free carbon, as even 0.5 wt.% of residual free carbon effectively inhibits ZrC grain coarsening. Further reductions in $C_{12}H_{22}O_{11}$ may lead to notable grain coarsening or the formation of ZrO_2 impurities. Notably, HRTEM images in Fig. 7(d–f)) display lattice fringes with interlayer distances between 0.23 and 0.27 nm, corresponding to the (200) or (111) planes of ZrC. The lattice parameter calculated from these fringes aligns closely with values obtained from XRD measurements, confirming the presence of non-stoichiometric $Zr_{1-x}C$. Non-stoichiometric, nanoscale $Zr_{1-x}C$ powders are anticipated to offer advantages for subsequent sintering and densification processes in material engineering.

2.4.5. Synthesis Zr MAX phase through reactive hot-pressing and pressureless-sintering

The synthesis of MAX phases involved combining ZrH_2, TiH_2, Al, and C powders as initial materials, with a Zr:Ti:Al:C ratio of [3(1 − x)]:[3x]:[1.2]:[1.6], where x varied from 0 to 1 in increments of 0.1. This approach allowed for the investigation of a broad range of Ti and Zr concentrations on the M site of the resulting MAX phases. The starting stoichiometries were selected to achieve a 312 stoichiometry, incorporating a higher Al content to compensate for potential losses during melting while maintaining a lower carbon content to account for interdiffusion caused by the graphite die/punch arrangement in the hot press. Prior studies on Zr–Al–C MAX phases informed the choice of 312 stoichiometry, as these had shown the formation of off-stoichiometric phases. For the synthesis of 211 and 312 phases, the initial powder mixes corresponded to the 312 and 413 stoichiometries.

The powders underwent a 48-h dry mixing process in ambient air using a Turbula-type multidirectional mixer. Subsequently, the mixed powders were cold pressed at a pressure of 30 MPa using a graphite die with a 30 mm interior diameter. Following this, the powder compacts were hot pressed under a vacuum at approximately 10 MPa, with a heating rate of 25 °C min^{-1} and a dwell time of 30 min at temperatures ranging from 1350 to 1700 °C. Pressureless sintering was also performed, where powder compacts were cold-pressed at 30 MPa and subjected to similar thermal changes as the hot-pressed samples. This approach successfully synthesized both the 211 (ZT211) and 312 (ZT312) MAX phases using various mixtures of $(Zr_{1-x}, Ti_x)_3Al_{1.2}C_{1.6}$.

Fig. 8(a) illustrates the evolution of the MAX phases (ZT211 and ZT312) based on hot-pressing temperatures and the atomic fraction x of Ti in the initial powder. The pie charts represent the hot-pressed ceramics, with each phase detected by XRD analysis assigned a distinct colour. All ceramics contained ternary carbides rich in Zr and/or Ti, while only those primarily composed of Zr and Ti exhibited binary ZrC and TiC carbides. Intermetallic compounds, such as $ZrAl_2$, $ZrAl_3$, or Zr_2Al_3 were detected in samples hot-pressed below 1550 °C. Distinct trends in the formation of MAX phases were observed: the ZT211 phase consistently appeared in ceramics hot pressed at temperatures between 1350 and 1600 °C, except for those with a low Ti concentration ($x = 0.1$). The ZT312 phase exhibited stability within the 1450–1550 °C range but was absent at 1450 °C for other stoichiometries. Notably, minimal quantities of ZT211 were detected when this specific stoichiometry was subjected to hot pressing at 1450 °C, suggesting that a small amount of Ti stabilizes the ZT312 phase, which is challenging to achieve at higher Ti concentrations. At x values of 0.5, 0.67, 0.7, and 0.8, ceramics hot pressed at 1600 °C showed very low quantities of ZT312 as measured by XRD. The highest concentration of MAX phases (approximately 85 % by mass) was observed at 1500 °C when x was 0.9.

Fig. 8(b) displays XRD data from a comprehensive set of hot-pressed ceramics at 1550 °C, where Zr-rich ternary carbide is denoted as (Zr,Ti)C and Ti-rich ternary carbide as (Ti,Zr)C. Backscattered electron (BSE) images in Fig. 8(c) illustrates microstructures of $(Zr_{0.8},Ti_{0.2})_3Al_{1.2}C_{1.6}$ ceramics hot-pressed at temperatures between 1400 and 1500 °C. At 1400 °C, large $ZrAl_2$ grains were observed within a ZT211 matrix containing fine grains of (Zr,Ti)C. At 1450 °C, there was a reduction in intermetallic compounds alongside an increase in the size of mixed carbides, although the ZT312 phase did not form. By 1500 °C, elongated ZT312 grains surrounded by ZT211 grains were detected, with the (Zr, Ti)C grains distributed within a composite matrix of ZT211 and $ZrAl_2$.

After hot pressing, solidified remnants were found on the die/punch setup, indicating material loss during processing. Liquid byproducts may have been compressed into the gaps of the die/punch arrangement, resulting in residual substances. Tunca et al. [52] identified pressureless

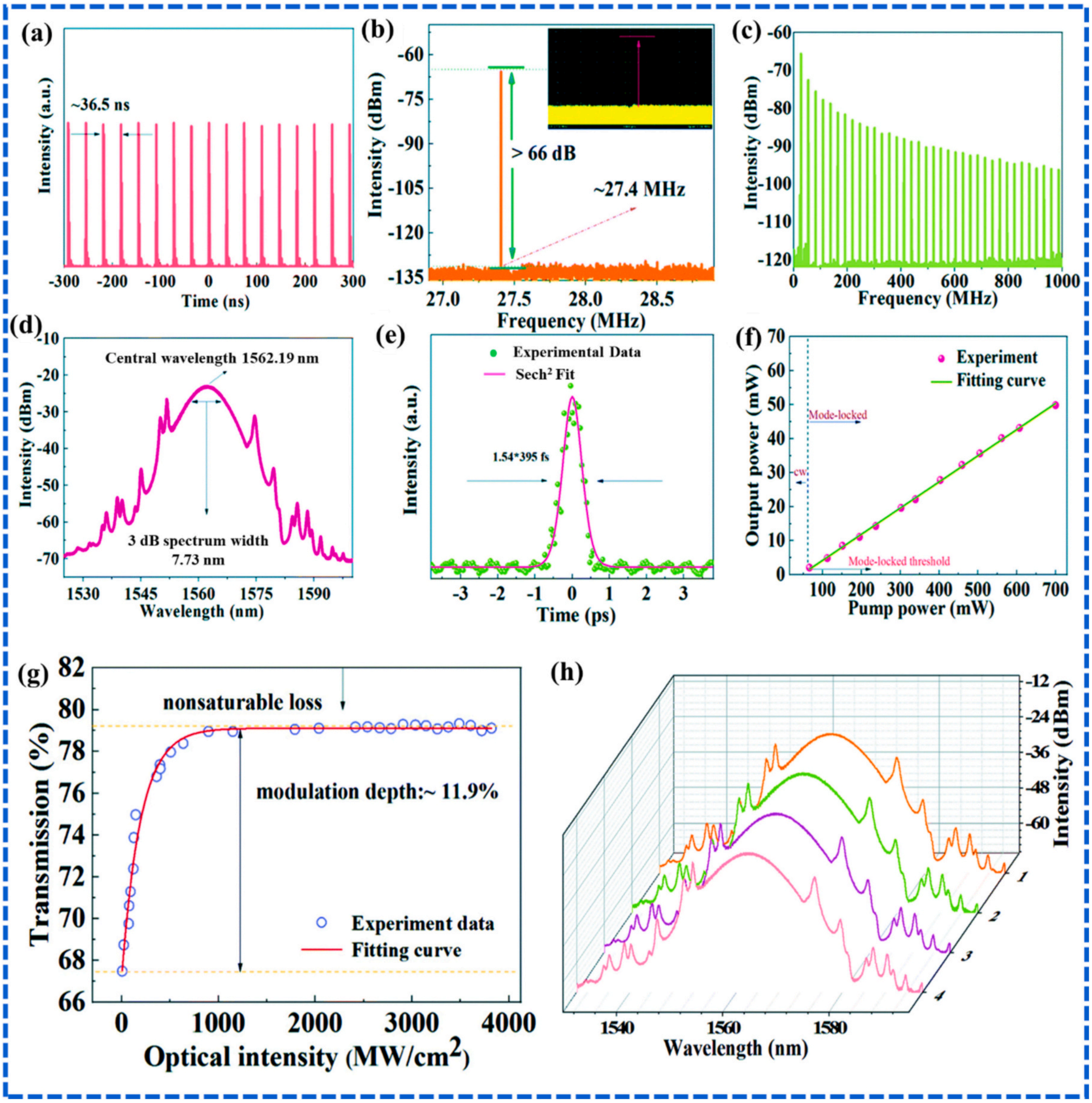

Fig. 9. (a) Oscilloscope trace, (b) RF spectrum, (c) RF spectrum is inside the 1 GHz range, (d) Optical spectrum, (e) Pulse profile, (f) Incident pump power vs. output average power, (g) Nonlinear optical characteristics of the ZrC film, (h) Output optical spectrum measured every hour. Reproduced with permission from [37].

sintering as an alternative technique for synthesizing MAX phases in the Zr–Ti–Al–C system, yielding a higher content of MAX phases with fewer secondary carbides compared to hot-pressed ceramics, potentially due to reduced liquid phase losses. Further refinement of processing methods is required to achieve ceramics with a high level of phase purity within this MAX phase system.

2.5. Properties of Zr–based MXenes

2.5.1. Structural properties

The structural properties of Zr-based MXenes are critical in determining their performance, stability, and versatility. Zhou et al. [47] characterized the structural properties of 2D $Zr_3C_2T_x$ synthesized through HF etching. Thermal gravimetric analysis (TGA) indicated a 4 % mass loss between 50 and 500 °C, attributed to physisorbed water, which was validated by differential scanning calorimetry (DSC) showing an endothermic peak at 71 °C. No significant mass change was observed by 700 °C in TGA, while DSC revealed an exothermic peak, indicating structural rearrangement rather than decomposition. XRD patterns confirmed the formation of the Zr_3C_2 phase along with residual $Zr_3Al_3C_5$. $Zr_3C_2T_x$ demonstrated better structural integrity and maintained a 2D morphology, as evidenced by TGA–DSC and XRD analyses [47]. The stability of Zr–MXenes over a wide temperature range is attributed to their excellent binding energy, making them suitable for various temperature–related applications.

Zr_3C_2 MXene exhibits a quintuple-layered structure arranged in a Zr–C–Zr–C–Zr sequence, consisting of three zirconium layers alternated with two carbon layers. Both Zr_2C and Zr_3C_2 MXenes exhibit hexagonal structures, with lattice constants of 3.32 Å and 3.34 Å, respectively. The structural stability can be evaluated by comparing their total relative energy with stability following the sequence a > b > c. The magnetic properties of Zr_3C_2 are similar to those of Ti_3C_2, while Zr_2CO_2 and $Zr_3C_2O_2$ are non-magnetic in their ground states. The electric and magnetic characteristics of these MXenes can be altered by modifying surface groups and geometrical conformations. The presence of a dispersive electron cloud is crucial for stabilizing the adsorption of multilayer sodium (Na) atoms [53,54].

Further, Meng et al. [53] reported on the electron localization functions (ELF) for the (110) plane of $Zr_3C_2O_2$, focusing on both single-layer and two-layer Na atoms. Their findings illustrated the formation of a negatively charged cloud around single-layer Na atoms due to the electron presence on the Na layer, facilitating the migration of electrons from inside to the outermost surface of Na atoms. Furthermore, these electrons were evenly distributed among the Na atoms, ensuring consistent attractive interactions with the outer layer.

The researchers conducted a comprehensive analysis of the adsorption coefficients for second-layer Na atoms across five systems, concluding that the energy differences in Na atom adsorption onto MXenes are primarily influenced by the lattice constant variations among the MXenes and the Na bilayer. The observed energy differences for $Zr_3C_2O_2$ (−0.059 eV), $Ti_3C_2S_2$ (−0.01 eV), and $Ti_3C_2O_2$ (0.033 eV) correlate with corresponding lattice mismatches of 7.5 %, 10.3 %, and 15.5 %, respectively. Additionally, charge transfer values for the Ti_3C_4, Zr_2CO_2, and $Zr_3C_2O_2$ systems were recorded at −0.46, −0.49, and −0.51, respectively. When lattice mismatches are small, the adsorption energies of second–layer Na atoms (−0.03 eV, −0.054 eV, and −0.059 eV) exhibit a similar trend to the charge transfer values.

It was concluded that significant charge transfer and minimal lattice mismatch favour the adsorption of second–layer Na atoms. The relative stability of second-layer Na atom adsorption on $Zr_3C_2O_2$ compared to Ti_3C_4, Zr_2CO_2, $Ti_3C_2O_2$, and $Ti_3C_2S_2$ MXenes can be attributed to differences in charge density and lattice mismatch. Notably, $Zr_3C_2O_2$ MXene demonstrated a higher number of transferred electrons compared to Zr_2C, Zr_3C_2, and Zr_2CO_2 MXenes, indicating stronger bonding between Na and $Zr_3C_2O_2$. This observation aligns with computed adsorption energy (E_ad) outcomes, suggesting that substantial energy requirements for adsorption and significant charge transfer indicate a robust electrostatic interaction between adsorbed Na atoms and ZrC MXenes.

The charge density difference analysis revealed distinct behaviours in second-layer Na adsorption among Zr_2CNa_2, $Zr_3C_2Na_2$, $Zr_2CO_2Na_2$, and $Zr_3C_2O_2Na_2$ MXenes. The configurations $Zr_2CO_2Na_2$ and $Zr_3C_2O_2Na_2$ exhibited higher electron acceptance compared to Zr_2CNa_2 and $Zr_3C_2Na_2$, indicating stronger bonding interactions, which aligns with findings from E_ad calculations [53].

2.5.2. Optical properties

The frequency-dependent dielectric function ($\varepsilon(\omega) = \varepsilon_1(\omega) + i\varepsilon_2(\omega)$) is essential for understanding electronic band structures, where ω represents the frequency of light and ε(ω) is the dielectric function. Key optical properties, such as absorption spectrum, reflectivity, optical conductivity, refractive index, and loss function are derived from the real and imaginary components, $\varepsilon_1(\omega)$ and $i\varepsilon_2(\omega)$, respectively. Variations in inter- and intra-band transitions in metallic compounds are influenced by changes in the dielectric function. Studies indicate that the MAX phase Zr_2AC (where A = Al, Si, P, or S) exhibits a metallic-like band structure. For Zr MAX phases along the [55] polarization direction, the static refractive indices are $Zr_2AlC = 56.3$, $Zr_2SiC = 56.4$, $Zr_2PS = 56.4$, and $Zr_2SC = 56.3$ [25]. The refractive index aligns with the incident photon energy along this polarization plane, and the excitation coefficient remains consistent across most of the energy spectrum, except between 1 and 6 eV.

The absorption spectra of Zr_2AC phases begin at zero, reflecting their metallic nature, with notable absorption peaks at 6.02 eV, 7.02 eV, 7.51 eV, and 7.21 eV for Zr_2AlC, Zr_2SiC, Zr_2PC, and Zr_2SC, respectively. Another significant optical property is the bulk plasma frequency (ω_p), which corresponds to the maximum peak in the energy loss spectrum where $\varepsilon_2 < 1$ and $\varepsilon_1 = 0$. For Zr_2AC compounds, ω_p values range between 13.2 and 14.9 eV [25]. Additionally, the reflectivity spectra of these materials show a significant increase in the ultraviolet and infrared regions within the 4.8 to 9.8 eV range [25]. Recent studies demonstrate that reflectivity values consistently exceed 44 % for Zr_2AlC, Zr_2SiC, and Zr_2PC, contributing to their metallic grey appearance. Moreover, their ability to effectively reduce solar heating suggests potential applications in minimizing solar heat absorption [56,57].

In a practical application, integrating ZrC as a saturable absorber (SA) within a ring laser cavity enabled effective mode-locking through adjustments to the polarization controller and pump power. Initially, the laser operated in continuous wave mode at a pump power of 45 mW. A stable mode-locked pulse output was subsequently achieved upon increasing the pump power to 66 mW, resulting in an output power of approximately 2.11 mW. Fig. 9(a–f) summarizes the characteristics of the passive mode-locked laser. Fig. 9(a) presents the oscilloscope trace of the pulse train, which exhibits a pulse interval of 36.5 ns and minimal jitter, confirming stable mode-locking conditions. The radio frequency (RF) spectrum at a repetition rate of 27.4 MHz is depicted in Fig. 9(b), showing no additional frequency components, with the inset highlighting a signal peak in the RF spectrum and a signal-to-noise ratio (SNR) of approximately 66 dB, indicating satisfactory stability.

Fig. 9(c) and (d) illustrate the extended range spectrum and the optical spectrum, respectively, with a 3 dB bandwidth of approximately 7.73 nm and a center wavelength of 1562.19 nm. The presence of Kelly sidebands in the output spectrum confirms soliton mode-locking, which is associated with interference among dispersive waves [58,59]. Fig. 9 (e) displays the oscillation trace of the pulse, revealing a full width at half maximum (FWHM) of about 607 femtoseconds (fs), corresponding to a pulse length of 395 fs, determined by fitting the sech^2 function. The temporal bandwidth product (TBP) value of 0.375 exceeds the transformation limit, indicating mild chirping of the pulses. Fig. 9(f) illustrates the correlation between pump power and average output power, demonstrating linear growth throughout the mode-locked operational range, with a peak output power of 49.86 mW at a pump power of 700 mW.

Additionally, the nonlinear optical properties of the ZrC film were also examined using a mode–locked ultrafast laser setup with a wavelength of 1550 nm, pulse duration of 580 fs, and repetition frequency of 30 MHz. The nonlinear transmission curve vs. incoming intensity was generated using a balanced twin-detector and optical coupler, enabling simultaneous measurement of the optical power transmitted through the SA and the reference light, as shown in Fig. 9(g). Fig. 9(h) presents the output spectra over a designated time interval, assessing the long-term stability of the fiber laser, with the data demonstrating consistent pulse behaviour and no noticeable changes in wavelength over a 4 h period. Furthermore, experiments removing the SA confirmed the inability to restore mode-locked behaviour, validating the efficacy of ZrC films as photonic devices for generating mode-locked pulses [37].

2.5.3. Mechanical properties

The mechanical strength of Zr–MXene materials is crucial for various applications due to their remarkable durability. When transition metal carbides, like Zr–MXenes are incorporated into composite materials, they enhance mechanical strength by reinforcing intergranular bonds through diffusion, leveraging phase compatibility between carbide ions and high–temperature ceramics [60]. This enhanced bonding is attributed to the phase compatibility between carbide ions and high-temperature ceramic materials. The MXene surface groups establish strong M–X bonds, which may be ionic or covalent, functioning as “carbide nanofillers” that contribute to forming C–vacancy carbides [61,62].

Zhou et al. [47] highlighted the metallic properties of three functionalized $Zr_3C_2T_2$ MXenes (T = −O, −F, −OH), with $Zr_3C_2O_2$ demonstrating the highest mechanical durability, indicated by a C_{11} elastic modulus of 392.9 GPa. Comparative studies revealed that $Zr_3C_2T_z$ MXene exhibited superior structural stability relative to $Ti_3C_2T_z$ under both vacuum and Ar environments. The advent of 2D $Zr_3C_2T_z$ MXenes holds promise for diverse applications, particularly in high-temperature environments, including their roles as electrodes in electrical energy storage systems, reinforcing additives in polymer composites, and various sensor and catalytic applications. The enhancement of specific strength and modulus in ceramics by incorporating second-phase

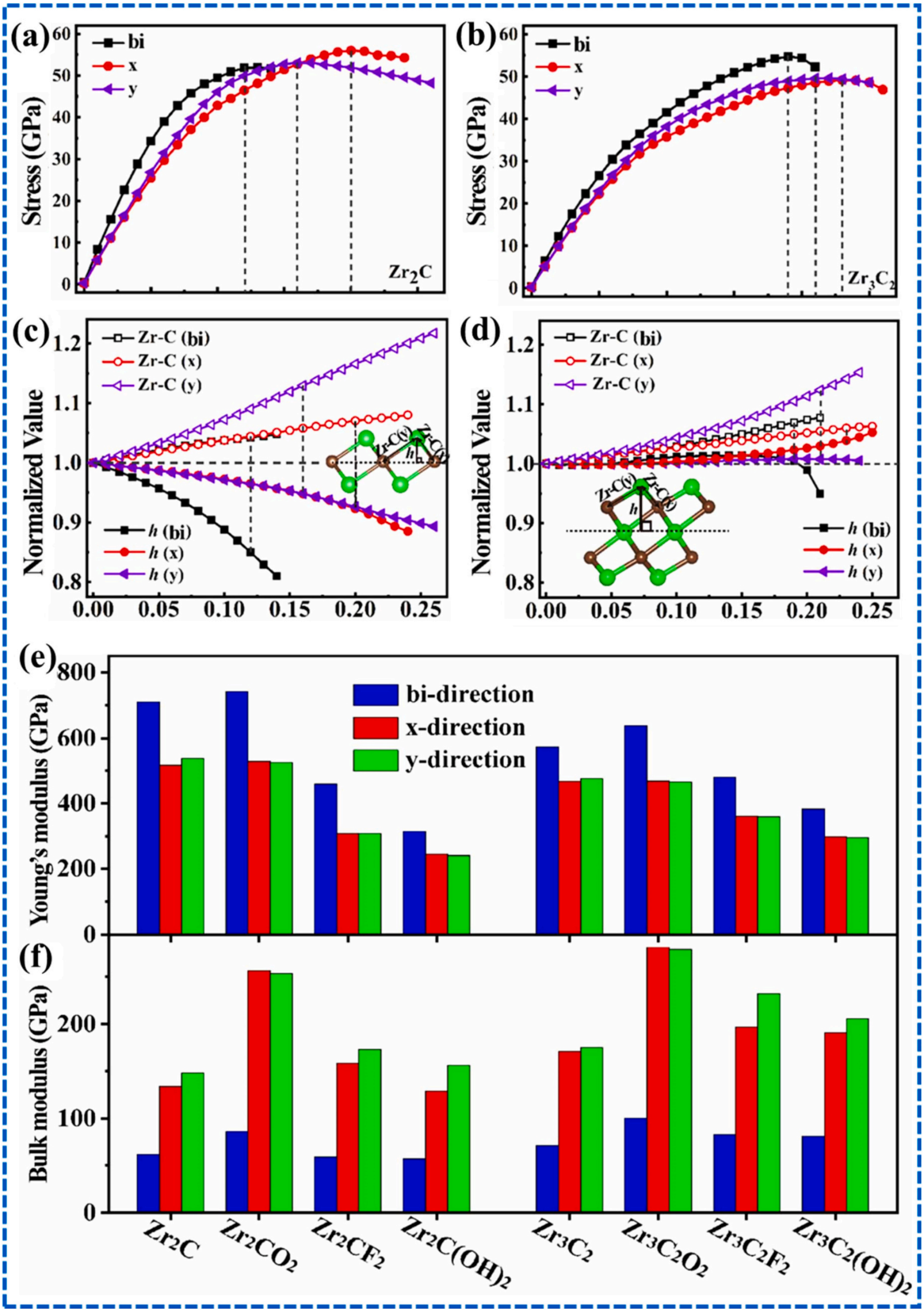

Fig. 10. Tensile stress-strain curves of (a) Zr_2C and (b) Zr_3C_2 under biaxial and uniaxial loading conditions (x/y). The surface Zr–C bond lengths, the out-of-plane half-height h of Zr atoms, vary with strain for (c) Zr_2C and (d) Zr_3C_2. In figure (a) to (d) horizontal axis denotes the tensile strain, whereas the dashed line indicates the emergence of elastic instabilities, also known as 'critical strain point', (e) Young's modulus (E), (f) bulk modulus (Y) of pristine and –O, –F, and –OH functionalized Zr-based MXenes in biaxial and uniaxial orientations. Reproduced with permission from [70].

particles with high Young's moduli is well-documented. The integration of particulates such as SiC, TiB_2, ZrB_2, HfB_2, ZrC, and HfC into Zr-Al(Si)–C carbides is anticipated to strengthen hardness, stiffness, and strength, attributable to the comparatively lower Young's modulus associated with ternary and quaternary carbides. He et al. [63] employed an in-situ reaction/hot pressing technique to fabricate a $Zr_2[Al(Si)]_4C_5$–30 vol % SiC composite, commencing with Zr, Al, Si, and graphite. This composite features a microstructural configuration with SiC grains embedded within a plate-like or elongated $Zr_2[Al(Si)]_4C_5$ matrix. The incorporation of SiC particles distinctly enhances specific stiffness, hardness, fracture toughness, thermal conductivity, and oxidation resistance [63].

The tensile stress–strain behaviour of 2D Zr_2C and Zr_3C_2 under uniaxial and biaxial conditions is depicted in Fig. 10(a) and (b), providing insights into their mechanical response. In the initial stretch phase (strain <3 %), stress increases linearly with strain, characterized by Young's modulus (E) [64]. The calculated moduli, E_x and E_y, for Zr_2C and Zr_3C_2 are 516 GPa (476 GPa) and 538 GPa (467 GPa), respectively, notably higher than values for materials such as 2D MoS_2 ($E_x = 198$ GPa, $E_y = 200$ GPa) [65], 2D $MoSe_2$ ($E_{2D} = 177$ GPa) [66], Graphene oxide ($E_{2D} = 256$ GPa) [67], and $Zr_3Al_3C_5$ ($E_x = 388$ GPa, $E_y = 346$ GPa) [68]. However, they remain lower than 2D Ti_2C ($E_x = 620$ GPa, $E_y = 600$ GPa) [69], indicating that virgin $Zr_{n+1}C_n$ MXenes have superior deformation capabilities compared to Ti_2C MXenes.

The in-plane bulk modulus (Y), for Zr_2C calculated using the third-order bending moment equation, is 134 GPa in the x-direction and 148 GPa in the y-direction, showing slightly higher resistance to compression in the armchair (y) direction than in the zigzag (x) direction. Poisson's ratios ($\nu x = 0.53$, 0.38 and $\nu y = 0.15$, 0.10 for Zr_2C, and Zr_3C_2, respectively) reveal that deformation is less pronounced in the zigzag than in the armchair direction [70]. To further understand structural failure under tensile stress, Fig. 10(c) and (d) illustrate changes in structural properties with strain, including half-thickness (h) and average Zr–C bond length. These data show that Zr–C bonds in Zr_2C and Zr_3C_2 elongate more along the y-axis under stress, leading to a lower critical strain along the y-axis than the x-axis. Notably, the half-thickness of Zr_3C_2 increases slightly with strain in all loading conditions, suggesting potential for shock-resistance applications in devices utilizing pristine Zr_3C_2 MXenes. Structural changes under tension suggest that Zr_3C_2 failure primarily arises from the elongation and rupture of internal Zr–C bonds, enhancing flexibility during stretching.

The influence of –O, –F, and –OH functional groups on the flexibility of 2D $Zr_{n+1}C_n$ ($n = 1, 2$) MXenes was evaluated by calculating E and Y from stress–strain data, as shown in Fig. 10(e) and (f). The mechanical anisotropy of $Zr_{n+1}C_n$-based MXenes is minimal, similar to $Ti_{n+1}C_n$ based MXenes [71]. Functionalization with –F and –OH has a greater impact on E than –O, though –O functionalization has a stronger effect on Y. Compared to Zr_2CT_2, $Zr_3C_2T_2$ MXenes generally exhibit superior deformation resistance, except for $Zr_3C_2O_2$. However, Zr_2CT_2 MXenes are more suitable for flexible and wearable sensor applications than $Zr_3C_2T_2$ due to their better flexibility.

2.5.4. *Electrical properties*

The electrical properties of Zr-based MXene materials, such as Zr_2AC, are primarily governed by their electronic band structure, particularly the band gap between energy levels. Studies indicate that multiple valence bands in Zr_2AC intersect the Fermi level and overlap with conduction bands, facilitating its conductive properties [72]. Density of states (DOS) calculations further validate the structural stability and favourable electrical conductivity of Zr_2AC phases. The Zr 4d orbitals significantly contribute to DOS peaks, while interactions between the A 3p and Zr 4d states just below the Fermi level, along with the hybridization of C 2s and C 2p with Zr 4d states, play a crucial role in stabilizing the Zr_2AC structure. This material exhibits a mix of covalent, metallic, and ionic bonds due to the distinct electronegativities of its constituent elements [73].

Ceramics with ternary and quaternary compositions, such as Zr–Al–Si–C, demonstrate notable electrical conductivity, making them suitable for machining via electrical discharge processes. The reported electrical conductivities at room temperature for ternary compounds $Zr_2Al_3C_4$, $Zr_3Al_3C_5$, and the quaternary compounds $Zr_2[Al(Si)]_4C_5$, $Zr_3[Al(Si)]_4C_6$ are 0.91×10^6, 0.69×10^6, 0.74×10^6, and 1.16×10^6 S m^{-1}, respectively. For comparison, the Hf-Al-C composite exhibits a conductivity of 0.78×10^6 S m^{-1}.

First-principles calculations indicate that the electronic states primarily responsible for electrical conductivity originate from the Zr 4d states or Hf 5d states at the Fermi level [74]. Zr MXenes are generally expected to behave as conductors, with the exception of Zr_2CO_2 MXene [75,76]. DFT is widely used for ab initio calculations and is reliable for predicting electronic properties but can sometimes misclassify materials, such as mistakenly labelling some semiconductors as gapless due to the limitations of specific density functionals, particularly in complex transition-metal systems [77].

2.5.5. *Electrochemical properties*

Recent studies have demonstrated the promising potential of various MXenes for energy storage and conversion applications [78]. A crucial factor influencing electrode performance is the kinetics of electron and ion transport within the material [79]. For instance, investigations into ZrC MXenes using DOS calculations, with and without Na atom adsorption, reveal that Na desorption does not significantly alter the electronic structure of pristine ZrC. While, Zr_2C_2 exhibits a minor shift in the Fermi level upon Na adsorption, Zr_3C, Zr_3C_2, and $Zr_3C_2O_2$ maintain consistent Fermi levels. Notably, Zr_3CO_2 shows metallic characteristics after Na adsorption, which may enhance Na–ion adsorption and desorption, thereby enabling high-rate capability and capacity in Na-ion batteries using Zr–based MXene electrodes.

Further analyses of Zr_2CNa_2, $Zr_3C_2Na_2$, $Zr_3CO_2Na_2$, and $Zr_3C_2O_2Na_2$ MXenes using charge density calculations indicate that $Zr_3CO_2Na_2$ and $Zr_3C_2O_2Na_2$ have higher electron acceptance compared to Zr_2CNa_2 and $Zr_3C_2Na_2$. To better understand their electrochemical properties, researchers examined Na diffusion paths and barriers using the Climbing Image-Nudged Elastic Band (CI–NEB) method. Diffusion barriers were reported as follows: Zr_3C (0.3 eV) $\approx$ Zr_3C_2 (0.03 eV) < Zr_2CO_2 (0.29 eV) < $Zr_3C_2O_2$ (0.32 eV). Importantly, Zr_2CO_2 and $Zr_2C_2O_2$ display diffusion barriers similar to those for Li adsorption, suggesting that these MXenes facilitate easy Na migration, which is beneficial for high-rate applications in Na–ion batteries [80].

Li et al. [81] systematically used DFT calculations to study Ti–Zr dual transition metal carbides ($TiZrCO_2$, $Ti_2ZrC_2O_2$, and $TiZr_2C_2O_2$) as anode materials for Na-ion batteries. These systems exhibited dynamic stability, commendable conductivity, and support for energetically favourable double-layer Na adsorption on both sides of the material, leading to higher capacities than mono–Ti or mono–Zr MXenes. Additionally, their low diffusion energy barriers (<0.3 eV) and favourable open-circuit voltages indicate high viability as Na–ion battery anodes. The Zr MXenes, particularly Zr_2CO_2 and $Zr_3C_2O_2$, enable stable double-layer Na adsorption due to minimal lattice mismatch with the Na bilayer [53]. However, $Zr_3C_2O_2$ has an anode capacity of 326 mAh g^{-1} for Na–ion batteries, slightly lower than the theoretical 372 mAh g^{-1} due to the greater atomic weight of Zr atoms. Mono–Ti-based MXenes, though lighter, offer limited Na storage, while Zr–based MXenes provide improved storage capacity [81].

Furthermore, $TiZrCO_2$, $Ti_2ZrC_2O_2$, and $TiZr_2C_2O_2$ exhibit average open-circuit voltages conducive to high energy density and reduced Na cluster formation, with predicted capacities of 586, 441, and 375 mAh g^{-1}, respectively, surpassing those of mono-metal carbides. The hierarchical structure of these Ti–Zr dual transition metal carbides positions them as superior anode materials for Na–ion batteries compared to their mono-transition metal counterparts [81].

2.5.6. *Thermo–electric properties*

The functional groups and orientations of MXenes significantly

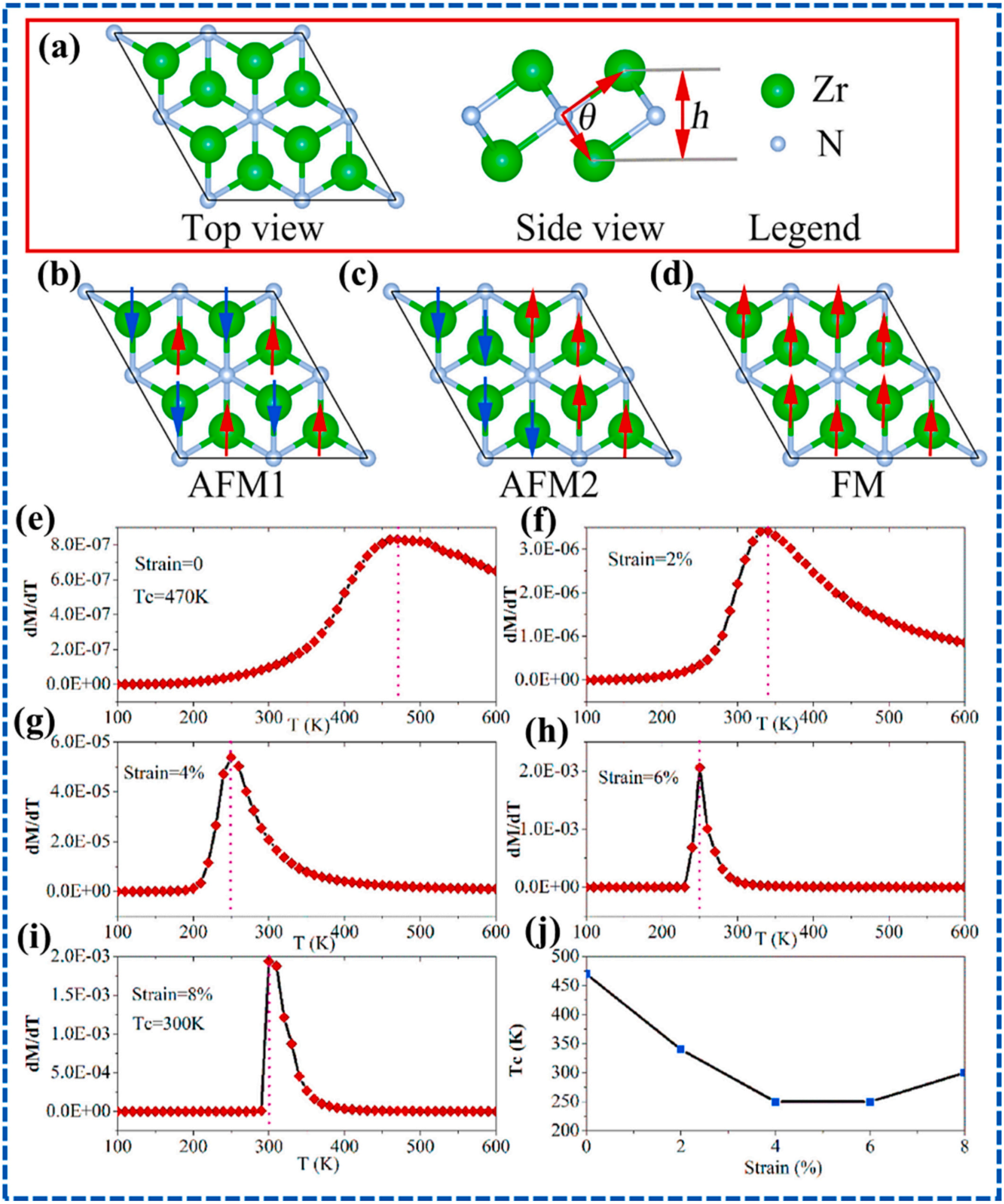

Fig. 11. (a) Top and side views of the geometric arrangements of Zr_2N MXene, along with three possible magnetic states: (b) AFM1, (c) AFM2, (d) FM configurations, and the magnetic susceptibility as a function of temperature at tensile strains of (e) 0 %, (f) 2 %, (g) 4 %, (h) 6 %, (i) 8 %, (j) Effect of critical temperatures (T_c) on the strain. Reproduced with permission from [86].

Table 2
Summary of typical Zr-based MXenes.

Materials	Synthesis routes	Morphology	Properties	Applications	Ref.
Ti_3C_2–MXene embedded Zr-crosslinked Na alginate	In-situ etching	Aerogel beads	The embedded MXene improved the physical properties and worked as chemisorption active points to further strengthen phosphate adsorption of the SA beads simultaneously	Phosphate adsorption	[89]
Zr metal–organic framework	Hydrothermal technique	Homogeneous heterostructure crystals	Excellent mechanical properties	Triboelectric nanogenerators	[59]
ZrC	Magnetron sputtering deposition technology	Nano films	Nonlinear optical properties	Optical modulator designed for very brief laser pulses ZrC films produced using magnetron sputtering deposition exhibited excellent smoothness and uniformity	[90]
2D ZrC nanosheet (NSs)	Probe sonication and bath sonication	Ultrathin nanosheet	Physiological conditions because of its rich biological activities as well as low toxicity	Anticancer drug delivery platform	[91]
2D Zr ferrocene-based MOF/AuNPs/4-mercaptophenylboronic acid	Ultrasonication	Layered morphology.	Large surface area of Zr–Fc MOF	Faraday Cage-Type Electrochemical Aptasensor for *Escherichia coli* Detection	[92]
Zr amino–tris–(methylenephosphonate) (Zr–AMP)	In situ facilely loading Zr amino–tris–(methylenephosphonate) (Zr–AMP) onto the Ti carbide (MXene) surface	Nanosheets	With 1 wt.% of Zr-MXene, the resultant TPU nanocomposites demonstrate a record break strain (2060 %) and toughness (316 MJ m^{-3}) to date, in addition to increased tensile strength by 43.4 % and improved fatigue resistance relative to the TPU matrix, because of favourable interfacial hydrogen-bonding	Fire retardant	[93]
ZrO_2/CuO–ZnO nanocomposites	Heat treatment	Nanoparticles	Biomedicinal properties	Antibacterial, antifungal and antidiabetic activities	[94]
Zr_2N MXene	–	–	The effects of strain on the magnetic properties of Zr_2N MXene proved dynamically and mechanically stable by the first-principles calculations	Spintronic applications	[86]
$Zr_3N_2O_2$ MXene monolayer	–	–	Thermoelectric properties using first principles and Boltzmann transport theory	Thermoelectric applications	[95]
Zr_nC_{n-1} ($n = 2$, 3, and 4) and their functionalized MXene	–	–	Structural, vibrational, and electronic properties using the framework of density functional theory calculations	–	[96]
Zr_2CO_2 MXene	–	–	The electronic and optical properties, quantum capacitance and photocatalytic performance of Zr_2CO_2 under uniaxial strain are investigated by DFT	Tensile strain often improves the efficacy of Zr_2CO_2 as a cathode material, but compressive strain induces a transition from cathode to anode material. Zr_2CO_2 with a strain over 7 % demonstrates exceptional CO_2 photocatalytic activity.	[97]
Zr_2CO_2 MXene	–	–	The electronic, optical, and photocatalytic properties of Zr_2CO_2 MXene under biaxial strain are investigated by hybrid HSE06 functional	Photocatalytic water splitting in acid environment, hydrogen evolution reaction and oxygen evolution reaction.	[98]
Zr_2Si MXene	–	–	Antiferromagnetic property through first-principles calculations	Electronics applications	[55]
$Zr_3C_2O_2$ MXene	–	–	First-Principles computations were employed to examine the adsorption behaviours of several gas molecules on monolayer $Zr_3C_2O_2$ MXene	NH_3 sensor	[99]
Zr_2CO_2 MXene	–	–	Thermodynamic stability and N_2 adsorption behaviour is studied through DFT	Catalyst for nitrogen reduction reaction	[100]

influence their electrical behaviour, determining whether they exhibit semiconducting or metallic characteristics [82]. Gandi et al. [83] studied various MXenes, including Zr_2CO_2 and reported they possess narrow band gaps between 0.17 and 0.44 eV, classifying them as semiconductors. These narrow band gap semiconductors generally exhibit high electrical conductivity, attributed to minority carrier contributions, which can reduce the Seebeck effect at low carrier concentrations and elevated temperatures. Consequently, Zr_2CO_2 shows promise for thermoelectric applications due to these properties.

Zr_2CO_2 shares many attributes with Ti_2CO_2 as both Zr and Ti possess

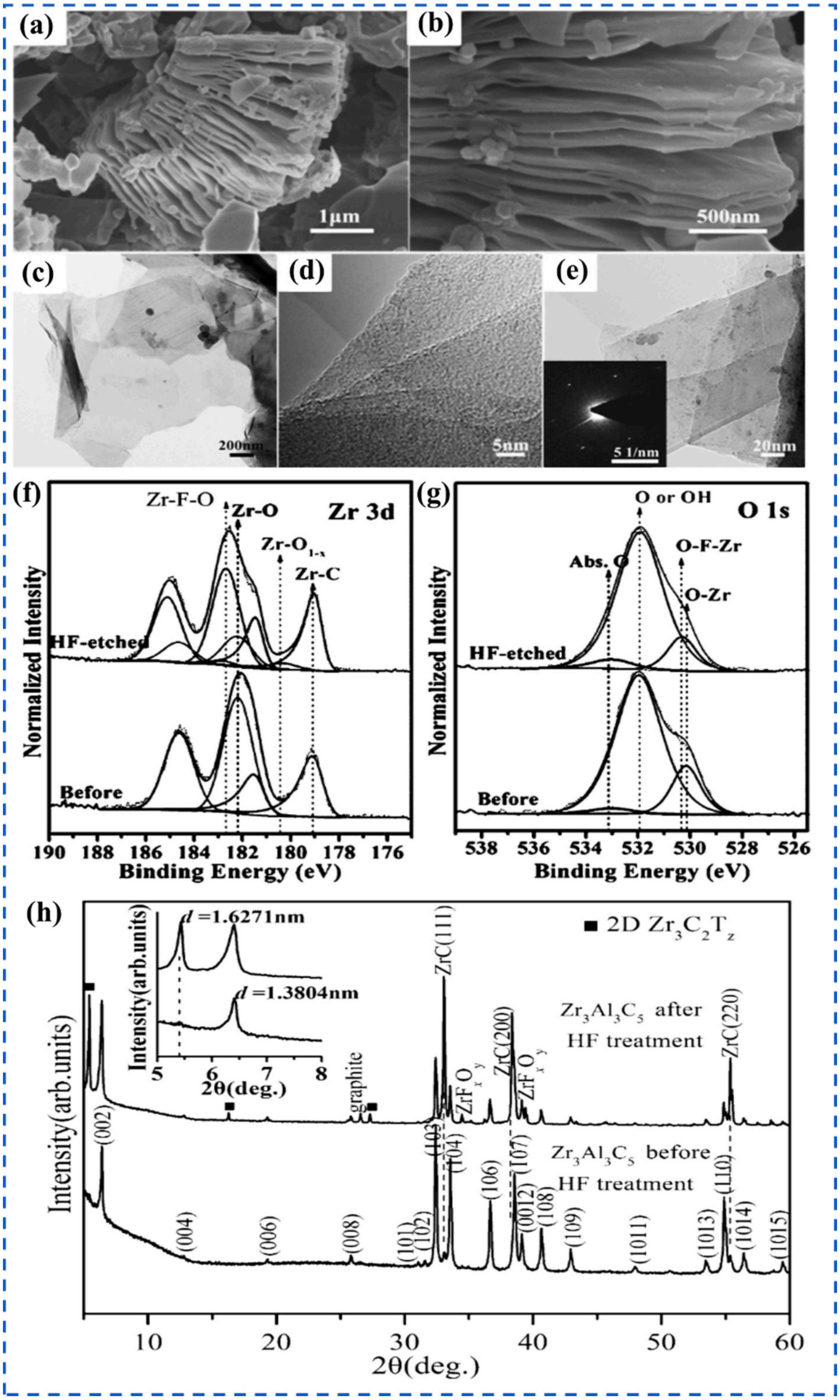

Fig. 12. SEM images of $Zr_3Al_3C_5$ after HF treatment reveals; (a) Exfoliated grains, (b) Accordion like structure, (c) Bright field TEM images of the 2D $Zr_3C_2T_z$ material after ultrasonication, (d) TEM image of few–layered $Zr_3C_2T_z$, (e) TEM image of a scrolled $Zr_3C_2T_z$ nanosheet, inset is a SAED pattern showing the reserved hexagonal basal plane symmetry. High-resolution XPS spectra of samples before and after etching procedure in the; (f) Zr 3d region and (g) O 1s region. (h) XRD of $Zr_3Al_3C_5$ before and after HF treatment. Reproduced with permission from [102].

12 valence electrons, leading to structural and compositional parallels. Notably, Ti_2CO_2 has been shown to achieve a higher level of n–type doping than Zr_2CO_2, combined with a lower lattice thermal conductivity, enhancing its thermoelectric figure of merit relative to Zr_2CO_2 [83].

The coefficient of thermal expansion (CTE) is also critical in thermoelectric materials. It is often linked to adhesive strength, as materials with mismatched CTEs can experience stress and potential failure at the interfaces. This is particularly important in layered compounds and composites used in thermoelectric applications, where maintaining structural integrity under thermal cycling is essential [84]. The CTE for

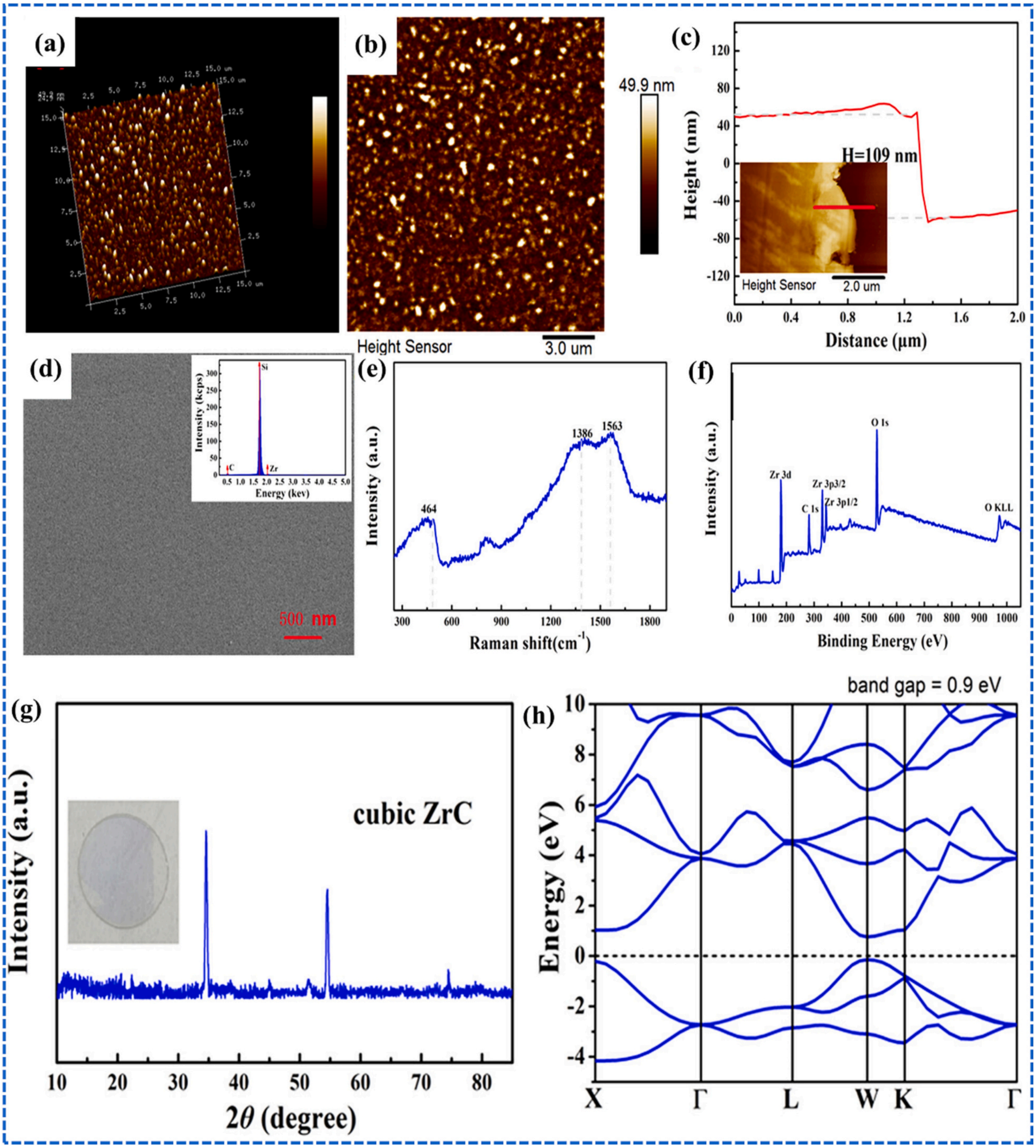

Fig. 13. Characterization of MXene ZrC film SAOM: (a) AFM 3D topographical images, (b) Corresponding 2D topographical images, (c) Thickness profiles, (d) SEM and EDS image, (e) Raman spectra, (f) XPS survey scan of MXene ZrC films, (g) XRD patterns, (h) Calculated band structure of ZrC. Reproduced with permission from [90].

$Zr_2Al_3C_4$ and $Zr_2[Al(Si)]_4C_5$ are determined to be $8.1 \times 10^{-6}\ K^{-1}$, while $Zr_3Al_3C_5$, and $Zr_3[Al(Si)]_4C_6$ have CTE values of $7.7 \times 10^{-6}\ K^{-1}$. Comparatively, Al_4C_3 has lower stiffness than ZrC, suggesting a weaker bond strength between Al and C relative to Zr and C. Consequently, Zr-Al (Si)-C compounds have a lower average bond strength than binary ZrC, resulting in an increase in CTE for layered ternary and quaternary carbides. Notably, the CTE of these carbides depends on the thickness of the ZrC layers, with an increase in ZrC layer thickness potentially lowering the CTE. Thus, $Zr_4Al_3C_6$ is anticipated to have a lower CTE than $Zr_3Al_3C_5$ [85].

2.5.7. Magnetic properties

Yue and colleagues investigate the magnetic properties of Zr_2N MXene using first-principles calculations, focusing on its strain-free and stress-induced magnetic behaviours [86]. In its natural state, Zr_2N exhibits inherent antiferromagnetic (AFM) behaviour with a high Néel temperature of 470 K, placing it in the MXene family of AFM materials. However, when subjected to tensile biaxial strain, the magnetic ordering shifts toward ferromagnetism, with a critical threshold for this transition occurring at around 4 % strain. Notably, the critical temperature (T_c) for the AFM state decreases to approximately 250 K under this strain, but as strain increases beyond 4 %, the magnetic ordering of the material transitions to ferromagnetic (FM), with T_c rising back toward ambient temperatures, reaching around 300 K at 8 % strain [23].

Moreover, the magnetic anisotropy energy (MAE) for strain-free Zr_2N MXene is −92 μeV per cell, indicating a stable magnetic ordering at temperatures above 0 K [87,88]. Even under stress, Zr_2N retains significant magnetic anisotropy, allowing for controlled MAE manipulation through strain adjustments, with peak MAE observed at a 2 % strain. This pronounced perpendicular MAE is attributed to spin-orbit coupling interactions, specifically between the P_x/P_y states of Zr atoms at the microscopic level. This study contributed valuable insights into previously undiscovered magnetic properties of MXene materials, expanding the potential applications of Zr_2N in spintronics [86].

The geometric configuration of Zr_2N, depicted in Fig. 11(a), shows a N layer sandwiched between two Zr atomic layers. The spin-polarized state of Zr_2N exhibits a 70 meV lower energy per formula unit than the non-polarized state. To ascertain the most stable magnetic configuration, the study evaluates three potential states: FM and two AFM variants (AFM1 and AFM2), as depicted in Fig. 11(b–d). The AFM1 state demonstrates ferromagnetic interactions within layers while exhibiting antiferromagnetic interactions between layers. By using the total energy of the AFM1 state as a reference point, the relative energies of AFM2 and FM states are determined to be 267 meV and 103 meV higher, respectively. These results establish Zr_2N as an AFM1-type antiferromagnet with a local magnetic moment of 0.73 μB per Zr atom.

Magnetic susceptibility curves in Fig. 11(e–j) show temperature-dependent behaviour, with peaks indicating T_c. For strain-free Zr_2N, the Néel temperature around 470 K confirms the stability of the AFM1 ordering up to room temperature. However, as strain is applied, T_c decreases to 250 K at 4 % strain in the AFM state, while favouring ferromagnetic ordering results in an increased T_c. At 8 % strain, the ferromagnetic T_c reaches 300 K, suggesting that higher strain levels can stabilize ferromagnetism near room temperature. This strain-responsive tunability opens opportunities for Zr_2N MXene in applications where magnetic properties are essential and require adaptability to environmental or operational stresses [86].

Table 2 provides a summary of synthesis methods, properties, morphology, and applications for various Zr–based MXenes and their related heterostructures.

3. Characterizations of Zr-based MXenes

This section discusses key characterizations of Zr-based MXenes, focusing on structural, morphological, and compositional aspects. Fig. 12(a) and (b) illustrate SEM images of $Zr_3Al_3C_5$ after HF treatment, revealing individual grain exfoliation within the basal planes and accordion-like structures similar to those observed in Ti_3AlC_2 [101]. TEM images in Fig. 12(c–e) reveal that HF–etched and sonicated $Zr_3Al_3C_5$ samples exhibit thin, electron-transparent layers, suggesting a few–layer MXene morphology. EDS analysis confirms the presence of Zr, C, and O in the nanosheets, with no trace of Al. These sheets display flexible, foldable characteristics, similar to typical 2D MXenes and graphene. XPS spectra in Fig. 12(f) and (g) identify Zr–C and Zr–O bonds in $Zr_3Al_3C_5$, both pre- and post–HF treatment, aligning with previous findings for ZrC [102,103].

The XRD pattern in Fig. 12(h) shows that the HF-treated $Zr_3Al_3C_5$ powders primarily consist of a single phase with minor ZrC impurities. Notably, the (002) peak shifts to a lower angle of $2\theta = 5.438^\circ$, corresponding to an increase in the c lattice parameter from 27.73 Å to 32.53 Å, a feature commonly observed in HF–etched MXenes [101,104]. Two additional peaks at $2\theta = 16.328^\circ$ and $2\theta = 27.248^\circ$ are sharper and more intense compared to the typically broad peaks of etched MXenes, suggesting possible intercalation during the etching process [105,106]. This intercalation likely contributes to the observed expansion of the c lattice parameter. The initial $Zr_3Al_3C_5$ powders contain minor ZrC impurities, which persist after HF treatment due to the chemical inertness of rock-salt structured ZrC to HF. These impurities appear more prominent post–etching, likely due to the reduction of the $Zr_3Al_3C_5$ parent phase and the formation of a less ordered structure [102].

In a study by Zhou et al. [85] $Zr_3Al_3C_5$ was selectively etched to create a novel Zr–based 2D carbide MXene, exploiting the weak bonding and hydrolytic susceptibility of Al–C layers. This material, part of the quaternary transition-metal carbides, can be generalized as $MnAl_3C_4$ and $Mn[Al(Si)]_4C_3$, where M is Zr or Hf, and n ranges from 1 to 3. These carbides are structurally complex, with an intergrowth framework of hexagonal metal carbide layers and AlC_3–like $Al_3C_2/[Al(Si)]_4C_3$ layers sharing a C monolayer at their interface [85,102].

Wang et al. [90] investigated the deposition of ZrC films on saturable absorber optical modulators (SAOM) based on MXene onto fused silica substrates using magnetron sputtering. The characterization of these films yielded insights into the synthesis process, with critical parameters for assessing film quality, including thickness and surface roughness, effectively measured by atomic force microscopy. Fig. 13(a) and (b) depict 3D and 2D atomic force microscopy topographic images of the MXene ZrC films, revealing a smooth and uniform surface morphology with a low root mean square roughness (Rq) value of 7.21 nm, which is advantageous for minimizing defects. The film thickness was approximately 109 nm, as determined by atomic force microscopy profile measurements (Fig. 13(c)). Moreover, the SEM–EDS analysis of MXene ZrC films corroborates the presence of C and Zr, as confirmed by EDS spectra (Fig. 13(d)). The Raman spectrum (Fig. 13(e)), acquired using a 532 nm excitation laser, reveals three distinct peaks at wavenumbers at 464, 1386, and 1563 cm^{-1}. Notably, the peaks within the 1300–1400 cm^{-1} and 1550–1600 cm^{-1} ranges correspond to the D and G bands of carbon, while the peak at 464 cm^{-1} signifies ZrC. XPS analysis of MXene ZrC films indicates the presence of Zr, C, and O, with a survey spectrum and specific elemental spectra (Zr 3d, C1 s, Zr $3p_{3/2}$, Zr $3p_{1/2}$, and O1 s) depicted in Fig. 13(f). The XPS data suggest minimal surface contamination and defects, with only a few additional peaks detected. Moreover, the XRD patterns in Fig. 13(g) illustrate the FCC lattice structure, indicating the excellent crystallinity of ZrC. The band structure of ZrC was further explored through first-principles calculations, as illustrated in Fig. 13(h) [90].

4. Applications of Zr-based MXenes

The 2D laminar material α–Zr phosphate ($Zr(HPO_4)_2{\cdot}H_2O$), commonly referred to as α–ZrP, is characterized by Zr atoms positioned alternately above and below the central α–ZrP plane. This material shows promise in applications such as ion exchange processes [107], lubricants [108], and host intercalation [109,110]. When integrated into Ni–W composites, α–ZrP contributes to a nanocomposite matrix with notable friction resistance and suitable impedance properties [110–112]. Additionally, studies on the compatibility of organic coatings with exfoliated α–ZrP (e–ZrP) indicate that using polypyrene as an encapsulant enhances compatibility with aqueous epoxy systems, leading to improved anti-corrosion performance of the composite coatings [113].

The exfoliation of α–ZrP was initially achieved using tris-(hydroxymethyl)-aminomethane (Tris), followed by functionalization via a one-pot approach [111,114]. The resulting composite coating, incorporating functionalized e–ZrP, showed superior anti-corrosion properties attributed to the barrier effect created by the coating. Limited studies have explored 2D heterojunctions involving MXene and e-ZrP, but existing findings suggest that MXene/e–ZrP heterojunctions could mitigate MXene's inherent tendency to restack [115]. Moreover, the intrinsic lattice mismatch between MXene and e-ZrP may further enhance their lubricating properties [116]. MXenes, known for their exceptional qualities, are utilized in diverse advanced applications, including catalysis, biosensing, energy storage, solar cells, and photonics [117]. Specific applications are discussed in the later sections.

Meanwhile, the Zr MAX phases exhibit unique attributes that make them suitable for specialized applications. For instance, Chen et al. [29]

successfully synthesized a ternary MAX phase, Zr_2SeC, incorporating chalcogen atoms. A comprehensive crystal structure analysis confirmed the presence of Se atoms at the A site within the MAX phase lattice. First–principles calculations were employed to determine the optimal crystal structure of Zr_2SeC and to explore its chemical bonding characteristics relative to the Zr_2SC analogue. The findings reveal that the heat transfer coefficient of Zr_2SeC is significantly influenced by electron participation, particularly at elevated temperatures, which counteracts the decline in thermal conductivity. These insights highlight the crucial role of A–site elements in modulating the physical properties of MAX phases [29].

4.1. Optoelectronic devices

DFT calculations and the application of compressive and tensile strain (CTS) at 2 %, 4 %, and 6 % indicate that the Zr_2CO_2 monolayer exhibits promising characteristics for optoelectronic and nanodevice applications [118]. A study by Alireza et al. [118] investigated the optical properties of 2D Zr_2CO_2, revealing enhanced absorption across the infrared, ultraviolet, and visible regions compared to other 2D materials like Hf_2CO_2 and Ti_2CO_2, highlighting its superior light-harvesting capabilities. In terms of vibrational properties, Zr_2CO_2 shows a higher phonon frequency (680 cm^{-1}) than MoS_2 (473 cm^{-1}), which could improve stability and performance in high-frequency applications [119]. Notably, the Zr_2CO_2 monolayer has an initial indirect band gap of 1.34 eV, which shifts to a direct band gap under 8% tensile strain, broadening its utilization in optoelectronic engineering where band gap tunability is advantageous. In addition, computational studies on the electronic density distribution, band structure, and semiconducting nature of Zr_2CO_2 confirm its potential as a promising MXene material for optoelectronic applications. When compared to materials like hexagonal boron nitride (h–BN) and aluminum nitride (AlN), Zr_2CO_2 demonstrates superior optical absorption in the visible range, positioning it as a highly competitive candidate for optoelectronic applications [120,121].

4.2. Photonic devices

In recent years, photonic devices have achieved significant advancements, finding applications in diverse fields, including optical communications, micromachining, remote sensing, biological applications, and scientific research [122]. Among these devices, ZrC MXenes have shown potential due to their remarkable nonlinear optical properties, though their use in ultrafast photonics remains limited. Liu et al. [37] first demonstrated the nonlinear optical behaviour of ZrC films prepared via magnetron sputtering deposition (MSD) technology in 2021, achieving a saturation intensity of 197.6 MW cm^{-2} and a modulation depth of 11.9 %. These properties suggest ZrC as a promising mode-locking material for generating ultrashort pulses in fiber lasers and other photonic systems. High-yield, high-quality ZrC saturable absorbers, sputtered onto D-shaped fiber via the MSD method, exhibited a smooth, dense surface with a saturation intensity of 197.6 MW cm^{-2} and a modulation depth of 11.9 %, generating output power up to 49.86 mW. This positions ZrC as a highly suitable material for ultrafast photonic applications.

In another significant advancement, Liang et al. [123] applied liquid-phase exfoliation to produce ZrC–based saturable absorbers, which enabled the first successful Q-switching of a 3 μm band laser. Their computational studies, grounded in fundamental principles, confirmed that metallic ZrC could serve as an exceptional optical modulator for mid-infrared lasers. ZrC nanofilms and nanoclusters were efficiently synthesized by sonication of commercially available ZrC powder, with the resulting ZrC saturable absorber used to achieve a peak power of approximately 24 W within a passively Q-switched Er: Lu_2O_3 laser system, pumped at 10.9 W. Utilizing ZrC nanoparticle-based absorbers produced remarkably short pulses, with durations of 50 ns at a 13 kHz repetition rate, pulse energy of 22 μJ, and peak power reaching 0.4 kW. These results represent the shortest pulse durations and highest peak powers achieved with any Q-switched laser operating in the 3 μm wavelength range, affirming ZrC's viability as a saturable absorber for achieving minimal pulse durations in the mid-infrared spectral region.

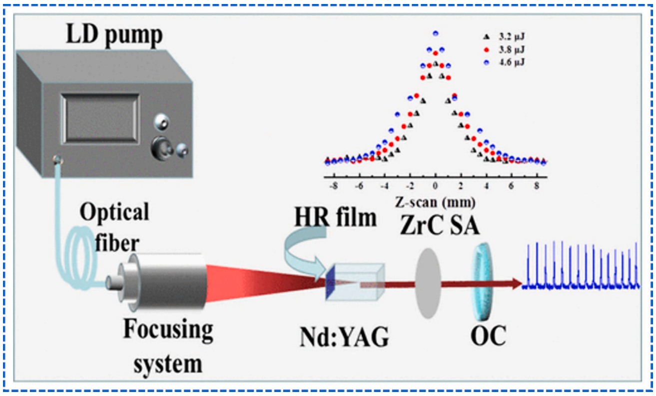

Fig. 14. Schematic diagramof the linear cavity configuration of the Nd:YAG laser. Reproduced with permission from [90].

In a related study, Wang et al. [90] employed a commercially available quasi-continuous wave diode laser (LD) at 808 nm to explore the thermal dynamics and output stability of ZrC–based saturable absorbers, as shown in Fig. 14. Unlike pulsed lasers, continuous-wave laser operation introduces additional heat, potentially impacting the saturable absorber's performance and structural integrity. To mitigate thermal effects, a pulsed diode laser with a pulse duration of 25 microseconds and a repetition rate of 1 kHz was utilized. An Nd:YAG crystal with a 1.2 at.% Nd^{3+} concentration was used as the gain medium, with dimensions of 3 mm × 3 mm × 5 mm optimized for efficient energy absorption at the 808 nm pump wavelength. Coatings with high transmission at 808 nm and high reflection at 1064 nm were applied to one end of the crystal, allowing for shorter pulse generation within the laser oscillator, which was designed with a compact length of 22 mm. Furthermore, the Nd:YAG crystal was temperature-controlled at 20 °C using a copper mount with water cooling, ensuring stable, consistent laser output [90]. These studies collectively highlight the potential of ZrC as a high-performance material for photonic devices, particularly in applications requiring rapid response times and high power in the mid-infrared spectrum. The innovations in ZrC–based saturable absorbers and the detailed exploration of thermal management in ZrC-integrated laser systems open new avenues for the development of efficient and reliable ultrafast photonic devices.

4.3. Metal–ion batteries

Lithium-ion (Li–ion) batteries continue to advance rapidly within the field of metal-ion battery technology, recognized for their high energy density and excellent cycling stability. Recent studies have highlighted the role of Zr in enhancing Li–ion battery performance. Zhu et al. [54] investigated the effects of Zr on Li-ion batteries by employing DFT to assess the structural and energy storage properties of Zr_2C and Zr_2CX_2 compounds, where X represents −F, −O, or S. Their results indicated that Zr_2C and Zr_2CS_2 exhibit remarkable specific capacities of 310 mAh g^{-1} and 259 mAh g^{-1}, respectively, along with low diffusion barriers, highlighting their potential for high-performance energy storage [124,125]. Additionally, Zr_2CS_2 exhibited metallic properties post-synthesis, which are crucial for battery applications [54].

A critical factor for improving capacity in MXene-based anodes for Li–ion batteries is the efficient adsorption of Li–ions. By considering the adsorption of Li-ions on both sides of MXene sheets, it is possible to increase the capacity, as Li–ions can arrange themselves in multiple layers. Computational analyses demonstrated that the compound $Zr_2CO_2Li_x$ with three Li atoms adsorbed on each side of the MXene sheets

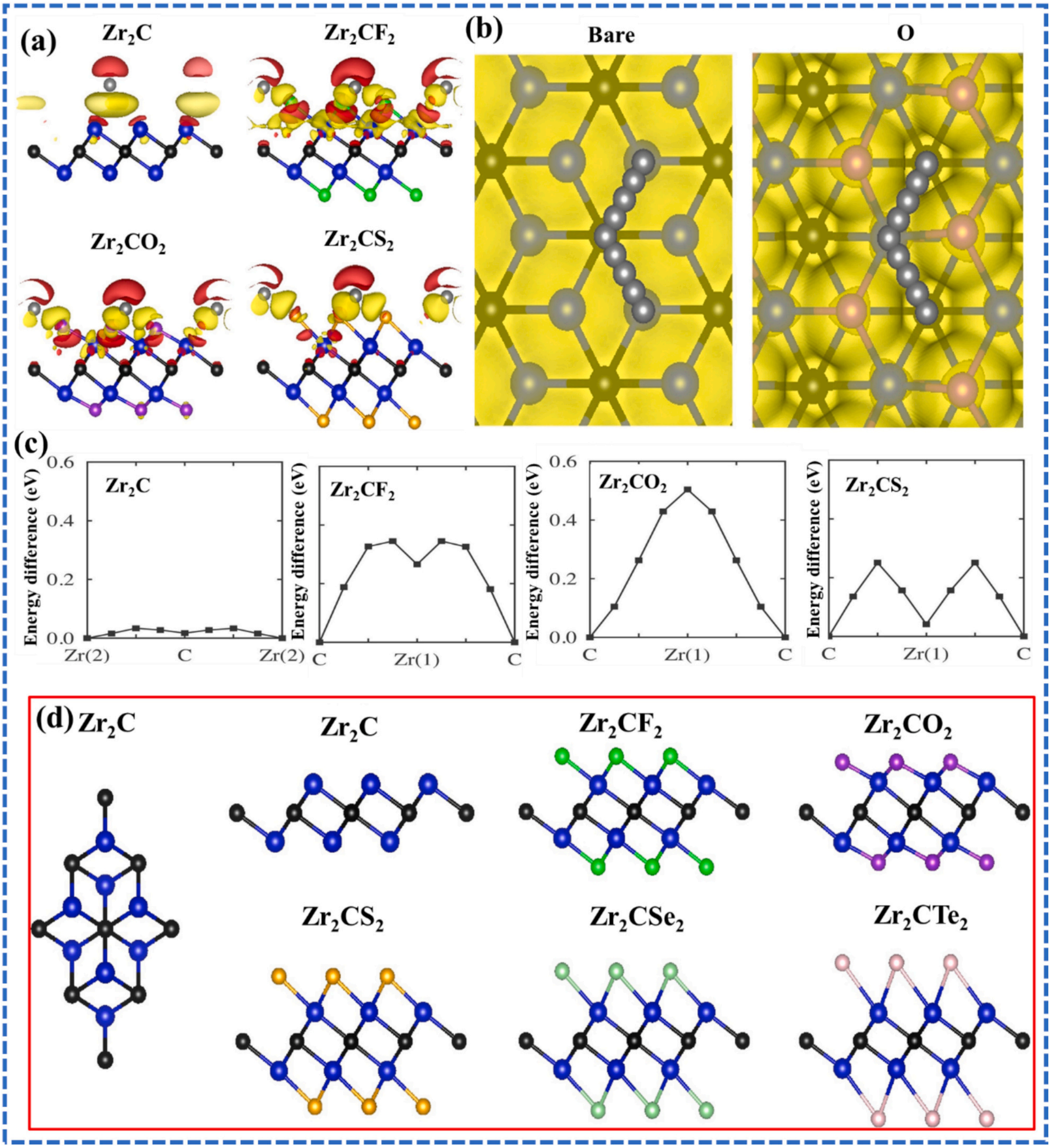

Fig. 15. (a) Charge redistribution due to the interaction with Li. Yellow/red is indicative of the accumulation or depletion of charge. The isosurfaces correspond to an isovalue of 2×10^{-3} electrons/bohr^3. The atoms of Zr, C, Li, F, O, and S atoms are shown in blue, black, grey, green, purple, and brown colour, (b) Diffusion paths for Li atoms. The Zr, C, Li, and F/O/S atoms are shown in blue, black, grey, and purple colour. The surface charge distribution is shown in yellow for the O case. For the F and S cases the distribution is virtually the same, (c) Diffusion barriers encountered by Li atoms on Zr_2C and Zr_2CX_2 (X = F, O, and S), (d) Structures of Zr_2C and Zr_2CX_2 (X = F, O, S, Se, and Te). The top view of Zr_2C is shown on the left, while the side views of Zr_2CX_2 are shown for each respective X element. The atoms of Zr, C, F, O, S, Se, and Te are represented by the colours blue, black, green, purple, brown, cyan, and pink. Reproduced with permission from [54]. (For interpretation of the references to colour in this figure legend, the reader is referred to the web version of this article.)

offered favourable voltages [54]. Further studies have shown that incorporating Zr into the system to form heterostructures can enhance the performance of Li–ion batteries [126]. Insights into material stability can be obtained from the charge density differences depicted in Fig. 15 (a), which are quantitatively described using Eq. (7).

$$\Delta\rho = \rho - \rho_{MXene} - \rho_{Li} \tag{7}$$

Where ρ represents the total charge density of the system, while ρ_{MXene} and ρ_{Li} denote the charge densities of the MXene material without Li and the individual Li atoms, respectively. Observations indicate significant charge redistribution onto Li in bare MXene compared to passivated MXenes, reflecting variations in their interaction profiles.

The charging rate is dependent upon the diffusion characteristics of Li. Three diffusion paths are examined, with the ground state location of

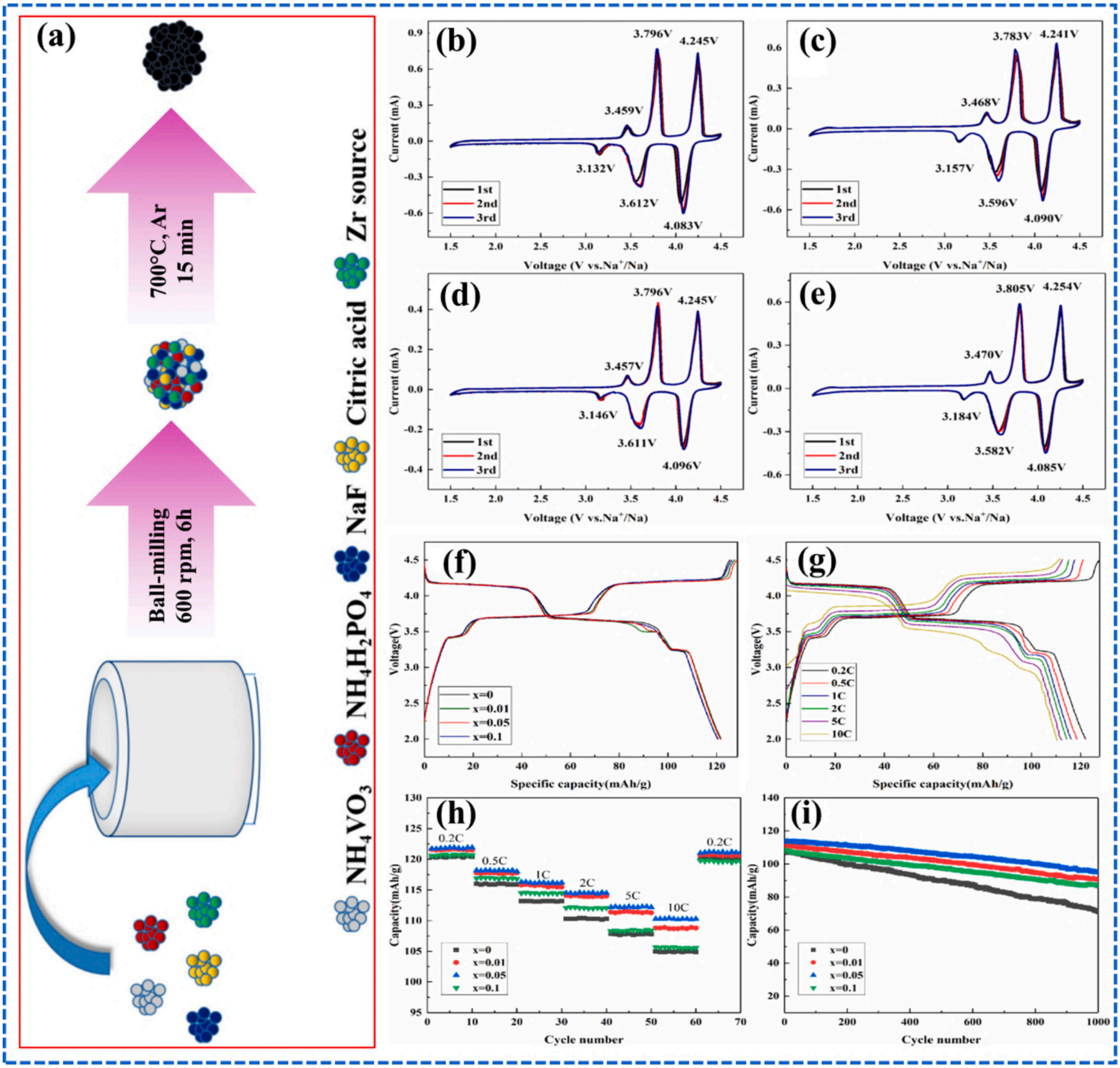

Fig. 16. (a) Schematic diagram for the preparation process of the $Na_3V_{2-x}Zr_x(PO_4)_2F_3/C$ samples, where x values of 0, 0.01, 0.05, and 0.1. The CV curves for the $Na_3V_{2-x}Zr_x(PO_4)_2F_3/C$ samples for four different values of x: (b) x = 0, (c) x = 0.01, (d) x = 0.05, and (e) x = 0.1, (f) The charging and discharging profiles of $Na_3V_{2-x}Zr_x(PO_4)_2F_3/C$ samples with varying values of x (0, 0.01, 0.05, and 0.1), (g) Charge-discharge profiles of the $Na_3V_{2-x}Zr_x(PO_4)_2F_3/C$, (h) Rate performances, (i) Cycling performance of the $Na_3V_{2-x}Zr_x(PO_4)_2F_3/C$ samples (x = 0, 0.01, 0.05, and 0.1). Reproduced with permission from [131].

Li and its nearest neighbour locations serving as the initial and final states. Path I/II traverses the tops of the C/Zr(1) and Zr(1)/X atoms, accordingly, for the unmodified and F/O/S passivated MXenes, while path III establishes a direct connection between the original and final states. Path I, as illustrated in Fig. 15(b) demonstrates a reduced diffusion barrier compared to path II across all scenarios, attributable to the robust interactions in the transition states. Path III consistently converges to Path I. Fig. 15(c) illustrates the diffusion barriers for Li along pathway I. Zr_2C exhibited the lowest energy barrier of 34 meV, attributed to a uniform surface charge distribution and the presence of a transition state at the apex of the Zr(2)–C bond. A local energy minimum of 17 meV was noted near the apex of the carbon atom. In contrast, other configurations presented significantly higher diffusion barriers. Specifically, the transition states for Zr_2CO_2 and Zr_2CF_2 were located above the Zr(1) atom and the Zr(1)–C bond, respectively, for Zr_2CS_2. The synthesis in an aqueous medium is expected to yield multiple –OH groups, which can be converted to –O groups through high-temperature annealing, enhancing Li stability. However, the semiconducting nature of these materials, combined with the presence of high diffusion barriers, continues to limit their practical applications. In contrast, the metallic characteristics of Zr_2CS_2 are particularly advantageous for battery applications [54].

Fig. 15(d) presents the atomic configurations of Zr_2C and its derivatives, Zr_2CX_2 (where X includes F, O, S, Se, and Te). Calculations for bare MXenes were performed to assess their non-magnetic, ferromagnetic, and antiferromagnetic properties. The ground state was found to

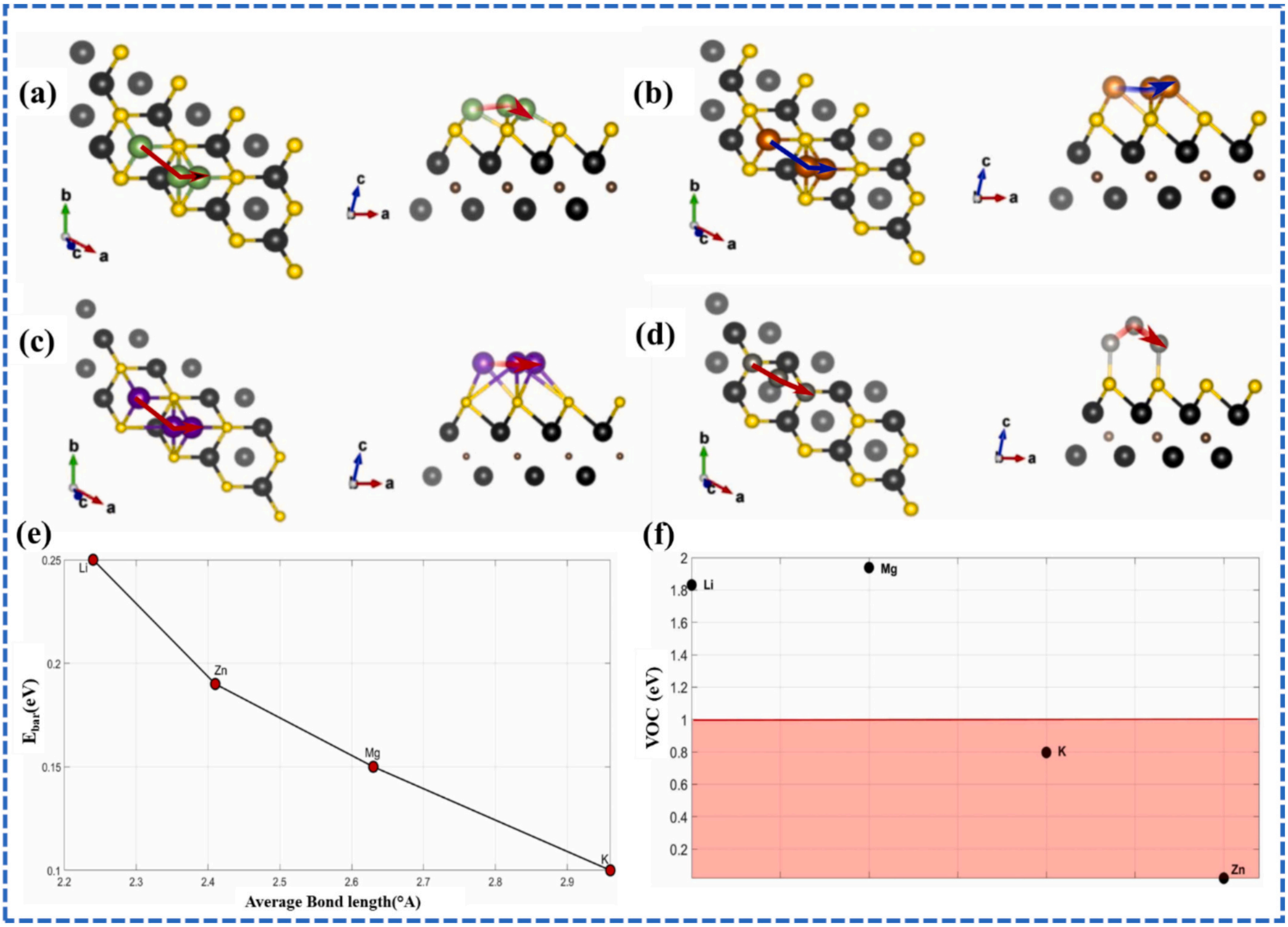

Fig. 17. The migratory paths for; (a) Li-ion, (b) K ion, (c) Mg ion, and (d) Zn ion. The arrows indicate the direction of migration. To enhance visibility, the colours of the most distant atoms is desaturated. Black spheres represent Zr atoms, brown C atoms, and yellow S atoms. (e) Bond length vs E_{bar} for all ions, (f) The open-circuit voltage for each ion considered in the study. Corresponding red horizontal line is drawn at 1 eV. Reproduced with permission from [125]. (For interpretation of the references to colour in this figure legend, the reader is referred to the web version of this article.)

exhibit antiferromagnetism, characterized by parallel spins in each Zr layer, with opposing spins in the top and bottom layers. This configuration was determined to be 10 meV per atom lower in energy compared to the ferromagnetic state, contradicting earlier calculations that employed a less stringent energy convergence criterion of 10^{-4} eV [127]. The in-plane lattice constant of Zr_2C was calculated to be 3.317 Å. The capping elements preferentially occupied positions above carbon atoms, coordinated equidistantly with three adjacent Zr atoms in both the top (Zr(1)) and bottom (Zr(2)) layers. This arrangement resulted in a non-magnetic state for all derivatives. The bond lengths between Zr(1) and the capping elements were measured at 2.12, 2.53, 2.69, and 3.01 Å for functionalization with O, S, Se, and Te, respectively, highlighting the influence of varying ionic radii. The Zr–F bond length was 2.33 Å, surpassing that of the Zr–O bond, which can be attributed to the different oxidation states of the anion-capped elements. The enhanced negative charge associated with the O group leads to a stronger Coulombic attraction with the positively charged Zr atoms [54].

Due to the limited availability of Li in the Earth's crust and potential safety risks, such as dendrite formation during charging, researchers have explored alternatives such as Na–ion and potassium–ion (K–ion) batteries. Na–ion batteries, in particular, have gained significant attention for their cost-effectiveness and high availability of Na. MXenes, particularly Zr–based MXenes, have shown promise as anode materials due to their excellent electrical conductivity and high energy storage potential, positioning them among the most effective electrodes for Na-ion batteries. For instance, Meng et al. [53] reported that Zr_2CO_2/$Zr_3C_2O_2$ serves as a promising anode for Na–ion batteries, demonstrating exceptional electrical conductivity, low open circuit voltage, low diffusion barriers (0.29/0.32 eV), and a high capacity of 474 mAh g^{-1} for Na storage. Variations in charge transfer and lattice mismatches significantly influence battery capacity, and increasing electrode thickness can lead to reduced ionic mobility. Meng and colleagues proposed that $Zr_3C_2O_2$ is well-suited as an anode material for Na-ion batteries due to its superior electronic conductivity, low equilibrium open circuit potential, and improved Na mobility and storage capacity compared to other MXenes [128,129].

In addition, Zha et al. [129] explored various Zr–MXene compositions for Na–ion batteries, demonstrating that $Zr_3C_2T_2$ (where T is O, F, OH, or S) and $Zr_3C_2O_2Na_4$ and $Zr_3C_2S_2Na_2$ exhibited excellent volumetric capacities of 913 and 777 mAh cm^{-3}, respectively. Further, $Zr_3C_2O_2$ and $Zr_3C_2S_2$ displayed outstanding mechanical strength, stability, and conductivity. It was noted that surface functional groups could influence theoretical capacity, open circuit voltage, and ionic mobility while increasing MXene thickness, which can lead to slightly reduced ionic mobility and elevated open circuit voltages. For instance, $Zr_3C_2O_2$ was observed to have a higher diffusion barrier and open circuit voltage compared to Zr_2CO_2 [81,130]. Theoretical Na-ion adsorption capacity depends heavily on lattice mismatch and charge transfer differences. Furthermore, incorporating Zr into the existing structure to form heterostructures can enhance overall system efficiency. Wang et al.

[131] demonstrated significant improvements by incorporating Zr^{4+} into $Na_3V_2(PO_4)_2F_3$ (NVPF) composites via a carbothermal reduction procedure using citric acid ($C_6H_8O_7$) as the carbon precursor. Their investigations focused on the effects of Zr^{4+} doping on crystal structures and morphologies, with electrochemical characteristics evaluated through galvanostatic charge-discharge (GCD), cyclic voltammetry (CV), and electrochemical impedance spectroscopy (EIS).

Experimental evidence indicated that modest levels of Zr^{4+} doping enhanced the electrochemical performance of NVPF. The $Na_3V_{2-x}Zr_x(PO_4)_2F_3/C$ samples, specifically $Na_3V_{1.95}Zr_{0.05}(PO_4)_2F_3/C$, exhibited superior rate and cycle performance compared to other samples with varying Zr content (x = 0, 0.01, 0.05, and 0.1), achieving specific capacity values of 121.8 and 110.3 mAh g^{-1} at 0.2 and 10C, respectively. The material also maintained a capacity retention of approximately 83.6 % after 1000 cycles at 5C. Analysis of kinetic characteristics suggested that the remarkable electrochemical performance of $Na_3V_{1.95}Zr_{0.05}(PO_4)_2F_3/C$ was attributed to enhancements in electronic conductivity and ion diffusion coefficients. The synthesis process of $Na_3V_{2-x}Zr_x(PO_4)_2F_3/C$ (x = 0, 0.01, 0.05, 0.1) is depicted in Fig. 16(a). To analyze the effects of Zr^{4+} doping on electrochemical characteristics, CV tests were conducted on $Na_3V_{2-x}Zr_x(PO_4)_2F_3/C$ samples within a voltage range of 1.5 to 4.5 V. As illustrated in Fig. 16(b–e), distinct redox peaks were identified around 3.46/3.13, 3.79/3.61, and 4.24/4.08 V. Based on the findings from the referenced study [132], it can be concluded that Na(2) ions exhibit lower stability compared to Na(1) ions due to their displacement from the stable position [133]. During the charging process, approximately 50 % of the Na(2) ions were extracted, leading to the reorganization of the $Na_{2.5}V_2(PO_4)_2F_3$ compound to reach a stable state. The extraction of the remaining Na(2) ions proved more challenging, contributing to increased redox peak intensity [134]. Analogous to the examination of Na(2) ion reorganization, it was noted that separation within Na(1) ions increased after the extraction of Na(2) ions. The $Na_3V_{1.95}Zr_{0.05}(PO_4)_2F_3/C$ sample exhibited the smallest potential difference, indicating minimal polarization. Fig. 16(f–i) presents the GCD patterns of $Na_3V_{2-x}Zr_x(PO_4)_2F_3/C$ samples at a rate of 0.2 C, with observed specific capacities of approximately 120.4, 121.8, 121.5, and 120.8 mAh g^{-1}. Among these samples, the $Na_3V_{1.95}Zr_{0.05}(PO_4)_2F_3/C$ sample demonstrated the highest specific capacity, with charge-discharge curves revealing three distinct plateaus at approximately 3.4, 3.7 and 4.2 V, attributed to the V^{4+}/V^{3+} redox peaks [135]. Consistent with CV analysis, the extraction and insertion of Na(2) ions occurred sequentially, resulting in the manifestation of three distinct working plateaus [136]. The observed voltage gap during the charging and discharging processes of the $Na_3V_{1.95}Zr_{0.05}(PO_4)_2F_3/C$ electrode was minimal, indicating enhanced Na^+ transport relative to the other samples [131].

Papadopoulou et al. [125] investigate Li, K, Mg, and Zn ion intercalation for the first time on the Zr_2CS_2 MXene monolayer surface, leveraging the property that S terminations reduce the diffusion barrier for the ions. The structures of Zr_2CS_2–Li, Zr_2CS_2–K, and Zr_2CS_2–Mg are identical, with Zr_2CS_2–Zn being the only difference due to the ion's location and the detachment of Zn from the surface of MXenes during migration. In their assessment of Zr_2CS_2 as a potential anode material for ion batteries, they analyzed adsorption energy, diffusion barrier energy, and open-circuit voltage for each ion. Their findings reveal that the K ion exhibits the highest mobility and the lowest open circuit voltage (VOC), suggesting that KIB offer faster charge/discharge rates and superior energy density compared to LIB, MIB, and ZIB when using S–terminated Zr–based materials as anode electrodes. The abundance and low cost of K further make KIB a promising alternative to LIBs [125].

The transition states for each ion are illustrated in Fig. 17(a–d), revealing that the migration pathways consistently occur at hollow sites on the MXene's surface, avoiding underlying atoms. For Li, K, and Mg, the migration pathway follows a Zr(2)–hollow–Zr(2) route, wherein the ions initiate their movement above a bottom-layer Zr atom, transition to a position above a void, and ultimately settle above a nearby bottom-layer Zr atom. In contrast, for the Zn ion, the initial position is over a termination atom, leading to its detachment from the surface at the transition state and residing in the vacuum without forming bonds with surface terminations (S atoms). This behaviour can be attributed to the exceedingly low adsorption energy of Zn. The relatively high energy barrier (E_{bar}) associated with the Zn ion's transition to the vacuum, surpassed only by the Li-ion scenario, reflects its lack of significant movement across the surface of Zr_2CS_2 MXene (Fig. 17(e)).

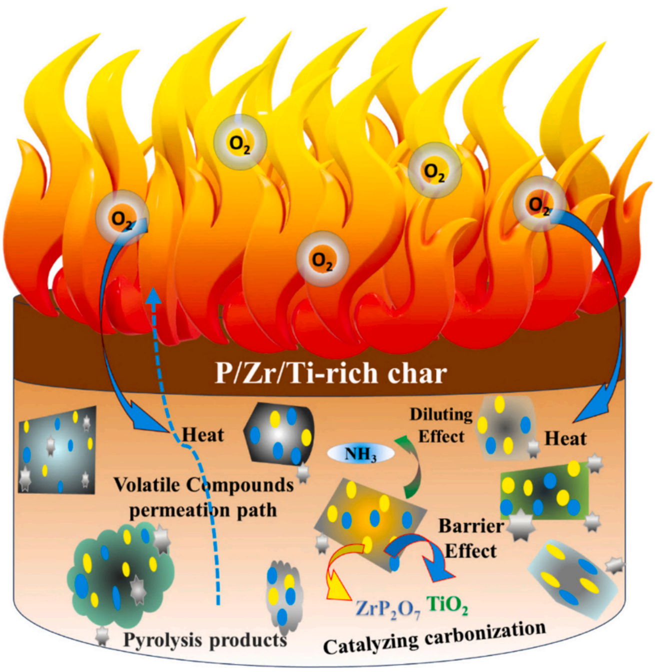

Fig. 18. Proposed fire retardant mechanism of Zr–MXene in the TPU. Reproduced with permission from [93].

Notably, the K ion exhibits the lowest diffusion barrier despite its stronger adsorption compared to Zn and its larger atomic mass relative to Li and Mg (39.0983 amu vs. 6.941 amu and 24.305 amu, respectively). This outcome aligns with predictions, as the average bond length between K and S is greater than that of the other ions, suggesting that K is more likely to break its bond with the termination atom and initiate migration with reduced energy requirements. The relationship between bond length and E_{bar} is depicted in Fig. 17(e).

Another critical parameter for selecting an anode material is the value of VOC. A negative VOC indicates that the ions do not adsorb onto the MXene surface but rather aggregate into clusters, while a VOC of zero signifies the maximum ion capacity of the material. For optimal rapid charge and discharge rates, the VOC should remain below 1 eV to minimize dendrite formation. Fig. 17(f) illustrates the VOC for each ion, highlighting the performance potential of the investigated materials [125].

Although KIBs, along with Na–ion technology, are emerging as cost-effective alternatives to Li–ion systems due to the abundance and affordability of K, challenges such as limited cycle life and thermal stability persist. Recent studies indicate that Zr–based MXenes can serve as high-performing anode materials for KIBs due to the presence of S termination atoms, which help to reduce the diffusion barrier for K–ions. DFT calculations show that S atoms in Zr_2C MXene preferentially occupy positions above carbon atoms in the surface layer, while Li, K, and Mg ions tend to occupy sites above Zr atoms in the lower MXene layer. In contrast, Zn ions are most stable when positioned directly above the S terminations. Further, computational approaches, including DFT, CASTEP, generalized gradient approximation (GGA), and BFGS algorithms, have shown that Zr_2CS_2 is metallic with a zero band gap, providing excellent electronic conductivity [125]. Papadopoulou et al.

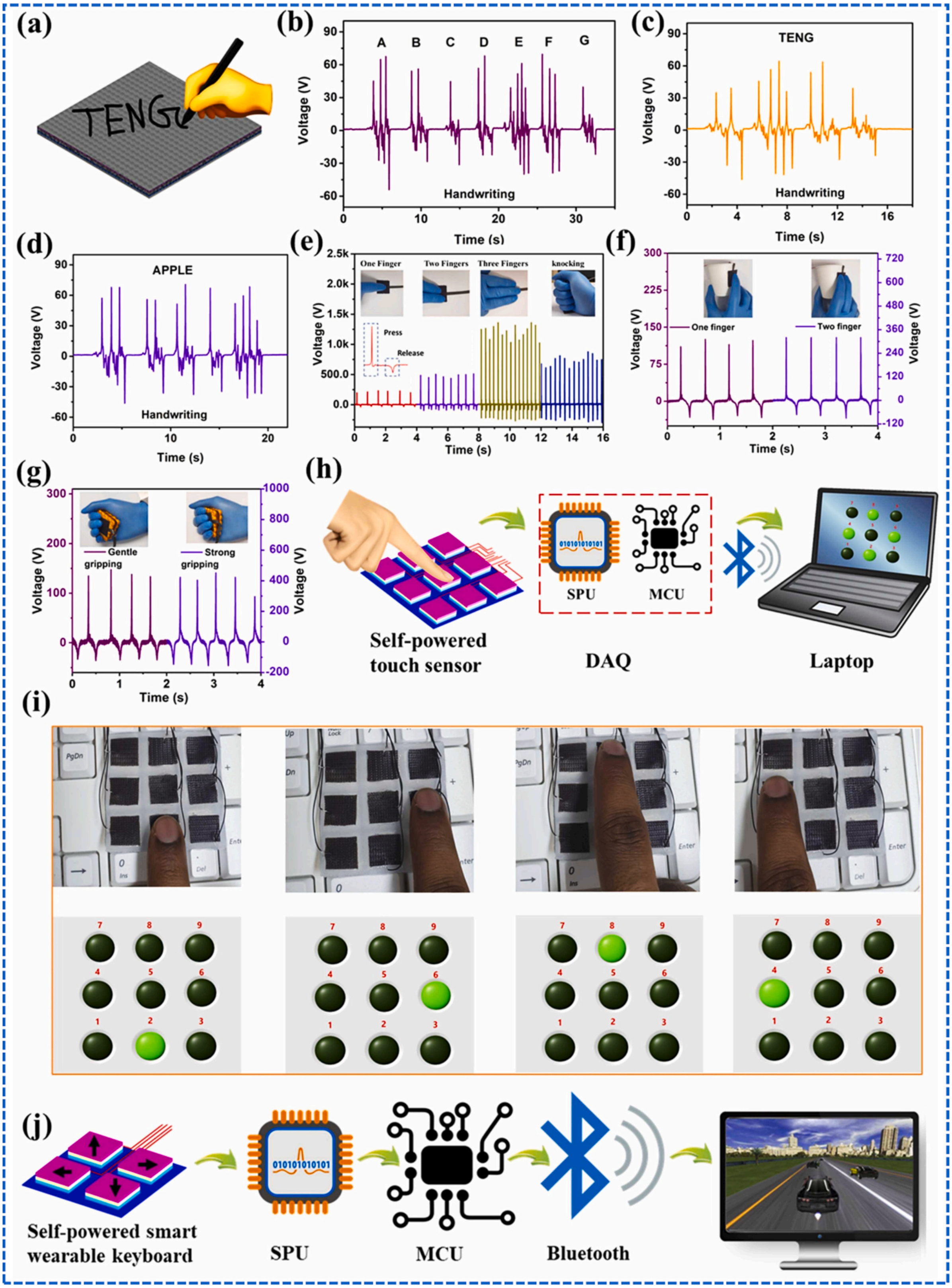

Fig. 19. (a) Schematic illustrates the handwriting recognition capabilities on the M–TENG surface, (b–d) Output voltage signals generated by the M–TENG capture handwriting details across its surface, (e) Variation in M–TENG voltage signals with different number of fingers interaction, (f) The output voltage response is recorded during the gripping and releasing of a paper cup, with inset images showing single-finger (left) and two-finger (right) interactions, (g) Voltage signals produced during the use of a flexible grip exerciser; inset shows gentle (left) and strong (right) gripping, (h) Schematic illustrates a real-time pressure tracking system, including a tactile sensor array, a data collecting system, Bluetooth connectivity, and LabVIEW data processing software. (i) Tactile sensor array visualized alongside its corresponding mapping image (j) Schematic illustration of the 2D car gaming control system, incorporating a tactile sensor array, data acquisition unit, MCU, Bluetooth, and a PC gaming interface. Reproduced with permission from [147].

[125] also suggest that K atoms create stronger hybrid states within the MXene structure than Li ions, and they bond robustly to MXene surfaces. These findings highlight that KIBs could achieve faster charge-discharge rates and better energy density than some traditional battery chemistries, such as Mg–ion and Zn–ion batteries [125,137–139].

4.4. *Fire retardant*

Zr–MXenes have emerged as a promising class of fire-retardant materials with significant potential in industrial applications. Their unique properties have been highlighted by Liu et al. [93], who demonstrated their effectiveness in enhancing fire resistance. However, achieving effective fire resistance typically requires compromising other material properties, such as mechanical strength or ductility. This challenge has hindered the successful synthesis of thermoplastic polyurethane (TPU) composites that combine both fire resistance and mechanical performance. Fig. 18 illustrates a proposed mechanism where a P/Zr/Ti–rich layer acts as a fire-retardant material, holding promise for a wide range of industrial uses. TPU itself is a highly attractive material due to its excellent mechanical properties, corrosion resistance, and self-lubricating characteristics. Recent advances, such as in situ loading of Zr amino tris(methylenephosphonate) (Zr AMP) onto the TiC surface, have led to substantial improvements in TPU's performance, including a dramatic increase in strain (2060 %), toughness (316 MJ m^{-3}), a 43.3 % increase in tensile strength, and enhanced fatigue resistance compared to conventional TPU matrices. The fire-retardant effect of Zr–MXenes, which includes physical barrier formation, catalytic carbonization, and dilution of flammability, offers an effective strategy for reducing flammability while maintaining material integrity, making it a promising approach for industrial applications [93].

4.5. *Energy harvesting*

Energy-harvesting systems present a promising solution for powering wearable electronic devices, addressing the challenge of ensuring uninterrupted operation while minimizing reliance on external energy sources and extending device longevity [140–142]. The development of a clean and environmentally compatible power supply is essential, especially since thermal energy and mechanical movements in the human body serve as reliable and readily accessible energy sources. Mechanical energy can be converted into electrical power through either the piezoelectric or triboelectric effect. Nanogenerators represent a novel, renewable, sustainable, and cost-effective approach to energy harvesting, particularly for powering wireless gas sensors [143,144]. Among the various types of nanogenerators, triboelectric nanogenerators (TENGs) have emerged as highly efficient mechanical energy harvesters due to their straightforward operation [145,146].

In a recent study, Rana et al. [147] developed a stretchy fabric-based TENG coated with a Zr metal–organic framework (MOF) and a hybridized nanocomposite. Their work resulted in creating a multilayered triboelectric nanogenerator (M–TENG) characterized by stretchability, humidity resistance, and high performance, making it suitable for applications in autonomous biomotion and tactile sensing. The M–TENG comprises a nanocomposite formed from Zr MOF–525 mixed with Ecoflex, combined with a layer of Ecoflex coated with cobalt-nano porous carbon (Co–NPC) and MXene. The performance of the TENG improved fourfold due to the homogeneous porosity and efficient charge accumulation provided by MOF–525. The Co–NPC features a porous architecture that enhances charge–trapping capabilities, while the MXene nanosheets act as micro capacitors, facilitating ion transport within the Ecoflex@Co–NPC@MXene nanocomposite. This composite structure enabled the effective collection of triboelectric charges from the charge-generating layer, leading to a substantial increase in negative charge buildup, quantified as a thirteenfold improvement in performance.

To further enhance performance, a 3D–printed microstructure was employed to increase the contact area and improve humidity resistance. Additionally, the use of knitted materials provided flexible electrodes due to their exceptional stretchability. The constructed M–TENG exhibited remarkable performance characteristics, including a power density of 25.7 W m^{-2}, a sensitivity of 149 V KPa^{-1}, humidity resistance, and a stretchability of 245 %, surpassing those of previously reported TENGs. The M-TENG's exceptional stretchability and sensitivity to mechanical stimuli have been demonstrated in various applications, such as wearable biomotion monitoring at low frequencies, biomechanical energy harvesting, precise character recognition, and self-powered tactile sensing. Real–time sensing capabilities were showcased using the LabVIEW interface, enabling control of virtual–reality automobile games through finger tracing. Thus, this study provides promising avenues for developing wearable energy–harvesting devices, self-sustaining sensing platforms, and interfaces that bridge humans and machines.

The findings from the M-TENGs also yielded positive results in tactile sensing applications with inherent self-powering capabilities. For instance, Fig. 19(a) illustrates the role of M–TENGs in a highly accurate handwriting identification system, which utilizes a polyvinyl chloride (PVC) plastic pen as the writing instrument. The voltage signals generated by the M–TENGs exhibited distinct peak patterns and magnitudes, influenced by the pressure applied by the pen tip. The voltages recorded in response to specific letters (e.g., “A, B, C, D, E, F, and G”) or words (e.g., “TENG” and “APPLE”) demonstrated consistency and reproducibility, as shown in the insets of Fig. 19(b), (c), and (d).

Moreover, Fig. 19(e) highlights the tactile detection capabilities of the M–TENG, indicating that voltage signals produced during finger contact were readily identifiable. The peak voltages generated by three fingers were approximately four times, twice, and 1.5 times greater than those produced by one finger, two fingers, and knocking, respectively. This behaviour suggests increased efficiency in the interaction area between the M–TENG and the human finger. Consequently, the M–TENG has the potential to function as a self-sustaining tactile sensor with built-in self-monitoring capabilities. The complex geometry and unique surface characteristics of the M–TENG device present significant potential for self-monitoring applications. To observe and analyze gripping actions, M-TENG was fabricated and wrapped around a paper cup, as depicted in Fig. 19(f). This demonstration included two distinct gripping techniques: one using a single finger and the other utilizing two fingers. The voltage signals in Fig. 19(f) reveal a positive pulse voltage signal when the paper cup is held and a negative pulse voltage pattern upon release [147].

The incorporation of multiple touch points, such as two fingers instead of one, significantly enhances the voltage impulse generated by the M–TENG system, attributed to the increased surface area interaction. This improvement highlights the potential of M–TENG for self-powered sensor applications. Flexible, soft, and self-monitoring devices, such as those enabled by M–TENG, are particularly promising in fields like rehabilitation training and health monitoring. Neurological disorders, including strokes, often lead to reduced grip strength, severely limiting an individual's ability to perform daily tasks. Rehabilitation programs targeting grip strength restoration have proven cost-effective and efficient strategies for managing such conditions.

To address these challenges, a novel, flexible grip exerciser was developed, utilizing output voltage signals to monitor rehabilitation progress. This device exhibits excellent flexibility, compressing and deforming during grip actions and rapidly returning to its original shape upon release. Voltage signals generated through triboelectrification, in both positive and negative directions, correspond directly to gripping and releasing actions, as illustrated in Fig. 19(g). A clear positive correlation was observed between applied grip strength and the resulting output voltage, enabling the device to autonomously track grip strength recovery. Furthermore, converting the tactile sensor's output signal into visual data enhances its viability and usability. A tactile sensor array was evaluated for real-time analysis, comprising a pressure monitoring system with a contact sensor array, a data acquisition device, and a LabVIEW-based processing program, as shown in Fig. 19(h). Changes in

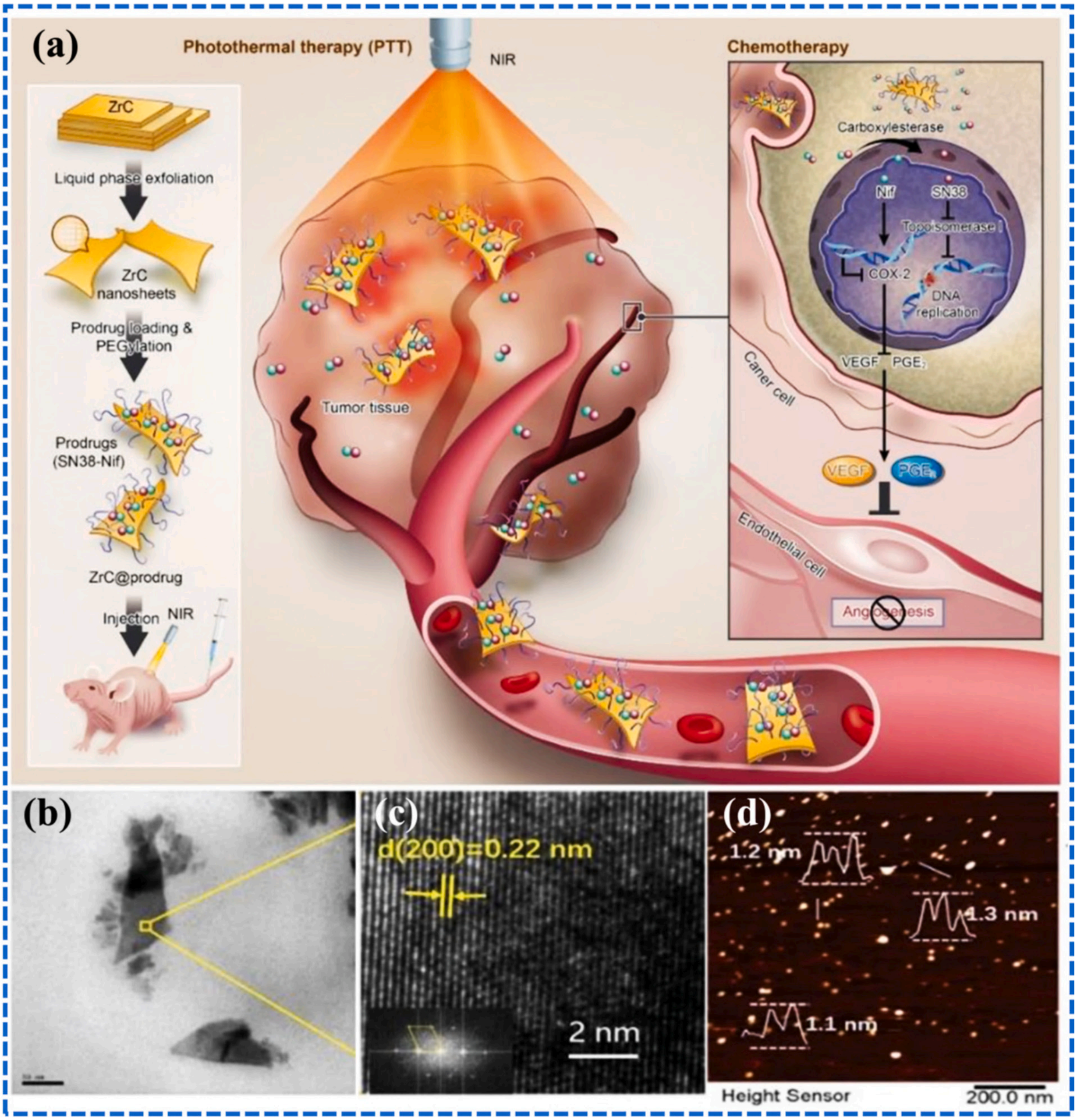

Fig. 20. (a) Schematic representation of a 2D biodegradable ZrC@prodrug (SN38-Nif) system designed for in vivo tumour photo-chemotherapy: Liquid-phase exfoliation of ZrC NSs in water, (b) TEM, and (c) HRTEM images (inset displaying the corresponding SAED pattern) of ZrC NSs, (d) Atomic force microscopy image depicting the ZrC NSs. Reproduced with permission from [158].

touchpoint colour (Fig. 19(i)) allowed for precise identification of contact areas, and touch action trajectories could be effectively recorded.

The rapid advancements in virtual reality (VR) technology have further expanded potential applications of M-TENG systems into areas such as immersive gaming and interactive engagement. A 2D VR game was experimentally demonstrated to validate the efficacy of the M–TENG array and its control interface. The real-time control system, depicted schematically in Fig. 19(j), comprises sensors, signal-processing circuitry, and a microcontroller unit (MCU) [147]. The MCU, integrated with a wireless transmitter module communicates with a personal computer running virtual gaming software. Upon activation of a touch sensor, signals are processed by the signal processing unit (SPU), which eliminates irrelevant noise. The MCU then transmits the processed signal wirelessly to the computer via Bluetooth, facilitating control in VR applications. Pre-set finger configurations enable intuitive control over functions like steering and speed adjustment in a VR-based driving game [147]. This research highlights the potential to enhance triboelectric performance and introduces a groundbreaking design for multi-functional, self-powered wearable sensors. These innovations pave the way for advancements in human-machine interactions, biomotion energy capture, and versatile sensing technologies.

4.6. *Anti-corrosive coatings*

Developing durable, high-performance anti–corrosive coatings is essential for applications, including steel structures, marine vessels, machinery, and power facilities [148]. Recent advances have explored various nanomaterials for this purpose, each with unique benefits and challenges. Among these, 2D materials, particularly zirconium phosphate (ZrP) and graphene oxide-zirconium dioxide (GO–ZrO_2), have

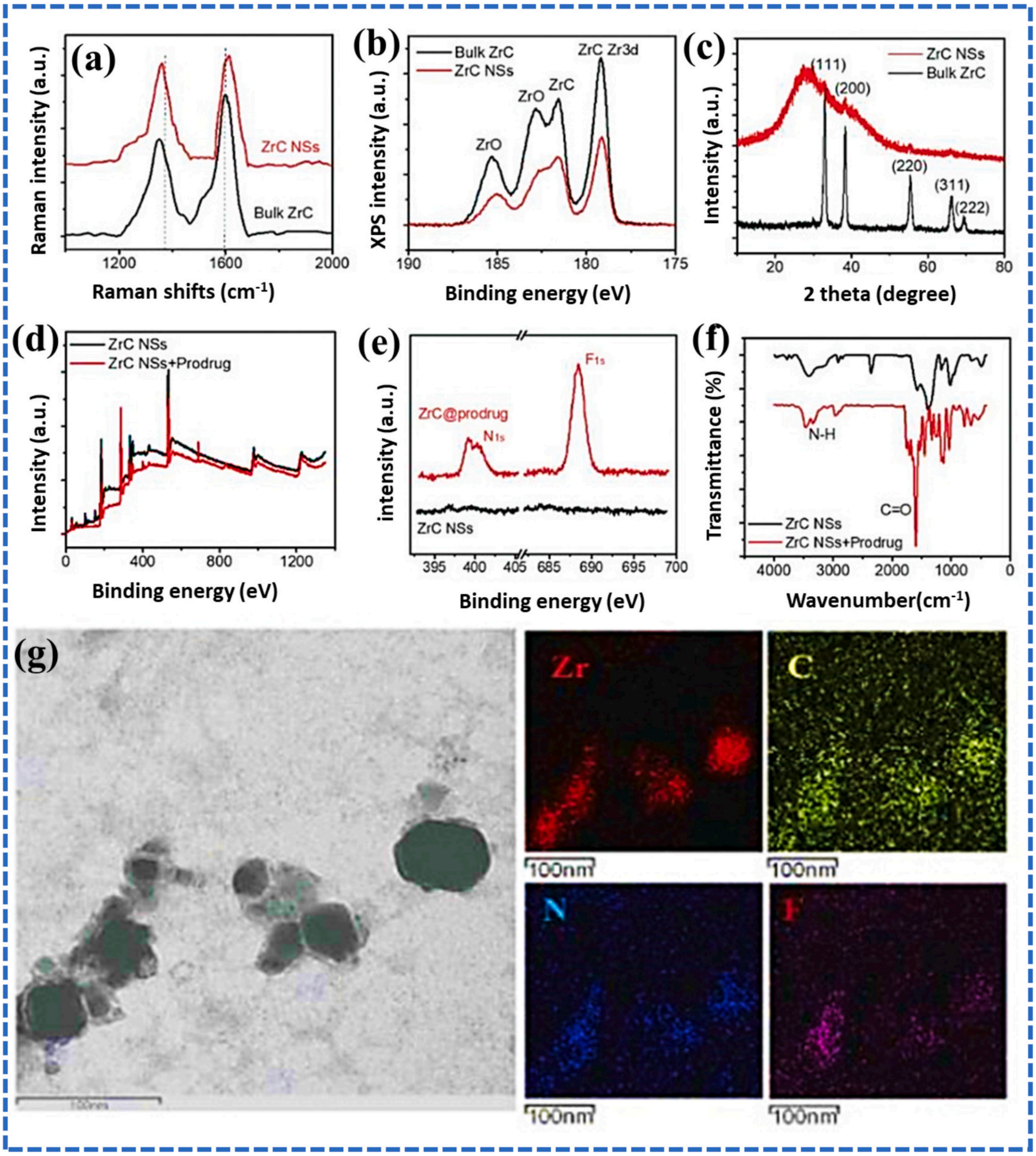

Fig. 21. (a) Raman spectra of bulk ZrC and ZrC NSs, (b) XPS spectra of bulk ZrC and ZrC nanoparticles, (c) XRD patterns of bulk ZrC and ZrC NSs, (d, e) XPS spectra of ZrC NSs and ZrC@prodrug, (f) FTIR spectra of ZrC, (g) STEM images of ZrC@prodrug. Reproduced with permission from [158].

shown significant promise. The incorporation of graphene oxide (GO) with nanoparticles has been found to improve structural integrity and enhance corrosion resistance [7,149]. For instance, GO–ZrO_2 hybrids synthesized using silane coupling agents and dispersed in polymer matrices demonstrated exceptional chemical, wear, and corrosion resistance [150]. Studies further highlighted the performance of GO–ZrO_2 epoxy hybrid coatings, which maintained low capacitance between the metal surface and electrolytes (e.g., 3.5 % NaCl) even after prolonged immersion, showcasing their durability and efficacy [151,152].

Similarly, MXene-based composites have emerged as effective materials for advanced coatings. For instance, He et al. [116] synthesized MXene–ZrP@PDA composite by functionalizing a heterojunction comprising MXene and exfoliated α-ZrP with polydopamine (MZP). This composite was incorporated into a waterborne epoxy (WEP) coating to create the MZP/WEP system. Results revealed a significant enhancement in anticorrosion properties, with the corrosion rate of MZP/WEP (1.70×10^{-4} mpy) reduced by an order of magnitude compared to the baseline WEP coating (1.28×10^{-3} mpy). Additionally, the average coefficient of friction (COF) of MZP/WEP showed an impressive reduction of 82.06 % relative to the blank WEP coating. These findings underscore the efficacy of MXene-ZrP@PDA in improving the anticorrosion and anti-wear characteristics of WEP coatings, providing promising avenues for metal preservation [153]. These results highlight the potential of ZrO_2–based nanocomposites as robust materials for advanced anticorrosive applications.

4.7. Bio-medical

Extensive research into Zr-based MXenes, particularly ZrC, shows great promise in addressing critical challenges in biomedical applications, including cancer treatment [154]. Despite advances in chemotherapy, radiation therapy, and surgery, these conventional methods often face limitations such as systemic toxicity, low bioavailability, tumour angiogenesis, poor tissue penetration, and complications like inflammation induced by treatment. These challenges contribute to suboptimal success rates and patient survival [155]. While advances in nanomedicine aim to improve treatment efficacy, the translation of

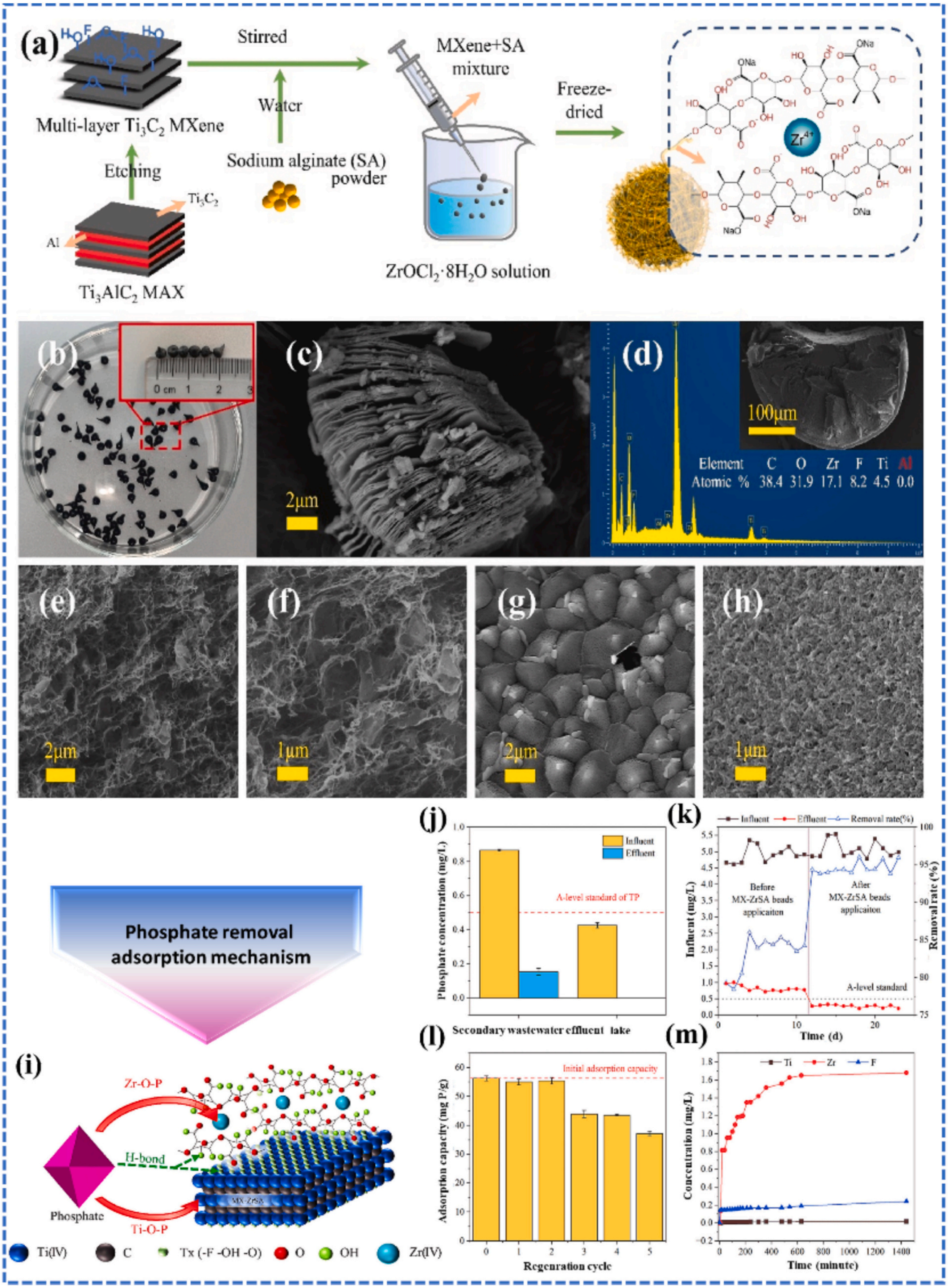

Fig. 22. (a) Fabrication process of MX–ZrSA beads, (b) Optical image of MX–ZrSA beads, (c) SEM image of Ti_3C_2–MXene, (d) SEM–EDS analysis of MX–ZrSA beads, (e-f) Cross-sectional SEM images of MX-ZrSA beads (g-h) Cross-sections of ZrSA beads, (i) Schematic of adsorption mechanism for MX–ZrSA beads, (j) Phosphate removal capacity and the corresponding starting and residual quantities of phosphate in second wastewater effluent and a lake using MX–ZrSA beads, (k) Phosphate concentration in influent and effluent and phosphate removal rate of the laboratory-scale AAO reactor during 23-day operational period, (l) Adsorption capacity of MX–ZrSA beads post-regeneration using 0.1 M NaOH, (m) Leaching profile of metal ions and F- ions in water. Reproduced with permission from [89].

research findings into clinical trials has often been challenging, with many studies failing to progress to this stage.

Recent studies have demonstrated the remarkable bio-photonic properties of ZrC MXenes, which can be engineered into nanosheets for advanced photothermal therapy (PTT)–based photosensing. For example, researchers developed an anticancer prodrug using SN38 and niflumic acid (Nif), showcasing ZrC's potential in cancer treatment through precision nanomedicine approaches. Mouse model studies validated the efficacy of ZrC nanosheets in achieving targeted drug delivery and precise tumour ablation, positioning ZrC as a promising candidate for precision oncology. PTT, in particular, stands out for its noninvasiveness, minimal collateral damage to healthy tissues, and potent anticancer activity. Atomic properties of Zr, including its thermoplasmonic effects, high oxidation state, superior charge density, bond polarization, and carboxylate O-atom affinity, contribute to its exceptional drug-loading capacity and reduced toxicity. Particularly, ZrC achieves an impressive photothermal conversion rate of 62.1 % under 1064 nm irradiation and can load drugs at an ultrahigh capacity of approximately 800 %. This high efficiency enables its effective application in photothermal and photodynamic therapy (PDT) [156,157].

Liu et al. [158] explored the role of 2D ZrC in prodrug delivery, demonstrating that 2D ZrC can accumulate in tumour tissue and release prodrugs via photo-hyperthermia, converting them into the active agents SN38 and Nif. This process enhances the bioavailability of SN38 and modulates the tumour microenvironment, thereby reducing inflammation induced by chemotherapy or hyperthermia [159,160]. The study also investigated the potential of ultra-thin 2D ZrC nanosheets as candidates for cancer treatment, employing a combination of near-infrared II (NIR-II) PDT and a photo-controlled drug delivery platform. The ZrC@prodrug formulation benefits from enhanced permeability and retention (EPR) properties, leading to effective accumulation in tumour tissues. The release of prodrugs is triggered by photo-hyperthermia induced by ZrC, facilitated by carboxylesterase—an enzyme typically upregulated in cancer cells (Fig. 20(a)). Additionally, ZrC promotes selective accumulation of prodrugs, further enhancing SN38 bioavailability. The COX–2 inhibitor Nif effectively suppresses tumour angiogenesis by targeting the COX–2/PGE2/VEGF signaling pathway.

The ZrC@prodrug formulation effectively regulates the tumor microenvironment (TME) and alleviates inflammation induced by chemotherapy and hyperthermia, thus fostering a more favorable environment for treatment. Notably, both ZrC and the prodrug demonstrate minimal toxicity. The synergistic combination of photothermal therapy and chemotherapy resulted in successful in vivo tumor ablation across various xenograft models, highlighting the efficacy of ZrC@prodrug biophotonic nanoplatforms in inhibiting tumor progression, preventing recurrence, and reducing metastasis [158].

In the synthesis of ZrC nanosheets (ZrC NSs), Liu et al. [158] employed a liquid-phase exfoliation technique, as illustrated in Fig. 20 (a). The stoichiometric ratio of ZrC nanosheets was determined via EDS. Further, TEM images (Fig. 20(b)) confirmed the ultrathin nature of ZrC NSs, showing a lateral dimension ranging from approximately 50 to 200 nm. HRTEM and SAED analyses (Fig. 20(c)) revealed lattice fringes with an interplanar spacing of 0.22 nm, corresponding to the (200) crystallographic planes of ZrC. The fast Fourier transform (FFT) of the crystal lattice exhibited expected reflections consistent with the Fm3m space group. Atomic force microscopy (Fig. 20(d)) further confirmed the thickness of ZrC nanosheets, ranging from 1.1 to 1.4 nm, indicative of single or double-layer structures.

Raman spectra for both bulk ZrC and ZrC NSs (Fig. 21(a)) and XPS analyses (Fig. 21(b)) confirmed the chemical composition of the materials. XRD patterns (Fig. 21(c)) exhibited similar reflection peaks for bulk ZrC and exfoliated ZrC NSs, attributable to the FCC structure of ZrC. XPS investigations (Fig. 21(d)) assessed the binding affinity of the prodrug to ZrC NSs, with magnified areas (Fig. 21(e)) revealing prominent peaks at 399 eV and 688 eV corresponding to N1s and F1s orbitals, respectively, after prodrug loading. Moreover, FTIR spectra (Fig. 21(f)) indicated peaks at 1627 cm^{-1} and 2920 cm^{-1}, associated with C=O and NH stretching vibrations of the prodrug. Scanning transmission electron microscopy (STEM) combined with EDS mapping (Fig. 21(g)) confirmed the co-localization of Zr, C, F, and N elements in ZrC@prodrug, validating effective prodrug deposition.

In addition to this, Zr dioxide nanoparticles (ZrO_2 NPs) have significant implications in medicine and pharmacy due to their dependable therapeutic biomedical applications. These applications include their use as anticancer, antibacterial, and antioxidant agents, as well as in tissue engineering. A review by Bannunah et al. [161] explores various synthesis methods for ZrO_2 NPs and their broad medical and biological applications. ZrO_2 is recognized for its mechanical strength, biocompatibility, and chemical stability, making it a promising candidate in biomimetic scaffolds. ZrO_2 NPs exhibit significant anticancer activity against various cancer cell types, demonstrate antibacterial properties against multiple bacterial strains, and showcase exceptional antioxidant capabilities. Furthermore, ZrO_2 nanocomposites have notable biosensing potential, particularly in detecting glucose and other biological entities with high sensitivity.

4.8. Water treatment

Phosphorus (P) is essential for cellular functions across all living organisms [162]. However, excess P in aquatic systems can severely impact these ecosystems, leading to hypoxia or anoxia, reduced phytoplankton diversity, and higher water treatment costs due to toxic microcystin production from algal blooms [163]. Consequently, regulatory bodies have imposed strict P limits; for instance, the U.S. Environmental Protection Agency (USEPA) mandates a maximum concentration of 25 parts per billion (ppb) of total P in surface waters to mitigate eutrophication in lakes and reservoirs [164].

To address this issue, Song et al. [89] developed sodium alginate (SA) beads embedded with a Ti_3C_2–based MXene, forming MX–ZrSA beads. These beads were optimized for phosphate adsorption through batch experiments, with the MXene enhancing the physical properties of the SA beads and providing active chemisorption sites. Kinetic and isotherm models confirmed improved adsorption, and control ZrSA beads without MXene were also tested. Regeneration and ion leaching studies demonstrated the beads' reusability, phosphate recovery potential, and environmental safety. Phosphate removal efficiency was further validated in a real-world water sample using a continuous-flow anaerobic-anoxic-oxic (AAO) reactor.

Fig. 22(a) illustrates the fabrication process of the Ti_3C_2–MXene embedded Zr–crosslinked SA (MX-ZrSA) beads, followed by an evaluation of their phosphate adsorption under various conditions. Fig. 22(b) shows the morphology of the MX–ZrSA beads, which have a smooth surface and black colour, with a droplet-like shape and dimensions between 3 and 4 mm. The accordion-like structure of the Ti_3C_2–based MXene formed during the in-situ etching process is depicted in Fig. 22 (c). SEM–EDS analysis (Fig. 22(d)) reveals that the beads consist of five elements: C, O, Zr, F, and Ti, with no detectable Al from the MAX phase due to its complete removal during etching. Cross-sectional images of the beads at magnifications of 5000× (Fig. 22(e–f)) and 10,000× (Fig. 22(g–h)) show differences in the inner structure. The ZrSA beads, without MXene, exhibit a denser inner structure, likely due to their lower mechanical resilience. In contrast, the MXene flakes in MX–ZrSA beads are uniformly dispersed and interconnected, forming an unsecured network-like architecture that supports the bead's structural integrity. This configuration enhances the adsorption capacity of the beads by providing more contact sites for phosphate adsorption.

Fig. 22(i) illustrates the proposed mechanism of phosphate adsorption by MX–ZrSA beads, where chemical adsorption occurs through the formation of Zr–O–P and Ti–O–P complexes. The presence of –OH, –O, and –F groups improves the hydrophilicity of the beads, facilitating better interaction and hydrogen bonding with phosphate in aqueous solutions. The adsorption capacity of MX–ZrSA beads was evaluated

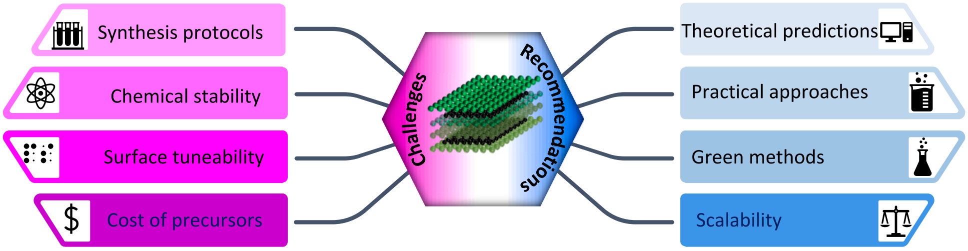

Fig. 23. Schematic view of associated challenges and future recommendations for Zr-MXenes.

using secondary wastewater effluent and lake water samples (Fig. 22(j)), with initial phosphate concentrations of 0.87 mg L^{-1} and 0.43 mg L^{-1}, respectively. After adsorption, phosphate concentrations decreased to 0.15 mg L^{-1} and 0.00 mg L^{-1}, respectively.

The AAO system, commonly used for biological phosphate removal in wastewater treatment, is cost-effective but sometimes limited by unfavourable conditions that affect bioactivity. As demonstrated by MX-ZrSA beads, the adsorption method offers an effective, cost-efficient alternative that generates no chemical sludge, unlike traditional chemical methods. In laboratory-scale AAO reactor tests (Fig. 22(k)), MX-ZrSA beads were used as a filler material in the outflow pipe of a sedimentation tank, leading to a reduction in phosphate concentration from 0.77 mg L^{-1} (above the 0.5 mg L^{-1} limit set by GB 18918–2002) to 0.27 mg L^{-1} after 12 days of operation.

Reusability, a key factor for practical application, was evaluated using a 0.1 M NaOH regeneration solution (Fig. 22(l)). The MX-ZrSA beads maintained 97.5 % and 98.5 % of their original adsorption capacity after the first two regeneration cycles. Metal ion and F ion leaching were assessed, with minimal concentrations of Ti ions (0.0016 mg L^{-1}) and F- ions (0.2400 mg L^{-1}) detected after 1440 min, indicating minimal environmental risk from ion leaching (Fig. 22(m)) [89].

5. Challenges and future perspectives

The development of non-Ti–based MXenes, particularly Zr–based MXenes, represents an exciting frontier in 2D layered materials research due to their unique structural and chemical properties, offering potential for diverse applications. However, integrating Zr–based MXenes into practical applications remains challenging. As summarized in Fig. 23, key obstacles include safety risks associated with hazardous chemicals in traditional synthesis methods, limited colloidal stability in physiological environments, and difficulties in scaling up production processes.

Although several Zr MAX phases have been theoretically predicted, only a few have been synthesized experimentally [165], highlighting a need for both empirical and computational studies to fully explore the capabilities of Zr–based MXenes. Such studies are essential to advance applications in catalysis, energy storage, and biomedicine. Currently, the field is nascent, with most research focused on theoretical modeling rather than experimentally validated, scalable synthesis methods. The high cost and limited availability of precursor materials also complicate efforts to synthesize Zr–based MAX phases practically. Further research is required to overcome these obstacles and to develop hybrid or heterostructures involving Zr–based MXenes, which could enhance their functionality for specific applications. To integrate Zr–based MXenes into real–world applications, addressing the issues related to the hazardous chemicals involved in synthesis, inadequate colloidal stability in physiological conditions, and scalability for industrial production is crucial [166].

Furthermore, as interest in Zr–based MXenes grows, establishing sustainable disposal and recycling methods will be essential to mitigate their environmental impact. This includes developing recycling processes and safe degradation methods to minimize ecological risks. Research into the environmental impact of MXenes, such as the effects of degradation products and potential long-term implications for ecosystems, is still in preliminary stages and requires further study [167]. Implementing a circular economy model for Zr–based MXenes, focusing on recycling and resource recovery, could help reduce their environmental footprint. Future developments should prioritize improving material performance while minimizing ecological impacts, supporting the broader and more sustainable use of MXenes across various industries [168].

6. Conclusions

This review provides a comprehensive update on recent advancements in Zr and Zr–based MXene materials, emphasizing their distinctive properties and growing applicability across various domains. Emerging research indicates that Zr–MXene composites, including both Zr–based MXenes and their parent MAX phases, exhibit remarkable structural, electronic, optical, thermoelectric, and electrochemical properties, positioning them as highly promising materials for diverse technological applications. These materials have demonstrated effectiveness in fields such as optoelectronics, photonics, energy storage (e.g., Li– and Na–ion batteries), and anticorrosive coatings. Additionally, biomedical applications like targeted cancer therapy and biosensing benefit from their biocompatibility and functional versatility. The unique adaptability, stability, and performance of Zr–based MXenes in harsh environments highlight their transformative potential. This review aims to inspire continued exploration and innovative applications of Zr–MXenes, particularly toward sustainable and high-performance solutions in advanced material science.

Declaration of competing interest

The authors declare that they have no known competing financial interests or personal relationships that could have appeared to influence the work reported in this paper.

Acknowledgement

The authors, G.E. and A.H., thank Sunway University, Malaysia, for awarding the PhD Studentship with grant number (Ethics No: **PGSUREC2023/064** and **PGSUREC2023/006**).

Data availability

No data was used for the research described in the article.

References

[1] M.A.U. Din, et al., Synthesis of MXene-based single-atom catalysts for energy conversion applications, Chem. Eng. J. 474 (2023) 145700.
[2] I. Hussain, et al., Mo-based MXenes: synthesis, properties, and applications, Adv. Colloid Interf. Sci. 324 (2024) 103077.
[3] K. Zhang, et al., Insights into different dimensional MXenes for photocatalysis, Chem. Eng. J. 424 (2021).
[4] R.R. Raja Sulaiman, et al., Structurally modified MXenes-based catalysts for application in hydrogen evolution reaction: a review, Catalysts 12 (12) (2022) 1576.

[5] Y. Wu, et al., Recent advances in transition metal carbides and nitrides (MXenes): characteristics, environmental remediation and challenges, Chem. Eng. J. 418 (2021).

[6] A. Sokolov, et al., Partially oxidized MXene $Ti_3C_2T_x$ sheets for memristor having synapse and threshold resistive switching characteristics, Adv. Electr. Mat. 7 (2) (2021) 2000866.

[7] A. Hanan, et al., Co_2FeO_4@ rGO composite: towards trifunctional water splitting in alkaline media, Int. J. Hydrog. Energy 47 (80) (2022) 33919–33937.

[8] A. Hussain, et al., Preparation of reduced graphene oxide decorated two-dimensional WSe2 nanosheet sensor for efficient detection of ethanol gas, Physica E: Low-dimensional Systems and Nanostructures 147 (2023) 115574.

[9] H. Chang, et al., Towards high-performance electrocatalysts and photocatalysts: design and construction of MXenes-based nanocomposites for water splitting, Chem. Eng. J. 421 (2021).

[10] T.J. Xu, et al., MXenes@metal-organic framework hybrids for energy storage and electrocatalytic application: insights into recent advances, Chem. Eng. J. 470 (2023).

[11] M. Pogorielov, et al., MXenes-A new class of two-dimensional materials: structure, properties and potential applications, Nanomaterials (Basel) 11 (12) (2021).

[12] I. Hussain, et al., Double transition-metal MXenes: classification, properties, machine learning, artificial intelligence, and energy storage applications, Mat. Today Phys. 42 (2024) 101382.

[13] C. Wen, et al., Exfoliation behavior and superior photothermal conversion performance of MXenes beyond $Ti_3C_2T_x$, Chem. Eng. J. 472 (2023) 144921.

[14] L.P. Hao, et al., Synergistic integration of MXene and metal-organic frameworks for enhanced electrocatalytic hydrogen evolution in an alkaline environment, Catalysts 13 (5) (2023) 802.

[15] M. Liu, et al., Spinel compounds as multivalent battery cathodes: a systematic evaluation based on ab initio calculations, Energy Environ. Sci. 8 (3) (2015) 964–974.

[16] L. Yu, A. Zunger, Identification of potential photovoltaic absorbers based on first-principles spectroscopic screening of materials, Phys. Rev. Lett. 108 (6) (2012) 068701.

[17] J. Greeley, et al., Computational high-throughput screening of electrocatalytic materials for hydrogen evolution, Nat. Mater. 5 (11) (2006) 909–913.

[18] S. Curtarolo, et al., The high-throughput highway to computational materials design, Nat. Mater. 12 (3) (2013) 191–201.

[19] N. Mounet, et al., Two-dimensional materials from high-throughput computational exfoliation of experimentally known compounds, Nat. Nanotechnol. 13 (3) (2018) 246–252.

[20] S. Haastrup, et al., The computational 2D materials database: high-throughput modeling and discovery of atomically thin crystals, 2D Mat. 5 (4) (2018) 042002.

[21] N.C. Frey, et al., Prediction of synthesis of 2D metal carbides and nitrides (MXenes) and their precursors with positive and unlabeled machine learning, ACS Nano 13 (3) (2019) 3031–3041.

[22] B. Anasori, M.R. Lukatskaya, Y. Gogotsi, 2D metal carbides and nitrides (MXenes) for energy storage, Nat. Rev. Mater. 2 (2) (2017) 16098.

[23] M. Khazaei, et al., Novel electronic and magnetic properties of two-dimensional transition metal carbides and nitrides, Adv. Funct. Mater. 23 (17) (2013) 2185–2192.

[24] N.C. Frey, et al., Tuning noncollinear spin structure and anisotropy in ferromagnetic nitride MXenes, ACS Nano 12 (6) (2018) 6319–6325.

[25] M. Nasir, et al., Zirconium metal-based MAX phases Zr_2 AC (a= Al, Si, P and S): a first-principles study, Int. J. Mod. Phys. B 28 (32) (2014) 1550022.

[26] W. Voigt, Ueber die Beziehung zwischen den beiden Elasticitätsconstanten isotroper Körper, Ann. Phys. 274 (12) (1889) 573–587.

[27] A. Reuß, Berechnung der fließgrenze von mischkristallen auf grund der plastizitätsbedingung für einkristalle, ZAMM-Journal of Applied Mathematics and Mechanics/Zeitschrift für Angewandte Mathematik und Mechanik 9 (1) (1929) 49–58.

[28] X.-H. Zha, et al., Non-MAX phase precursors for MXenes, in: B. Anasori, Y. Gogotsi (Eds.), 2D Metal Carbides and Nitrides (MXenes): Structure, Properties and Applications, Springer International Publishing, Cham, 2019, pp. 53–68.

[29] K. Chen, et al., MAX phase Zr_2SeC and its thermal conduction behavior, J. Eur. Ceram. Soc. 41 (8) (2021) 4447–4451.

[30] G. Li, et al., 2D titanium carbide (MXene) based films: expanding the frontier of functional film materials, Adv. Funct. Mater. 31 (46) (2021) 2105043.

[31] J. Zhu, A. Chroneos, U. Schwingenschlögl, Nb-based MXenes for Li-ion battery applications. Physica status solidi (RRL), Rapid Research Lett. 9 (12) (2015) 726–729.

[32] I. Hussain, et al., V-MXenes for energy storage/conversion applications, ChemSusChem 17 (15) (2024) e202400283.

[33] V. Mehta, et al., S-functionalized Mo_2C monolayer as a novel electrode material in Li-ion batteries, J. Phys. Chem. C 123 (41) (2019) 25052–25060.

[34] M. Li, et al., Element replacement approach by reaction with Lewis acidic molten salts to synthesize Nanolaminated MAX phases and MXenes, J. Am. Chem. Soc. 141 (11) (2019) 4730–4737.

[35] X. Shao, et al., Zr_2 Si: an antiferromagnetic Dirac MXene, Phys. Chem. Chem. Phys. 20 (6) (2018) 3946–3952.

[36] X. Zhang, et al., Prediction of an ultrasoft graphene allotrope with Dirac cones, Carbon 105 (2016) 323–329.

[37] S. Liu, et al., Ultrafast photonics applications of zirconium carbide as a novel mode-locker for fiber lasers, J. Mater. Chem. C 9 (47) (2021) 16985–16990.

[38] S. Venkateshalu, A.N. Grace, MXenes—A new class of 2D layered materials: synthesis, properties, applications as supercapacitor electrode and beyond, Appl. Mater. Today 18 (2020) 100509.

[39] L. Toth, Transition Metal Carbides and Nitrides, Elsevier, 2014.

[40] J.H. Park, C.H. Jung, J.Y. Park, Temperature dependency of the LPCVD growth of ZrC with the $ZrCl_4$–CH_4–H_2 system, Surf. Coat. Technol. 203 (3–4) (2008) 324–328.

[41] Y. Hou, et al., High temperature electromagnetic interference shielding of lightweight and flexible ZrC/SiC nanofiber mats, Chem. Eng. J. 404 (2021) 126521.

[42] R. Ganter, et al., Laser-photofield emission from needle cathodes for low-emittance electron beams, Phys. Rev. Lett. 100 (6) (2008) 064801.

[43] W.A. Mackie, P.R. Davis, Single-crystal zirconium carbide as a high-temperature thermionic cathode material, IEEE Trans. Electron Devices 36 (1) (1989) 220–224.

[44] X. He, et al., One-pot fabrication of an MXene-ZrP@ PDA heterojunction for enhanced corrosion/Wear resistance of waterborne epoxy coatings, Ind. Eng. Chem. Res. 61 (34) (2022) 12576–12589.

[45] R.M.R. Prince, et al., ZrC-impregnated titanium-based coating as an effective lubricating barrier for artificial hip prosthesis, Mat. Perf. and Charact. 10 (1) (2021) 189–205.

[46] M. Jiang, et al., A comparative study of low energy radiation responses of SiC, TiC and ZrC. Acta Materialia 110 (2016) 192–199.

[47] J. Zhou, et al., A two-dimensional zirconium carbide by selective etching of Al_3C_3 from nanolaminated $Zr_3Al_3C_5$, Angew. Chem. Int. Ed. 55 (16) (2016) 5008–5013.

[48] A. Ul-Hamid, Microstructure, properties and applications of Zr-carbide, Zr-nitride and Zr-carbonitride coatings: a review, Mat. Adv. 1 (5) (2020) 1012–1037.

[49] J. Xiang, et al., Mechanochemically activated synthesis of zirconium carbide nanoparticles at room temperature: a simple route to prepare nanoparticles of transition metal carbides, J. Eur. Ceram. Soc. 31 (8) (2011) 1491–1496.

[50] M. Dollé, et al., Synthesis of nanosized zirconium carbide by a sol–gel route, J. Eur. Ceram. Soc. 27 (4) (2007) 2061–2067.

[51] J.-X. Wang, et al., Synthesis of nanocrystallized zirconium carbide based on an aqueous solution-derived precursor, RSC Adv. 7 (37) (2017) 22722–22727.

[52] B. Tunca, et al., Synthesis of MAX phases in the Zr-Ti-Al-C system, Inorg. Chem. 56 (6) (2017) 3489–3498.

[53] Q. Meng, et al., Theoretical investigation of zirconium carbide MXenes as prospective high capacity anode materials for Na-ion batteries, J. Mater. Chem. A 6 (28) (2018) 13652–13660.

[54] J. Zhu, et al., S-functionalized MXenes as electrode materials for Li-ion batteries, Appl. Mater. Today 5 (2016) 19–24.

[55] X. Shao, et al., Zr_2Si: an antiferromagnetic Dirac MXene, Phys. Chem. Chem. Phys. 20 (6) (2018) 3946–3952.

[56] H.T. Li, et al., Mechanical properties of 2D $Zr_{n+1}C_n$(n=1, 2) MXenes with and without functionalization, Journal of Physics-Condensed Matter 34 (46) (2022).

[57] C.Y. Wang, et al., A first-principles study on the vibrational and electronic properties of Zr-C MXenes, Commun. Theor. Phys. 69 (3) (2018) 336–342.

[58] Y.-H. Lin, G.-R. Lin, Kelly sideband variation and self four-wave-mixing in femtosecond fiber soliton laser mode-locked by multiple exfoliated graphite nano-particles, Laser Phys. Lett. 10 (4) (2013) 045109.

[59] C. Zhang, et al., A hydrazone organic optical modulator with a π electronic system for ultrafast photonics, J. Mater. Chem. C 9 (34) (2021) 11306–11313.

[60] A.L. Chamberlain, et al., High-strength zirconium diboride-based ceramics, J. Am. Ceram. Soc. 87 (6) (2004) 1170–1172.

[61] X.-H. Zha, et al., Role of the surface effect on the structural, electronic and mechanical properties of the carbide MXenes, EPL (Europhysics Letters) 111 (2) (2015) 26007.

[62] U. Yorulmaz, et al., Vibrational and mechanical properties of single layer MXene structures: a first-principles investigation, Nanotechnology 27 (33) (2016) 335702.

[63] L.-F. He, et al., Microstructure, mechanical, thermal, and oxidation properties of a $Zr_2[Al(Si)]_4C_5$–SiC composite prepared by in situ reaction/hot-pressing, J. Eur. Ceram. Soc. 30 (11) (2010) 2147–2154.

[64] T.H. Courtney, Mechanical Behavior of Materials, Waveland Press, 2005.

[65] T. Li, Ideal strength and phonon instability in single-layer MoS_2. Physical review B—condensed matter and materials, Physics 85 (23) (2012) 235407.

[66] Y. Yang, et al., Brittle Fracture of 2D $MoSe_2$. Advanced Materials (Deerfield Beach, Fla.) 29(2), 2016.

[67] H. Li, et al., Mechanical properties of 2D $Zr_{n+1}C_n$ (n = 1, 2) MXenes with and without functionalization, J. Phys. Condens. Matter 34 (46) (2022) 465502.

[68] L. He, et al., Synthesis, physical, and mechanical properties of bulk $Zr_3Al_3C_5$ ceramic, J. Am. Ceram. Soc. 90 (4) (2007) 1164–1170.

[69] Z. Guo, et al., Flexible two-dimensional $Ti_{n+1}C_n$ (n = 1, 2 and 3) and their functionalized MXenes predicted by density functional theories, Phys. Chem. Chem. Phys. 17 (23) (2015) 15348–15354.

[70] H. Li, et al., Mechanical properties of 2D $Zr_{n+1}C_n$ (n = 1, 2) MXenes with and without functionalization, J. Phys. Condens. Matter 34 (46) (2022) 465502.

[71] D. Clatterbuck, et al., Phonon instabilities and the ideal strength of aluminum, Phys. Rev. Lett. 91 (13) (2003) 135501.

[72] D.R. Hussein, K.K. Abbas, A.M.H.A. Al-Ghaban, Overview of structural, electronic, elastic, thermal, optical, and nuclear properties of Zr_2AC (a= Al, Si, P, S, Ge, as, se in, Sn, Tl, and Pb) MAX phases: a brief review, Heliyon 9 (8) (2023) e18303.

[73] T. Zhou, et al., Atomic vacancy defect, Frenkel defect and transition metals (Sc, V, Zr) doping in Ti_4N_3 MXene nanosheet: a first-principles investigation, Appl. Sci. 10 (7) (2020) 2450.

[74] J. Wang, et al., First-principles prediction of the mechanical properties and electronic structure of ternary aluminum carbide $Zr_3Al_3C_5$, Phys. Rev. B 73 (13) (2006) 134107.

[75] A. Champagne, J.-C. Charlier, Physical properties of 2D MXenes: from a theoretical perspective, Journal of Physics: Materials 3 (3) (2020) 032006.

[76] M. Khazaei, et al., Novel electronic and magnetic properties of two-dimensional transition metal carbides and nitrides, Adv. Funct. Mater. 23 (17) (2013) 2185–2192.

[77] Z.-H. Yang, et al., More realistic band gaps from meta-generalized gradient approximations: only in a generalized Kohn-sham scheme, Phys. Rev. B 93 (20) (2016) 205205.

[78] F. Bibi, et al., Double transition metal MXenes for enhanced electrochemical applications: challenges and opportunities, EcoMat 6 (9) (2024) e12485.

[79] Z. Bao, et al., Role of MXene surface terminations in electrochemical energy storage: a review, Chin. Chem. Lett. 32 (9) (2021) 2648–2658.

[80] J. Zhou, et al., Synthesis and electrochemical properties of two-dimensional hafnium carbide, ACS Nano 11 (4) (2017) 3841–3850.

[81] N. Li, Y. Li, J. Fan, Prediction of chemically ordered dual transition metal carbides (MXenes) as high-capacity anode materials for Na-ion batteries, Nanoscale 13 (15) (2021) 7234–7243.

[82] W. Cui, et al., Atomic defects, functional groups and properties in MXenes, Chin. Chem. Lett. 32 (1) (2021) 339–344.

[83] A.N. Gandi, H.N. Alshareef, U. Schwingenschlögl, Thermoelectric performance of the MXenes M_2CO_2 (M = Ti, Zr, or Hf), Chem. Mater. 28 (6) (2016) 1647–1652.

[84] G. Chen, et al., Microstructure and properties of hot pressed $Zr_2(Al(Si))_4C_5$/SiC composites, J. Alloys Compd. 481 (1) (2009) 877–880.

[85] Y.-C. Zhou, et al., Synthesis and structure–property relationships of a new family of layered carbides in Zr-Al(Si)-C and Hf-Al(Si)-C systems, J. Eur. Ceram. Soc. 33 (15) (2013) 2831–2865.

[86] Y. Yue, et al., Tuning the magnetic properties of Zr_2N MXene by biaxial strain, Ceram. Int. 47 (2) (2021) 2367–2373.

[87] J. Wang, et al., Strongly-coupled magnetic nanospheres@trimetallic LDH hooding with thin MXenes veil: sandwiched ternary nanostructure towards forging fire-safe EP with low toxicity, Appl. Surf. Sci. 612 (2023) 155904.

[88] S. Zhao, W. Kang, J. Xue, Manipulation of electronic and magnetic properties of M_2C (M = Hf, Nb, Sc, Ta, Ti, V, Zr) monolayer by applying mechanical strains, Appl. Phys. Lett. **104 (13) (2014).**

[89] L. Song, et al., Novel three-dimensional Ti_3C_2-MXene embedded zirconium alginate aerogel adsorbent for efficient phosphate removal in water, Chemosphere 319 (2023) 138016.

[90] J. Wang, et al., Nonlinear absorption response of zirconium carbide films, ACS Appl. Mater. Interfaces 15 (2) (2023) 3317–3324.

[91] Q. Liu, et al., Prodrug-loaded zirconium carbide Nanosheets as a novel biophotonic Nanoplatform for effective treatment of Cancer, Adv. Sci. 7 (24) (2020) 2001191.

[92] G. Dai, et al., Zirconium-Based Metal–Organic Framework and $Ti_3C_2T_x$ Nanosheet-Based Faraday Cage-Type Electrochemical Aptasensor for *Escherichia coli* Detection, ACS Applied Nano Materials 5 (7) (2022) 9201–9208.

[93] L. Liu, et al., Functionalizing MXene towards highly stretchable, ultratough, fatigue- and fire-resistant polymer nanocomposites, Chem. Eng. J. 424 (2021) 130338.

[94] N.R. Shailaja, et al., Corallocarpus epigaeus mediated synthesis of ZnO/CuO integrated ZrO_2 nanoparticles for enhanced in-vitro antibacterial, antifungal and antidiabetic activities, J. Indian Chem. Soc. 100 (5) (2023) 100991.

[95] X. Yan, W. Cao, H. Li, Thermoelectric properties of $X_3N_2O_2$ (X = Hf, Zr) MXene monolayers: a first-principles study, RSC Adv. 13 (27) (2023) 18323–18327.

[96] C.-Y. Wang, et al., A first-principles study on the vibrational and electronic properties of Zr-C MXenes*, Commun. Theor. Phys. 69 (3) (2018) 336.

[97] H. Zhang, et al., First-principle study of electronic, optical, quantum capacitance, carrier mobility and photocatalytic properties of Zr_2CO_2 MXene under uniaxial strain, Vacuum 220 (2024) 112813.

[98] H. Zhang, et al., Strain engineering of electronic properties, quantum capacitance, and photocatalytic properties of Zr_2CO_2 MXene, Mol. Catal. 547 (2023) 113330.

[99] X. Li, et al., $Zr_3C_2O_2$ MXene as promising candidate for NH_3 sensor with high sensitivity and selectivity at room temperature, Appl. Surf. Sci. 624 (2023) 157125.

[100] C. Shao, et al., Rational design single-atom modified Zr_2CO_2 MXene as a promising catalyst for nitrogen reduction reaction, Int. J. Hydrog. Energy 51 (2024) 1153–1160.

[101] M. Naguib, et al., Two-dimensional nanocrystals produced by exfoliation of Ti_3AlC_2, Adv. Mater. 23 (37) (2011) 4248–4253.

[102] J. Zhou, et al., A two-dimensional zirconium carbide by selective etching of Al_3C_3 from Nanolaminated $Zr_3Al_3C_5$, Angew. Chem. Int. Ed. 55 (16) (2016) 5008–5013.

[103] C. Morant, et al., An XPS study of the interaction of oxygen with zirconium, Surf. Sci. 218 (2) (1989) 331–345.

[104] M. Naguib, et al., Two-dimensional transition metal carbides, ACS Nano 6 (2) (2012) 1322–1331.

[105] M. Ghidiu, et al., Conductive two-dimensional titanium carbide 'clay' with high volumetric capacitance, Nature 516 (7529) (2014) 78–81.

[106] O. Mashtalir, et al., Intercalation and delamination of layered carbides and carbonitrides, Nat. Commun. 4 (1) (2013) 1716.

[107] W. Zhang, et al., An electrochemically switched ion exchange α-ZrP/PPy film as a synergistically catalytic and anchoring material towards lithium-sulfur battery design, Electrochim. Acta 403 (2022) 139609.

[108] H. Li, et al., Preparation of laminar α-ZrP nanosheets enhanced NiW nanocomposite coating and investigation of its mechanical and anti-corrosion properties, Surf. Coat. Technol. 423 (2021) 127590.

[109] H. Wang, et al., Quaternary ammonium salts intercalated α-ZrP compounds for adsorption of phenolic compounds, Appl. Surf. Sci. 268 (2013) 179–187.

[110] H. Ding, et al., Gelation based on host-guest interactions induced by multi-functionalized Nanosheets, Gels 7 (3) (2021).

[111] L. Ml, et al., Single-step exfoliation, acidification and covalent functionalization of α-zirconium phosphate for enhanced anticorrosion of waterborne epoxy coatings, Surf. and Interfaces 23 (2021) 100887.

[112] H. Xiao, S. Liu, Zirconium phosphate (ZrP)-based functional materials: synthesis, properties and applications, Mater. Des. 155 (2018) 19–35.

[113] Y. Zhao, et al., Synthesis of ultrathin α-zirconium phosphate functionalized with polypyrrole for reinforcing the anticorrosive property of waterborne epoxy coating, Colloids Surf. A Physicochem. Eng. Asp. 635 (2022) 128052.

[114] H. Huang, et al., Exfoliation and functionalization of α-zirconium phosphate in one pot for waterborne epoxy coatings with enhanced anticorrosion performance, Prog. Org. Coat. 138 (2020) 105390.

[115] R. Yang, et al., Recent research Progress in the structure, fabrication, and application of MXene-based Heterostructures, Nanomaterials (Basel) 12 (11) (2022).

[116] X. He, et al., One-pot fabrication of an MXene-ZrP@PDA heterojunction for enhanced corrosion/Wear resistance of waterborne epoxy coatings, Ind. Eng. Chem. Res. 61 (34) (2022) 12576–12589.

[117] I. Hussain, et al., Partially oxidized MXenes for energy storage applications, Prog. Mater. Sci. 147 (2025) 101351.

[118] A. Mostafaei, E. Faizabadi, E.H. Semiromi, Theoretical studies and tuning the electronic and optical properties of Zr_2CO_2 monolayer using biaxial strain effect: Modified Becke–Johnson calculation, Phys. E. 114 (2019) 113559.

[119] B. Peng, et al., Thermal conductivity of monolayer MoS_2, $MoSe_2$, and WS_2: interplay of mass effect, interatomic bonding and anharmonicity, RSC Adv. 6 (7) (2016) 5767–5773.

[120] Z. Liu, H.N. Alshareef, MXenes for optoelectronic devices, Adv. Electr. Mat. 7 (9) (2021) 2100295.

[121] R. Beiranvand, S. Valedbagi, Electronic and optical properties of advance semiconductor materials: BN, AlN and GaN nanosheets from first principles, Optik 127 (3) (2016) 1553–1560.

[122] U. Keller, Recent developments in compact ultrafast lasers, Nature 424 (6950) (2003) 831–838.

[123] Y. Liang, et al., Mid-infrared Q-switch performance of ZrC, Photonics Research 8 (12) (2020) 1857–1861.

[124] U. Yorulmaz, et al., A systematical ab-initio review of promising 2D MXene monolayers towards Li-ion battery applications, J. Physics: Energy 2 (3) (2020) 032006.

[125] K.A. Papadopoulou, A. Chroneos, S.-R.G. Christopoulos, Ion incorporation on the Zr_2CS_2 MXene monolayer towards better-performing rechargeable ion batteries, J. Alloys Compd. 922 (2022) 166240.

[126] J. Wu, et al., Towards a high-rate and long-life $LiVPO_4F$/C cathode material for lithium ion batteries by potassium and zirconium co-doping, J. Power Sources 401 (2018) 142–148.

[127] S. Zhao, W. Kang, J. Xue, Manipulation of electronic and magnetic properties of M_2C (M= Hf, Nb, Sc, Ta, Ti, V, Zr) monolayer by applying mechanical strains, Appl. Phys. Lett. 104 (13) (2014).

[128] S. Khan, et al., Functionalized Hf_3C_2 and Zr_3C_2 MXenes for suppression of shuttle effect to enhance the performance of sodium–sulfur batteries, J. Power Sources 580 (2023) 233298.

[129] X.-H. Zha, et al., Surface potential-determined performance of $Ti_3C_2T_2$ (T = O, F, OH) and $Zr_3C_2T_2$ (T = O, F, OH, S) MXenes as anode materials of sodium ion batteries, Nanoscale 14 (29) (2022) 10549–10558.

[130] P. Ma, et al., MXene-based materials for electrochemical sodium-ion storage, Adv. Sci. 8 (11) (2021) 2003185.

[131] M. Wang, et al., Improved sodium storage properties of Zr-doped $Na_3V_2(PO_4)_2F_3$/C as cathode material for sodium ion batteries, Ceram. Int. 46 (18, Part A) (2020) 28490–28498.

[132] W. Liu, et al., Y-doped $Na_3V_2(PO_4)_2F_3$ compounds for sodium ion battery cathodes: electrochemical performance and analysis of kinetic properties, J. Mater. Chem. A 5 (22) (2017) 10928–10935.

[133] L. Li, et al., Fluorophosphates from solid-state synthesis and electrochemical ion exchange: $NaVPO_4F$ or $Na_3V_2(PO_4)_2F_3$? Adv. Energy Mater. 8 (24) (2018) 1801064.

[134] L.L. Zhang, et al., Polydopamine-derived nitrogen-doped carbon-covered $Na_3V_2(PO_4)_2F_3$ cathode material for high-performance Na-ion batteries, ACS Appl. Mater. Interfaces 10 (43) (2018) 36851–36859.

[135] W. Song, et al., Mechanistic investigation of ion migration in $Na_3V_2(PO_4)_2F_3$ hybrid-ion batteries, Phys. Chem. Chem. Phys. 17 (1) (2015) 159–165.

[136] W. Song, S. Liu, A sodium vanadium three-fluorophosphate cathode for rechargeable batteries synthesized by carbothermal reduction, Solid State Sci. 15 (2013) 1–6.

[137] M.-Q. Zhao, et al., Magnesium-ion storage capability of MXenes, ACS Applied Energy Materials 2 (2) (2019) 1572–1578.

[138] X. Wang, et al., Screening for stable ternary-metal MXenes as promising anode materials for sodium/potassium-ion batteries, J. Phys. Chem. C 125 (48) (2021) 26332–26338.

[139] N. Li, et al., Theoretical Investigation of the Structure–Property Correlation of MXenes as Anode Materials for Alkali Metal Ion Batteries, J. Phys. Chem. C 124 (28) (2020) 14978–14986.

[140] K.G. Motora, et al., Waste-to-energy: development of a highly efficient keratin enhanced chitosan bio-waste-derived triboelectric Nanogenerator for energy harvesting and real applications, Adv. Funct. Mater. 34 (22) (2024) 2315069.
[141] M.R. Gokana, et al., Effects of patterned electrode on near infrared light-triggered cesium tungsten bronze/poly(vinylidene)fluoride nanocomposite-based pyroelectric nanogenerator for energy harvesting, J. Power Sources 536 (2022) 231524.
[142] K.G. Motora, et al., Effect of electrode patterns on piezoelectric energy harvesting property of zinc oxide polyvinylidene fluoride based piezoelectric nanogenerator, Renew. Energy 217 (2023) 119208.
[143] J. Lee, et al., Conductive Fiber-based ultrasensitive textile pressure sensor for wearable electronics, Adv. Mater. 27 (15) (2015) 2433–2439.
[144] S. Cui, et al., Self-powered ammonia nanosensor based on the integration of the gas sensor and triboelectric nanogenerator, Nano Energy 49 (2018) 31–39.
[145] I. Park, et al., A 4.5-to-16μW integrated triboelectric energy-harvesting system based on high-voltage dual-input buck converter with MPPT and 70V maximum input voltage. in 2018 IEEE International Solid-State Circuits Conference - (ISSCC), 2018.
[146] A.N. Simões, et al., A triboelectric Nanogenerator for energy harvesting from Transformers' vibrations, Machines 10 (3) (2022) 215.
[147] S.M.S. Rana, et al., Zirconium metal-organic framework and hybridized co-NPC@MXene nanocomposite-coated fabric for stretchable, humidity-resistant triboelectric nanogenerators and self-powered tactile sensors, Nano Energy 104 (2022) 107931.
[148] H. Wang, et al., Improvement in surface performance of stainless steel by nitride and carbon-based coatings prepared via physical vapor deposition for marine application, J. Mater. Res. Technol. 27 (2023) 6021–6046.
[149] I. Khan, K. Saeed, I. Khan, Nanoparticles: properties, applications and toxicities, Arab. J. Chem. 12 (7) (2019) 908–931.
[150] M. Behzadnasab, et al., Corrosion performance of epoxy coatings containing silane treated ZrO_2 nanoparticles on mild steel in 3.5% NaCl solution, Corros. Sci. 53 (1) (2011) 89–98.
[151] Y. Zhang, et al., Graphene-like two-dimensional nanosheets-based anticorrosive coatings: a review, J. Mater. Sci. Technol. 129 (2022) 139–162.
[152] M. AhadiParsa, et al., Rising of MXenes: novel 2D-functionalized nanomaterials as a new milestone in corrosion science-a critical review, Adv. Colloid Interf. Sci. 307 (2022) 102730.
[153] Z.L. Wang, J. Song, Piezoelectric nanogenerators based on zinc oxide nanowire arrays, Science 312 (5771) (2006) 242–246.
[154] K. Huang, et al., Two-dimensional transition metal carbides and nitrides (MXenes) for biomedical applications, Chem. Soc. Rev. 47 (14) (2018) 5109–5124.
[155] R. Baskar, et al., Cancer and radiation therapy: current advances and future directions, Int. J. Med. Sci. 9 (3) (2012) 193–199.
[156] Y. Bai, et al., Zr-based metal–organic frameworks: design, synthesis, structure, and applications, Chem. Soc. Rev. 45 (8) (2016) 2327–2367.
[157] H.S. Han, K.Y. Choi, Advances in nanomaterial-mediated Photothermal Cancer therapies: toward clinical applications, Biomedicines 9 (3) (2021).
[158] Q. Liu, et al., Prodrug-loaded zirconium carbide nanosheets as a novel biophotonic nanoplatform for effective treatment of cancer, Adv. Sci. 7 (24) (2020) 2001191.
[159] L.M. Dong, et al., Two-dimensional metal carbides and nitrides (MXenes): preparation, property, and applications in cancer therapy, Nanophotonics 9 (8) (2020) 2125–2145.
[160] G.S. Karagiannis, et al., Neoadjuvant chemotherapy induces breast cancer metastasis through a TMEM-mediated mechanism, Sci. Transl. Med. 9 (397) (2017) eaan0026.
[161] A.M. Bannunah, Biomedical applications of zirconia-based nanomaterials: challenges and future perspectives, Molecules 28 (14) (2023) 5428.
[162] A. Jama-Rodzeńska, et al., Waste to phosphorus: a transdisciplinary solution to P recovery from wastewater based on the TRIZ approach, J. Environ. Manag. 287 (2021) 112235.
[163] M.-P. Soro, et al., Nitrogen and phosphorus spatio-temporal distribution and fluxes intensifying eutrophication in three tropical rivers of Côte d'Ivoire (West Africa), Mar. Pollut. Bull. 186 (2023) 114391.
[164] R. Bashar, et al., Cost effectiveness of phosphorus removal processes in municipal wastewater treatment, Chemosphere 197 (2018) 280–290.
[165] H. Zhang, et al., Computational studies on the structural, electronic and optical properties of graphene-like MXenes (M_2CT_2, M= Ti, Zr, Hf; T= O, F, OH) and their potential applications as visible-light driven photocatalysts, J. Mater. Chem. A 4 (33) (2016) 12913–12920.
[166] S. Iravani, et al., Advancements in MXenes and mechanochemistry: exploring new horizons and future applications, Mat. Adv. 5 (21) (2024) 8404–8418.
[167] J. Wu, Y. Yu, G. Su, Safety assessment of 2D MXenes, In Vitro and In Vivo. 12 (5) (2022) 828.
[168] I.A. Vasyukova, et al., Synthesis, toxicity assessment, environmental and biomedical applications of MXenes: a, Review 12 (11) (2022) 1797.